

# **Quantum entanglement in polarization and space**

## **PROEFSCHRIFT**

ter verkrijging van  
de graad van Doctor aan de Universiteit Leiden,  
op gezag van de Rector Magnificus Dr. D. D. Breimer,  
hoogleraar in de faculteit der Wiskunde en  
Natuurwetenschappen en die der Geneeskunde,  
volgens besluit van het College voor Promoties  
te verdedigen op 5 oktober 2006,  
klokke 16.15 uur

door

**Peter Sing Kin Lee**

geboren te Wageningen, Nederland  
op 12 december 1978

**Promotiecommissie:**

Promotor: Prof. dr. J. P. Woerdman  
Copromotor: Dr. M. P. van Exter  
Referent: Dr. R. J. C. Spreeuw (Universiteit van Amsterdam)  
Leden: Dr. M. J. A. de Dood  
Prof. dr. G. Nienhuis  
Dr. C. H. van der Wal (Rijksuniversiteit Groningen)  
Prof. dr. A. Lagendijk (AMOLF/Universiteit Twente)  
Prof. dr. K. A. H. van Leeuwen (Technische Universiteit Eindhoven)  
Prof. dr. P. H. Kes

The work reported in this thesis is part of a research programme of 'Stichting voor Fundamenteel Onderzoek der Materie' (FOM) and was supported by the EU programme IST-ATESIT.

---

## Contents

---

<b>1</b>	<b>Introduction</b>	<b>1</b>
1.1	Quantum entanglement . . . . .	1
1.2	Quantum-entangled photons . . . . .	2
1.3	Thesis . . . . .	3
<b>2</b>	<b>Spontaneous parametric down-conversion and quantum entanglement of photons</b>	<b>5</b>
2.1	Introduction . . . . .	6
2.2	Spontaneous parametric down-conversion . . . . .	6
2.2.1	The biphoton wavefunction . . . . .	6
2.2.2	Phase matching in type-II SPDC . . . . .	7
2.3	Polarization entanglement . . . . .	10
2.3.1	The polarization-entangled state . . . . .	10
2.3.2	Limitations to the degree of polarization entanglement . . . . .	10
2.3.3	Experimental scheme for measurement of polarization entanglement . . . . .	11
2.4	Spatial entanglement . . . . .	12
2.4.1	The spatially entangled state . . . . .	12
2.4.2	State representation in a modal basis . . . . .	13
2.5	Concluding remarks . . . . .	14
<b>3</b>	<b>Simple method for accurate characterization of birefringent crystals</b>	<b>15</b>
3.1	Introduction . . . . .	16
3.2	Theory . . . . .	16
3.3	Experimental setup . . . . .	18
3.4	Measurements and results . . . . .	19
3.5	Discussion . . . . .	21
3.6	Conclusions . . . . .	23

<b>4</b>	<b>Increased polarization-entangled photon flux via thinner crystals</b>	<b>25</b>
4.1	Introduction . . . . .	26
4.2	Measurements and results . . . . .	27
4.3	Concluding discussion . . . . .	31
4.4	Acknowledgements . . . . .	32
<b>5</b>	<b>Time-resolved polarization decoherence in metal hole arrays with correlated photons</b>	<b>33</b>
5.1	Introduction . . . . .	34
5.2	Experimental methods . . . . .	35
5.3	Experimental results . . . . .	37
5.4	Concluding discussions . . . . .	41
5.5	Acknowledgments . . . . .	41
<b>6</b>	<b>How focused pumping affects type-II spontaneous parametric down-conversion</b>	<b>43</b>
6.1	Introduction . . . . .	44
6.2	Theory . . . . .	44
6.3	Measurements and results . . . . .	47
6.4	Concluding discussion . . . . .	52
6.5	Acknowledgments . . . . .	52
<b>7</b>	<b>Polarization entanglement behind single-mode fibers: spatial selection and spectral labeling</b>	<b>53</b>
7.1	Introduction . . . . .	54
7.2	Theory . . . . .	54
7.3	Experimental results . . . . .	55
7.3.1	Experimental setup . . . . .	55
7.3.2	Mode matching . . . . .	56
7.3.3	Free-space detection versus fiber-coupled detection . . . . .	58
7.3.4	Spectral labeling . . . . .	59
7.4	Conclusion . . . . .	62
<b>8</b>	<b>Spatial labeling in a two-photon interferometer</b>	<b>63</b>
8.1	Introduction . . . . .	64
8.2	Theoretical description . . . . .	65
8.2.1	The generated two-photon field . . . . .	65
8.2.2	Two-photon interference . . . . .	67
8.2.3	Why the number of mirrors matters . . . . .	68
8.2.4	Temporal labeling . . . . .	70
8.2.5	Spatial labeling . . . . .	72
8.3	Experimental results . . . . .	73
8.3.1	Experimental setup . . . . .	73
8.3.2	Temporal labeling . . . . .	74
8.3.3	Spatial labeling . . . . .	78
8.3.4	Modal analysis of spatial entanglement . . . . .	82

8.4	Concluding discussion . . . . .	83
8.5	Acknowledgments . . . . .	84
8.A	A frequency non-degenerate two-photon interferometer . . . . .	85
<b>9</b>	<b>Mode counting in high-dimensional orbital angular momentum entanglement</b>	<b>89</b>
	<b>Bibliography</b>	<b>97</b>
	<b>Summary</b>	<b>107</b>
	<b>Samenvatting</b>	<b>115</b>
	<b>List of publications</b>	<b>123</b>
	<b>Curriculum vitæ</b>	<b>125</b>
	<b>Nawoord</b>	<b>127</b>



### 1.1 Quantum entanglement

Since quantum mechanics was born in the early 20th century, its controversial character has intrigued many physicists in their perception of nature. Undoubtedly, quantum mechanics offers a precise and elegant description of physical phenomena in various disciplines, ranging from subatomic physics to molecular physics and condensed-matter physics. In the shadow of this success, however, counterintuitive concepts of quantum mechanics have always been looming and have triggered several discussions on the foundations of quantum mechanics.

One of these concepts is quantum entanglement which originates from the well-known Gedankenexperiment proposed by Albert Einstein, Boris Podolsky and Nathan Rosen (EPR) in 1935 [1]. In this experiment, two physical systems are considered to interact with respect to a certain observable. Due to the interaction the two systems will exhibit a strong mutual relation with respect to this observable. This so-called quantum entanglement means that the *individual* outcomes of the observables cannot be predicted with certainty for each of the two EPR systems, but the outcomes of the observables for the two systems are always strictly correlated. Quantum entanglement offends physical reality in the sense that the individual measurement results are fundamentally undetermined before the measurement. According to quantum mechanics, a measurement of a certain value of the observable in one EPR system instantaneously determines the state of the other system, irrespective of the distance between the systems. This latter condition implies that quantum entanglement also contradicts the concept of locality. The EPR paper thus concluded that quantum mechanics is apparently incompatible with a local and realistic description of nature, and therefore cannot be considered as a “complete theory”.

It was not until 1964 that John Bell translated the somewhat philosophical EPR discussion into a concrete test of the conflict between local realism and quantum mechanics [2]. This

test consists of a set of inequalities which must be satisfied by any local and realistic theory. Quantum mechanics, however, predicts violation of these so-called Bell's inequalities for measurements on specific quantum-entangled systems. Some years later, Clauser, Horne, Shimony and Holt (CHSH) introduced a generalized version of Bell's inequalities which applies to real laboratory experiments with, for example, quantum-entangled photons [3]. By now, many of such experiments on EPR particles have shown strong violation of Bell's inequalities and thus confirmed the non-local nature of entanglement [4–13]. Especially in the last 15 years, investigations on the fundamental concept of quantum entanglement have also led to perspective applications in information science, such as quantum cryptography [14, 15], quantum teleportation [16, 17] and quantum computation [18].

## 1.2 Quantum-entangled photons

The first experimental proof of quantum entanglement via violation of Bell's inequalities was reported by Clauser and Shimony in 1978 [4]. A few years later, Aspect and co-workers [5] performed similar experiments in a more efficient way which yielded even more convincing results. For this pioneering work, photon pairs were used as the EPR particle systems. Ever since this major breakthrough, these photon pairs have remained the most popular tool for testing quantum correlations.

Despite the success of these early-generation EPR experiments [19], the employed atomic cascade source of photon pairs has only incidentally been employed in follow-up experiments [9] because of the poor pair-production rate and collection efficiency. Instead, the production of quantum-entangled photons via the non-linear process of spontaneous parametric down-conversion (SPDC) in a birefringent crystal [20] became more favourable. In fact, the first SPDC source of photon pairs was already presented by Burnham and Weinberg in 1970 [21]. They successfully observed photon coincidences by matching the detection to the energy- and momentum-conservation conditions of the SPDC process. The new generation of EPR experiments [19], where a SPDC source is used to test the quantum correlations between photons, was simultaneously introduced by two groups in the late 80's [6, 7], and quickly adopted by others [10, 11]. The popularity of EPR photon pairs is also reflected by the ongoing development of high-quality and high-intensity SPDC sources [8, 22–24].

As mentioned before, the entanglement of two-particle systems is always with respect to a certain observable. For quantum-entangled photons three of such observables can be distinguished, being polarization, energy or time (longitudinal space), and transverse momentum or transverse space. The corresponding types of entanglement are called polarization, time and spatial entanglement of photons, respectively. The entanglement of photons is in principle simultaneous in the three mentioned observables. In this respect, one can also speak about multiparameter or hyperentanglement [25, 26].

In the first entanglement experiments [4, 5] only polarization correlations of EPR photons were measured. Since then, EPR experiments with polarization-entangled photons have always been most popular due to their practical simplicity [6–8, 23, 24]. Time entanglement of photons has been widely investigated in several interferometric schemes [9–11, 27–29]. Somewhat less explored are the spatial correlations of entangled photons. The most notable experiments on spatial entanglement study these correlations by conditional imaging of the

transverse positions of the pair-photons [30, 31].

## 1.3 Thesis

The contents of this thesis covers research that has been performed to gain deeper insight into both polarization entanglement and spatial entanglement of photons. The general theme of this work is to investigate the quality of entanglement under different experimental settings. The explored conditions are associated with the manipulation of both the production and detection of entangled photons. Apart from the entanglement quality, the general interest was also focused on the yield of photon pairs under these conditions. As a kind of sidetrip, particular attention is paid to the degradation of polarization correlations caused by time- and space-related decoherence processes in a metal hole array (Chapter 5). Below, the structure of the thesis is presented in some more detail.

- Chapter 2 provides a brief description of the non-linear process of spontaneous parametric down-conversion (SPDC) as a source of quantum-entangled photons. Starting from the two-photon entangled state, polarization entanglement and spatial entanglement of photons are introduced in an analogous way.
- Chapter 3 presents a novel method for simultaneous determination of the thickness and cutting angle of a birefringent non-linear crystal that can e.g. be used as a SPDC source. Although this simple method is based only on polarization interferometry, it allows a highly accurate measurement of both the crystal thickness and cutting angle.
- Chapter 4 demonstrates how the thickness of the SPDC source determines its brightness, i.e., the generated number of polarization-entangled photons pairs. This result follows from simple scaling laws and is supported by experimental data.
- Chapter 5 addresses the question whether time- and space-related polarization- decoherence channels commute. These channels are created by sending entangled photons in succession through a birefringent delay and focusing them on a metal hole array, thereby using the thin crystal discussed in Chapter 4 to create sufficient time resolution. The experimental results are interpreted in terms of the propagation of surface plasmons that are excited on the hole array.
- Chapter 6 shows the consequences of focused pumping on the spatial distribution of the generated SPDC light and the obtained quality of polarization entanglement.
- Chapter 7 focuses on the polarization-entanglement attained behind single-mode optical fibers. The concept of transverse mode matching, which is needed for optimal photon-pair collection, is revised by explicit count rate measurements. The limitations to the entanglement quality are investigated for detection behind both apertures and fibers.
- Chapter 8 specifically treats the *spatial* entanglement of photons that are generated via SPDC. The theoretical and experimental work in this chapter study the spatial coherence of the two-photon wavepacket under different geometries of the employed two-photon interferometer.

## 1. Introduction

- Chapter 9 demonstrates how the same interferometer, but now with an additional image rotator in one the two interferometer arms, allows for determination of the number of entangled orbital-angular-momentum (OAM) modes. This mode number follows from the OAM entanglement measured as a function of the spatial-profile rotation of the entangled light.

## CHAPTER 2

---

### Spontaneous parametric down-conversion and quantum entanglement of photons

---

*We briefly describe how spontaneous parametric down-conversion can be used to generate quantum-entangled photons and which limitations this imposes. The specific cases of polarization entanglement and spatial entanglement are discussed.*

## 2.1 Introduction

Mathematically speaking, two particles 1 and 2 are said to be entangled if their joint quantum state cannot be factorized into the quantum states of the individual particles. The physical interpretation of entanglement is that measurement of a quantum observable on particle 1 instantaneously determines the outcome of this observable for particle 2 and vice versa, irrespective of the interparticle distance and without any manipulation of particle 2. Two photons can be entangled in their polarization, transverse momentum or frequency, which implies that their two-photon wavefunction is non-factorizable in either of these degrees of freedom.

The standard source for production of quantum-entangled photon pairs is the non-linear process of spontaneous parametric down-conversion (SPDC) in a birefringent crystal [5, 8]. In this process, a single pump photon is split into two photons (often called signal and idler photon) such that the energies and transverse momenta of the down-converted photons add up to those of the pump photon. The basic scheme for generating and detecting entangled photon-pairs is schematically shown in Fig. 2.1. The pump light is directed onto the non-linear crystal to create entangled pair-photons that are emitted along path 1 and 2 and travel to detectors placed in each path. The entanglement is measured via some (quantum) correlations in the number of photon pairs that are counted as coincidence clicks between the two detectors.

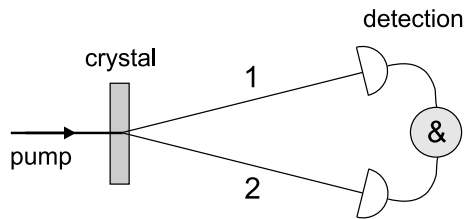


Figure 2.1: Basic scheme for generation and detection of entangled photon pairs.

In this chapter we will first give a description of SPDC as a source of entangled-photon pairs. Section 2.2 contains a general representation of the biphoton entangled state together with the phase-matching physics that governs the distribution of the emitted SPDC light. In Sec. 2.3 we will specifically focus on the polarization-entangled state and relate its spatial and frequency dependence to the degree of polarization entanglement. We also present, in some more detail, a general setup for measuring polarization entanglement with photons. In an analogous way, we will introduce the spatial entanglement of photons in Sec. 2.4. We will end with some concluding remarks in Sec. 2.5.

## 2.2 Spontaneous parametric down-conversion

### 2.2.1 The biphoton wavefunction

In general, the two-photon state produced via spontaneous parametric down-conversion in a nonlinear crystal can be represented by the wavefunction [32, 33]

$$|\Psi\rangle = \int d\mathbf{q}_1 \int d\mathbf{q}_2 \int d\omega_1 \int d\omega_2 \sum_{i=H,V} \sum_{j=H,V} \Phi_{ij}(\mathbf{q}_1, \omega_1; \mathbf{q}_2, \omega_2) \hat{a}_i^\dagger(\mathbf{q}_1, \omega_1) \hat{a}_j^\dagger(\mathbf{q}_2, \omega_2) |0\rangle. \quad (2.1)$$

The creation operators  $\hat{a}_i^\dagger(\mathbf{q}_1, \omega_1)$  and  $\hat{a}_j^\dagger(\mathbf{q}_2, \omega_2)$  act on the vacuum state  $|0\rangle$ , and create a photon in beam 1 with transverse momentum  $\mathbf{q}_1$ , frequency  $\omega_1$  and polarization  $i$ , and a photon in beam 2 with transverse momentum  $\mathbf{q}_2$ , frequency  $\omega_2$  and polarization  $j$ , respectively. The polarizations of photon 1 and 2 are labelled by indices  $i$  and  $j$  where the summation is over the horizontal ( $H$ ) and vertical ( $V$ ) polarization. Conservation of energy and transverse momentum in the down-conversion process requires  $\omega_p = \omega_1 + \omega_2$  and  $\mathbf{q}_p = \mathbf{q}_1 + \mathbf{q}_2$ .

The physics of the SPDC process and the quantum entanglement are contained in the biphoton amplitude functions  $\Phi_{ij}(\mathbf{q}_1, \omega_1; \mathbf{q}_2, \omega_2)$ . In fact, these amplitude functions depend on three different aspects that embody (i) the transverse profile of the pump field  $E_p(\mathbf{q}_p, \omega_p)$ , (ii) the phase mismatch built up during propagation inside the generating crystal and (iii) the two-photon propagation from the crystal plane to the detection plane. For a convenient description of a certain type of entanglement, one does not incorporate all three contributions but often neglects one of them. For instance, in the study of spatial entanglement one often assumes the crystal to be ‘‘sufficiently thin’’ so that the phase mismatch can be neglected [34]. This so-called thin-crystal limit is only a relative concept: the crystal is only thin enough *in relation* to the spectral detection bandwidth and spatial opening angle of the detected SPDC light.

Equation (2.1) provides a full description of the two-photon state that is in principle simultaneously entangled in polarization, frequency (time entanglement) and transverse momentum (spatial entanglement), i.e., non-separable in all three corresponding variables. The quantum entanglement is contained in the threefold labeling of the biphoton amplitude function  $\Phi$ . To describe one of the three types of entanglement, one isolates the relevant variable by integrating over the other two. In the Secs. 2.3 and 2.4 we will discuss in which way the symmetry properties of  $\Phi$  contains the polarization and spatial entanglement information.

### 2.2.2 Phase matching in type-II SPDC

The generation of SPDC light is among others determined by the phase-matching function which is incorporated in the biphoton amplitude  $\Phi$  and describes the phase mismatch  $\phi(\mathbf{q}_1, \omega_1; \mathbf{q}_2, \omega_2)$  built up in the crystal. Phase matching exists in two different forms which are known as type-I and type-II phase matching. In type-I phase matching, the down-converted photons have the same polarizations, i.e.  $i = j = H$  for a  $V$ -polarized pump photon. Twin photons generated under type-II phase matching have orthogonal polarizations ( $i = H$  and  $j = V$ , or vice versa).

In this section we restrict our description to type-II phase matching, where the crystalline  $c$ -axis lies in the  $yz$ -plane and where the horizontal and vertical polarization are defined along the  $x$ - and  $y$ -axis of the crystal frame, respectively (see Fig. 2.2). We consider the pump polarization to be vertical ( $e \rightarrow o + e$ ) and relabel the  $H$ - and  $V$ -polarization as the ordinary ( $o$ ) and extra-ordinary ( $e$ ) polarization. The average phase mismatch, being the mismatch for propagation over half the crystal length  $L/2$ , is then given by  $\phi = \Delta k_z L/2$  where  $\Delta k_z =$

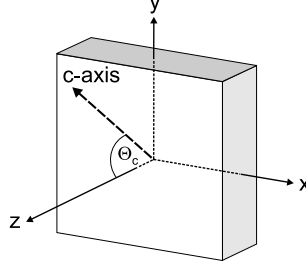


**Figure 2.2:** The crystal frame.

$k_{p,z} - k_{o,z} - k_{e,z}$  is the wave-vector mismatch in the  $z$ -direction parallel to the surface normal. If detection occurs far enough from the crystal, we can replace the transverse momenta  $\mathbf{q}$  by external angles  $\boldsymbol{\theta} = (\theta_x, \theta_y)$  via  $\boldsymbol{\theta} \approx (c/\omega)\mathbf{q}$ . The projected wavevectors can then be written as

$$k_{i,z} \approx n_i \left( \omega_i, \frac{\theta_{i,y}}{n_i} \right) \frac{\omega_i}{c} \cos \left( \frac{\theta_{i,x}}{n_i} \right) \cos \left( \frac{\theta_{i,y}}{n_i} \right), \quad (2.2)$$

where the index  $i = p, o$  or  $e$  and  $n_i$  are the corresponding refractive indices. Considering the paraxial approximation ( $|\theta_i| \ll 1$ ), we can Taylor-expand Eq. (2.2) around the angles  $\boldsymbol{\theta}_i = \mathbf{0}$  to obtain the phase mismatch [35]

$$\phi(\boldsymbol{\theta}_p, \boldsymbol{\theta}_o, \boldsymbol{\theta}_e) \approx \frac{L\Omega}{2c} \left\{ -C + (n_o - n_e(\Theta_c)) \frac{\delta\omega}{\Omega} + \rho(2\theta_{p,y} - \theta_{e,y}) + \frac{1}{2n} (\theta_{o,x}^2 + \theta_{o,y}^2 + \theta_{e,x}^2 + \theta_{e,y}^2) \right\}. \quad (2.3)$$

We have used  $\delta\omega = \Omega - \omega_o = \omega_e - \Omega \ll \Omega$ , where  $\Omega = \omega_p/2$  is the SPDC degeneracy frequency. The constant  $C$  depends on material properties, the crystal tilt and the cutting angle  $\Theta_c$ , being the angle of the crystal axis with respect to the surface normal. In the last “quadratic” angular terms we have neglected the (relatively small) difference between the group refractive indices  $n_o$  and  $n_e(\Theta_c)$  and replaced them by the average index  $n$ . Furthermore, the internal walk-off angle is given by  $\rho = \partial \ln[n_e(\Theta_c)] / \partial \Theta_c$  [35]. It can also be rewritten in terms of the external walk-off angle  $\theta_{\text{off}}$  (see below) as  $\rho = (2/n)\theta_{\text{off}}$ .

A closer inspection of Eq. (2.3) reveals the emission profiles of the SPDC light which are defined by the condition  $\phi \approx 0$ . For plane-wave pumping ( $\boldsymbol{\theta}_p = \mathbf{0}$ ) and frequency degeneracy ( $\delta\omega = 0$ ), the ordinary and extra-ordinary light are emitted along two identical cones that are mirror-flipped images of each other and are spaced with respect to the pump over  $-\theta_{\text{off}}$  and  $\theta_{\text{off}}$ , respectively. The opening angles of the light cones are determined by the constant  $C$  and can be tuned by tilting the crystal. Figure 2.3 shows typical SPDC patterns that we observed with an intensified CCD camera for different tilting angles of the crystal. The righthand picture depicts the standard experimental geometry where the perpendicularly intersecting cones define the light paths 1 and 2 shown in Fig. 2.1. It is easy to verify that both intersections are then also spaced by the external angle  $\theta_{\text{off}}$  with respect to the pump. In Chapter 6 we

will show that the condition of focused pumping ( $\theta_{p,y} \neq 0$ ) can drastically affect the emitted SPDC pattern.

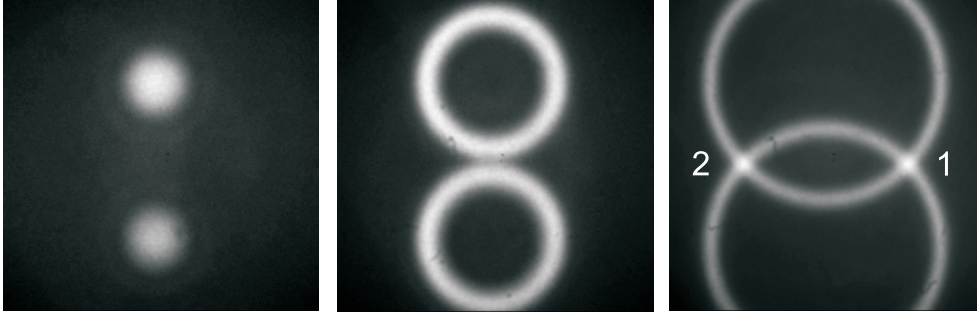


**Figure 2.3:** Intensified CCD images of SPDC emission for different tilting angles of the crystal. The orthogonal crossings 1 and 2 in the righthand picture define the regions for experimental study of polarization entanglement.

Figure 2.3 already provides a nice illustration of polarization entanglement. The ordinary and extra-ordinary ring have a well-defined horizontal and vertical polarization, respectively, except at the intersections 1 and 2. At these crossings, the individual polarizations of the pair-photons 1 and 2 are undetermined but always perpendicular to each other (for the singlet Bell state). The fact that one *in principle* cannot distinguish which polarization will emerge in which crossing makes these pair-photons polarization-entangled.

As we consider SPDC emission close to frequency degeneracy and as the SPDC crossings are the only relevant regions to study the entanglement, we can linearize the phase mismatch of Eq. (2.3) around these points ( $\theta_x = \pm\theta_{\text{off}} + \delta\theta_x$ ) to

$$\Delta\phi = \Delta k_z L/2 \approx \pi \left( \frac{\delta\omega}{\Delta\omega_{\text{SPDC}}} + \frac{\pm\delta\theta_x - \theta_y}{\Delta\theta_{\text{SPDC}}} \right), \quad (2.4)$$

where the plus and minus sign refer to the linearizations around  $\theta_x = +\theta_{\text{off}}$  and  $\theta_x = -\theta_{\text{off}}$ , respectively. The advantage of Eq. (2.4) is that it characterizes the phase mismatch as a function of the local frequency detuning  $\delta\omega$  and angular displacement  $\delta\theta_x$  relative to the degenerate coordinates  $(\Omega, \pm\theta_{\text{off}})$ . In Eq. (2.4) these local deviations are normalized to the SPDC spectral width  $\Delta\omega_{\text{SPDC}}$  and angular width  $\Delta\theta_{\text{SPDC}}$ , respectively, where

$$\Delta\omega_{\text{SPDC}} = \frac{2\pi c}{[n_o - n_e(\Theta_c)]L} \quad (2.5)$$

$$\Delta\theta_{\text{SPDC}} = \frac{\lambda}{\rho L}, \quad (2.6)$$

and  $\lambda = 2\pi c/\Omega$  is the degeneracy wavelength. Equation (2.6) gives the angular width in either the  $x$  or  $y$  direction. The real angular width in the radial directions is a factor  $\sqrt{2}$  smaller. Above equations obviously show that both the SPDC spectral and spatial width becomes larger for thinner crystals (see also Chapter 4).

## 2.3 Polarization entanglement

### 2.3.1 The polarization-entangled state

For the study of polarization entanglement, we consider two-photon production via type-II SPDC where the generated pair-photons have orthogonal polarizations, i.e., either  $i, j = H, V$  or  $i, j = V, H$ . The two-photon state in Eq. (2.1) can now be written as

$$|\Psi\rangle = \int d\mathbf{q}_1 \int d\mathbf{q}_2 \int d\omega_1 \int d\omega_2 \{ \Phi_{HV}(\mathbf{q}_1, \omega_1; \mathbf{q}_2, \omega_2) |H, \mathbf{q}_1, \omega_1; V, \mathbf{q}_2, \omega_2\rangle + \Phi_{VH}(\mathbf{q}_1, \omega_1; \mathbf{q}_2, \omega_2) |V, \mathbf{q}_1, \omega_1; H, \mathbf{q}_2, \omega_2\rangle \}. \quad (2.7)$$

Physically speaking, the pair-photons are polarization entangled if one *in principle* cannot distinguish which photon ( $H$  or  $V$ ) has travelled which path (1 or 2) on the basis of the measurement of any other variable than polarization. This is the case when the biphoton amplitude functions  $\Phi_{HV}$  and  $\Phi_{VH}$  overlap sufficiently well to prevent us to distinguish between the two states  $|HV\rangle$  and  $|VH\rangle$  on the basis of either frequency or spatial contents. The interference between these two probability channels is quantified by the wavefunction-overlap  $\langle\Psi|\Psi\rangle$  which is proportional to the coincidence count rate for simultaneous detection of one pair-photon in each detector (see Sec. 2.3.3). As the polarization entanglement is hidden in the interference terms ( $\propto \Phi_{HV}^* \Phi_{VH}$ ), an experimental measure for the degree of entanglement is given by [37]

$$V_{\text{pol}} = \frac{\langle\langle 2\text{Re}(\Phi_{HV}^* \Phi_{VH}) \rangle\rangle}{\langle\langle |\Phi_{HV}|^2 + |\Phi_{VH}|^2 \rangle\rangle}. \quad (2.8)$$

The double brackets  $\langle\langle \dots \rangle\rangle$  are just a shorthand notation of the six-fold integration over the range of momentum and frequency variables determined by the two apertures and the transmission of the two bandwidth filters, respectively. Maximal entanglement ( $V_{\text{pol}} = 1$ ) is obtained when  $\Phi_{HV} = \Phi_{VH}$ , i.e., when the amplitude functions are symmetric under exchange of labels. As soon as these functions differ due to a different momentum or frequency dependence, labeling comes into play and the entanglement will be weaker, the more so the larger the integration ranges. We note that the six-fold momentum and frequency integration, acting on the rather complicated function  $\Phi_{HV}^* \Phi_{VH}$ , makes the evaluation of Eq. (2.8) not as transparent as one would wish. For a more convenient description of polarization entanglement, the biphoton amplitude function  $\Phi_{HV}$  is often simplified as the product of the pump field profile and the phase matching function only, thereby omitting the contribution of the two-photon propagation. We note that this is strictly correct only in the far-field limit.

### 2.3.2 Limitations to the degree of polarization entanglement

In general, the entanglement in one of the three degrees of freedom, being polarization, transverse momentum and frequency, will be affected by the dependence of the amplitude function  $\Phi$  on the other two degrees of freedom and the integration over these variables. The complicated six-fold integration in Eq. (2.8) for example describes how the spatial and frequency labeling information, contained in the amplitude functions  $\Phi_{HV}$  and  $\Phi_{VH}$ , affects the obtained

polarization entanglement. In Chapter 7 we will discuss in more detail how the four-fold momentum integration will lead to lower degrees of polarization entanglement if the integration extends to larger apertures. As soon as detection occurs behind single-mode fibers instead of apertures, the spatial information will be reduced to that of a single transverse mode, the spatial labeling will thus disappear, and Eq. (2.8) will contain only a two-fold frequency integration. The degree of polarization entanglement is then no longer limited by the aperture size but only by the detected spectral bandwidth of the filters.

### 2.3.3 Experimental scheme for measurement of polarization entanglement

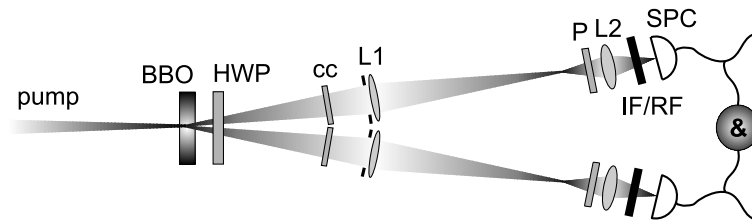


**Figure 2.4:** Experimental setup for measuring polarization entanglement.

In Fig. 2.4 we show the detailed experimental setup that we typically employ to generate and detect polarization-entangled photons. A krypton ion laser, operating at 407 nm, produces a light beam that is weakly focused (typical beam waist  $\approx 0.3$  mm) onto a 1-mm-thick non-linear  $\chi^{(2)}$  crystal made of  $\beta$ -barium borate (BBO). The perpendicular intersections of the generated SPDC cones are realized by a proper tilt of the crystal. These intersections form the two paths along which all optics are placed. A half-wave plate HWP, oriented at  $45^\circ$  with respect to the crystal axes, and two 0.5-mm-thick BBO crystals (*cc*) form the device that compensates for both the longitudinal and transverse walk-off built up between the ordinary and extra-ordinary light in the birefringent crystal. By tilting one of these two compensating crystals we can set the overall phase factor of the two-photon state which allows us to operate either in the singlet or one of the triplet states. The two light beams pass  $f = 40$  cm lenses ( $L_1$ ) at 80 cm from the down-conversion crystal and propagate over an additional 120 cm before being focused by  $f = 2.5$  cm lenses ( $L_2$ ) onto free-space single-photon counters SPC (Perkin Elmer SPCM-AQR-14). Spatial selection of the crossings is performed by circular apertures with variable diameter in front of the lenses  $L_1$ . Spectral selection is accounted for by interference filters IF ( $\Delta\lambda = 10$  nm FWHM centered around 814 nm) and red filters RF in front of the photon counters. Polarizers  $P$  are used for polarization selection. The output signals of the photon counters are combined in an electronic circuit that registers coincidence counts (simultaneous clicks) within a time window of 1.76 ns. This time window is sufficiently small to detect the individual photons of a single pair only, but is also much larger than the coherence time of the two-photon wavepacket, which is proportional to the inverse bandwidth of the interference filters and typically 0.1 ps (at  $\Delta\lambda = 10$  nm).

The above description of the experimental setup is just a general one. Slight modifications of this general scheme are required for specific studies on polarization-entanglement, using

different crystal thicknesses, pump foci and fiber-coupled photon counters, as presented in Chapter 4, Chapter 6 and Chapter 7, respectively.

In a typical measurement of the degree of polarization entanglement, we measure the coincidence count rates for an orthogonal and a parallel polarizer setting. These settings are reached by fixing one polarizer at  $+45^\circ$  and rotating the other to  $-45^\circ$  and  $+45^\circ$ , respectively. When we operate in the two-photon singlet state, we expect to measure a maximal coincidence rate  $R_{\max}$  for the orthogonal setting and a minimum rate  $R_{\min}$  for the parallel setting. In fact, the coincidence rate measured as a function of the orientation of the rotating polarizer is a sinusoidal fringe pattern that corresponds to the two-photon interference. The degree of polarization entanglement [see Eq. (2.8)] can now be experimentally measured by the two-photon fringe visibility, given by

$$V_{45^\circ} = \frac{R_{\max} - R_{\min}}{R_{\max} + R_{\min}}. \quad (2.9)$$

## 2.4 Spatial entanglement

### 2.4.1 The spatially entangled state

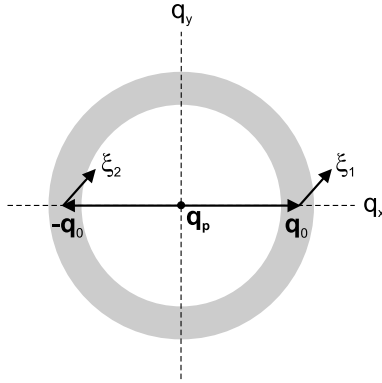


**Figure 2.5:** Transverse momenta of pair-photons 1 and 2 generated under type-I SPDC.

For the study of spatial entanglement, we consider type-I phase matching (one polarization) and monochromatic light ( $\omega_1 = \omega_2$ ). The two-photon state in Eq. (2.1) then changes into

$$|\Psi\rangle = \int d\mathbf{q}_1 \int d\mathbf{q}_2 \Phi(\mathbf{q}_1, \mathbf{q}_2) |\mathbf{q}_1, \mathbf{q}_2\rangle. \quad (2.10)$$

At first sight, Eq. (2.10) does not represent a spatially-entangled state as the amplitude function  $\Phi(\mathbf{q}_1, \mathbf{q}_2)$  seems to lack the symmetry property shown in Eq. (2.7) for the polarization-entangled state. The reason is that the continuous momentum variables  $\mathbf{q}_1$  and  $\mathbf{q}_2$  are not limited to two discrete values, as was the case for the polarizations  $H$  and  $V$ . By definition, the spatial entanglement is then contained in the non-separability of the amplitude function, i.e.,  $\Phi(\mathbf{q}_1, \mathbf{q}_2) \neq f(\mathbf{q}_1)g(\mathbf{q}_2)$ , rather than in the symmetry of  $\Phi$ . However, the

symmetry of  $\Phi(\mathbf{q}_1, \mathbf{q}_2)$  does emerge once we linearize the momenta around  $\mathbf{q}_0$  and  $-\mathbf{q}_0$ , being the transverse momenta associated with the central axes of beam 1 and 2, respectively (see Fig. 2.5). The momenta  $\mathbf{q}_1$  and  $\mathbf{q}_2$  are then given by  $\mathbf{q}_0 + \boldsymbol{\xi}_1$  and  $-\mathbf{q}_0 + \boldsymbol{\xi}_2$ , respectively, where  $|\boldsymbol{\xi}_{1,2}| \ll |\mathbf{q}_0|$ . Furthermore, we define  $\Phi_{12}(\boldsymbol{\xi}_1, \boldsymbol{\xi}_2) \equiv \Phi(\mathbf{q}_0 + \boldsymbol{\xi}_1, -\mathbf{q}_0 + \boldsymbol{\xi}_2)$  and  $\Phi_{21}(\boldsymbol{\xi}_1, \boldsymbol{\xi}_2) = \Phi_{12}(\boldsymbol{\xi}_2, \boldsymbol{\xi}_1) \equiv \Phi(\mathbf{q}_0 + \boldsymbol{\xi}_2, -\mathbf{q}_0 + \boldsymbol{\xi}_1)$ . The pair-photons are fully indistinguishable in momentum, and thus spatially entangled, if the amplitude function  $\Phi(\mathbf{q}_1, \mathbf{q}_2)$  is invariant to the exchange of the local variables  $\boldsymbol{\xi}_1$  and  $\boldsymbol{\xi}_2$  [36], i.e., if  $\Phi_{12}(\boldsymbol{\xi}_1, \boldsymbol{\xi}_2) = \Phi_{21}(\boldsymbol{\xi}_1, \boldsymbol{\xi}_2)$ .

Analogous to the case of polarization entanglement, the spatial entanglement is again quantified by the overlap between the amplitude functions  $\Phi_{12}$  and  $\Phi_{21}$ . In Chapter 8 we will study the spatial interference of these amplitude functions in a two-photon experiment that employs a so-called Hong-Ou-Mandel (HOM) interferometer [27]. In this interferometer photon coincidences are measured only when the two incident photons are either both reflected or both transmitted at the beamsplitter. These two probability channels are represented by  $\Phi_{12}$  and  $\Phi_{21}$  and, in essence, probed by a switch in beam labels. The degree of spatial entanglement is therefore given by

$$V_{\text{spat}} = \frac{\langle 2\text{Re}\{\Phi_{12}^* \Phi_{21}\} \rangle}{\langle |\Phi_{12}|^2 + |\Phi_{21}|^2 \rangle}. \quad (2.11)$$

The single brackets now denote the integration over the local momenta  $\boldsymbol{\xi}_1$  and  $\boldsymbol{\xi}_2$  only. In case of non-monochromatic light ( $\omega_1 \neq \omega_2$ ), double brackets should be introduced as we then have to integrate over frequencies as well. Equation (2.11) shows that we again obtain maximal entanglement if the biphoton amplitudes are symmetric under exchange of the beam labels.

## 2.4.2 State representation in a modal basis

The spatially-entangled state in Eq. (2.10) is represented in a plane-wave basis of two-photon states  $|\mathbf{q}_1, \mathbf{q}_2\rangle$  that are expressed in the continuous momentum variables  $\mathbf{q}_1$  and  $\mathbf{q}_2$ . As an alternative, this entangled state can also be represented in a modal basis of discrete eigenstates  $\psi_{ni}$  with  $i=1$  or  $2$  [34, 38, 39]. In this basis, Eq. (2.1) can be written as the inseparable state

$$|\Psi\rangle = \sum_n \Phi_n |\psi_{n1}\rangle |\psi_{n2}\rangle, \quad (2.12)$$

which represents a superposition of (separable) product states  $|\psi_{n1}\rangle |\psi_{n2}\rangle$ . The index  $n$  refers to the modal indices of the eigenfunctions that form a complete orthonormal set of solutions for the paraxial wave equation in a specific beam direction [40]. If we use the set of Laguerre-Gaussian (LG) modes, we can define  $n$  as  $n \equiv (l, p)$  where  $l$  and  $p$  are the azimuthal and radial LG polynomial indices that label the transverse profile of the light beam. The spatial entanglement that is hidden in the inseparable character of Eq. (2.12) simply becomes transparent from the measurement projection. The spatial mode of each individual pair-photon is unknown beforehand, but measurement of the mode of one photon fixes the mode of its partner photon.

## **2.5 Concluding remarks**

In this chapter we have described the process of spontaneous parametric down-conversion (SPDC) as a source of quantum-entangled photons. We have used the generated two-photon state as the basis for an analogous description of polarization and spatial entanglement in general. Elsewhere in this thesis, we will present the specific consequences of the crystal thickness (Chapter 4), focused pumping (Chapter 6) and fiber-coupled detection (Chapter 7) on the polarization entanglement. For a detailed study of spatial entanglement that originates from HOM interference we refer to Chapters 8 and 9.

## CHAPTER 3

---

### Simple method for accurate characterization of birefringent crystals

---

*We present a simple method to determine the cutting angle and thickness of birefringent crystals. Our method is based upon chromatic polarization interferometry and allows for accuracies of typically  $0.1^\circ$  in the cutting angle and 0.5% in the thickness.*

*P.S.K. Lee, J.B. Pors, M.P. van Exter, and J.P. Woerdman, *Appl. Opt.* **44**, 866-870 (2005).*

### 3.1 Introduction

Birefringent crystals play a key role in various optical applications ranging from polarization manipulations in linear optics to frequency conversion in nonlinear optics. As the specification of ready-made crystal slabs is often limited by manufacturing tolerances, accurate inspection after production is usually required. Properties of birefringent materials are generally characterized by applying interferometric [41–44] or ellipsometric techniques [45–47]. All these techniques enable one to determine the axes of orientation or the refractive indices (or both) of the birefringent material, but not its thickness (apart from [47]). We present here a simple method for simultaneous determination of both the precise cutting angle and thickness of a birefringent crystal. Our method uses the refractive indices of the crystal as input, since these indices are already well-known to high precision for most of the relevant crystals [48]. We combine this input with chromatic polarization interferometry to determine precisely the absolute order of the crystal (acting as a waveplate) at several angles of incidence.

### 3.2 Theory

When considering plane-wave illumination of a uniaxial waveplate, the accumulated phase difference  $\Delta\phi$  between the ordinary and extraordinary light upon propagation through a birefringent crystal is given by

$$\Delta\phi = d(k_{o,z} - k_{e,z}), \quad (3.1)$$

where  $d$  is the crystal thickness and  $k_{o,z}$ ,  $k_{e,z}$  are the internal longitudinal wavevector components of the ordinary and extraordinary light in the ( $z$ -)direction parallel to the surface normal. In detail, the wavevector components are given by

$$k_{o,z} = k_0 \sqrt{n_o^2(\lambda) - \sin^2(\theta)} \quad (3.2)$$

$$k_{e,z} = k_0 \sqrt{n_e^2(\lambda, \Theta) - \sin^2(\theta)} \quad (3.3)$$

where  $k_0 = 2\pi/\lambda$  is the wavevector of the incoming beam,  $\theta$  is the angle of incidence and  $n_o(\lambda)$  and  $n_e(\lambda, \Theta)$  are the refractive indices at the specified wavelength  $\lambda$  and angle  $\Theta$ , with

$$\frac{1}{n_e(\Theta)} = \sqrt{\frac{\cos^2 \Theta}{n_o^2} + \frac{\sin^2 \Theta}{n_e^2}}. \quad (3.4)$$

Here,  $\Theta = \theta_c + \theta'$  is the angle between  $\vec{k}_e$  and the crystalline  $c$ -axis,  $\theta_c$  is the cutting angle (= angle between  $c$ -axis and surface normal), and  $\theta'$  is the internal refraction angle. All relevant angles are indicated in Fig. 3.1.

Despite the simplicity of the above equations, the analysis of data obtained from chromatic polarization interferometry requires some thought. Experimentally, we measure the wavelength-dependent optical transmission  $T$  of the waveplate when it is positioned between two parallel polarizers. By fitting the measured spectral fringe pattern with the theoretical

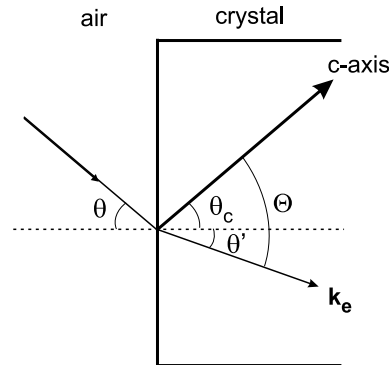


**Figure 3.1:** Definition of the relevant angles: angle of incidence  $\theta$ , internal angle of refraction  $\theta'$ , crystalline cutting angle  $\theta_c$ , and internal angle  $\Theta$ .

expression [49]  $T = a \cos^2\{\Delta\phi(\lambda, \theta = 0)/2\} + b$ , with  $a$  and  $b$  constant, we can extract not only the fractional but also the *integer* order of the waveplate for any specific wavelength  $\lambda_0$  (total order is  $\Delta\phi(\lambda_0)/2\pi$ ).

Another issue is the dependence of  $\Delta\phi$  on both crystal cutting angle  $\theta_c$  and thickness  $d$ . A single polarization-resolved transmission spectrum contains insufficient information to determine both  $\theta_c$  and  $d$  individually, as a variation of one parameter can be largely compensated for by a change in the other parameter. The basis for this approximate interchangeability of  $\theta_c$  and  $d$  is the observation that Eq. (3.4) is well approximated by its first-order Taylor expansion (as  $|n_o - n_e| \ll n_o$ ), making the refractive index difference  $\Delta n(\lambda, \Theta) \equiv n_o(\lambda) - n_e(\lambda, \Theta) \approx \Delta n(\lambda, \Theta = 90^\circ) \times \sin^2 \Theta$ . As a result  $\Delta n(\lambda, \theta_c)$  shows a similar wavelength dependence at various cutting angles and differences occur primarily in the prefactor.

To find the individual values of  $\theta_c$  and  $d$  we measure a set of polarization-resolved transmission spectra at various angles of incidence  $\theta$ . We analyze the spectra obtained at non-normal incidence by using the interchangeability mentioned above: we fit the polarization-resolved transmission spectrum at each incident angle  $\theta$  by that of a fictitious crystal of effective thickness  $d_{\text{eff}}(\theta)$  illuminated at normal incidence, i.e., we write  $\Delta\phi(\lambda, \theta) \approx 2\pi d_{\text{eff}}(\theta) \times \Delta n(\lambda, \Theta = \theta_c)/\lambda$ . This trick yields a single fitting parameter  $d_{\text{eff}}(\theta)$  for every spectrum. As a last step in our analysis we combine the data of all spectra, by plotting  $d_{\text{eff}}(\theta)$  (or actually the phase difference  $\Delta\phi(\lambda_0, \theta)$  at a fixed wavelength  $\lambda_0$ ) versus  $\theta$  and fitting it with the appropriate expression to extract both the real  $\theta_c$  and  $d$  individually.

With the above trick we avoid the problem that a single spectrum can be fitted with many different  $(\theta_c, d)$  combinations. The only alternative to our simplified procedure would be a single combined fit of *all* measured spectra. However, such a fit is much more cumbersome.

A nasty detail of every method of analysis is the conversion from external to internal angles; in order to find the internal angle  $\Theta = \theta_c + \theta'$  for a given external angle  $\theta$  and cutting angle  $\theta_c$ , Snell's law  $\sin \theta = n_e(\lambda, \Theta) \sin \theta'$  has to be solved iteratively, since  $\Theta$  itself depends on  $\theta'$ . In practice, three iterations are sufficient to find all angles with an error  $< 0.0001^\circ$ . As a typical example we take  $\theta_c = 24.9^\circ$ ,  $\theta = 25^\circ$ ,  $n_o = 1.66736$  and  $n_e = 1.55012$ ; we find then on the first iteration  $\theta'_1 = \arcsin\{\sin \theta / n_e(\Theta = \theta_c)\} = 14.89^\circ$  and  $\Theta_1 = 39.79^\circ$ , on the second iteration  $\theta'_2 = \arcsin\{\sin \theta / n_e(\Theta_1)\} = 15.158^\circ$  and  $\Theta_2 = 40.058^\circ$ , on the third

iteration  $\theta'_3 = \arcsin\{\sin \theta / n_e(\Theta_2)\} = 15.164^\circ$  and  $\Theta_3 = 40.064^\circ$  and the same to within  $0.0001^\circ$  on the fourth iteration. The advantage of our two-step fit procedure is that these iterations are necessary only in the final fit of  $\Delta\phi(\lambda_0, \theta)$  versus  $\theta$ . For the alternative approach of a single complete fit of all data an enormous amount of iterations in the 2-dimensional  $(\lambda, \theta)$  space is needed.

### 3.3 Experimental setup

Figure 3.2 shows the experimental setup. An incandescent lamp (GE 1460X) produces a beam which is directed through two apertures (spaced by 10 cm, each 5 mm diameter) in order to limit its divergence. Note that no lenses have been placed in the beamline. The birefringent BBO crystal (specified cutting angle  $\theta_c = 24.9^\circ \pm 0.5^\circ$  and specified thickness  $d = 1.0 \pm 0.1$  mm) is positioned between two parallel polarizers and placed in a rotation stage in such a way that the crystalline optical axis can be rotated in the horizontal plane. A 200  $\mu\text{m}$  diameter optical fiber guides the collected light to a fiber-coupled miniature grating spectrometer (Ocean Optics S2000), which contains a high-sensitivity CCD array for quick and easy measurement of a complete spectrum.

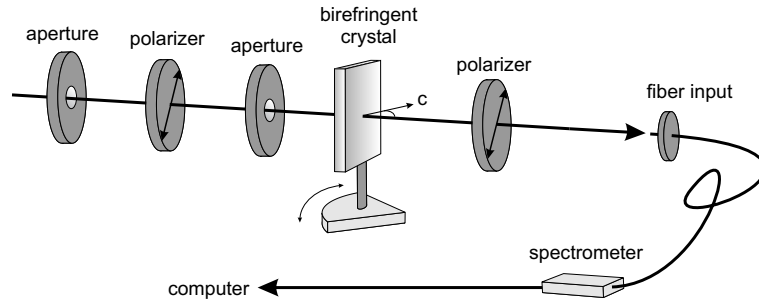


**Figure 3.2:** Experimental setup used to measure the optical transmission spectrum of a birefringent crystal sandwiched between two parallel polarizers. Light from an incandescent lamp (not shown) is passed through apertures (to limit its divergence) and the crystal before being spectrally analyzed by a fiber spectrometer. The crystalline  $c$ -axis can be rotated in the horizontal plane with an accurate rotation mount.

In order to generate the phase difference between the ordinary and extraordinary ray, we first orient the crystal's  $c$ -axis in the horizontal plane, using both polarizers initially in a horizontal-vertical crossed configuration. The polarizers are then rotated to the  $45^\circ$  setting to get maximum fringe contrast in polarization-resolved transmission.

Since we measure at angles of incidence up to  $30^\circ$ , we paid attention to position the crystal properly along the axis of the rotation stage to avoid (partial) cut off of the light beam by the crystal holder. The scale of the rotation stage is calibrated regarding its zero setting by carefully observing the reflection at normal incidence. Hereby, we could get an accuracy of the zero setting of  $0.1^\circ$ , which is also the accuracy the scale offers for angle measurement.

We operate our spectrometer in the transmission mode, in which the wavelength-dependent light intensity is normalized to the spectrometer signal obtained in the absence of the

crystal. Since this latter signal is relatively weak for wavelengths below roughly 350 nm, the measured signal in the transmission mode is very noisy in this spectral regime. For this reason, we measure in the wavelength domain 400-875 nm, though the fiber spectrometer can operate in the regime 200-875 nm.

### 3.4 Measurements and results

The experimental part of our method consists of measuring wavelength-dependent transmission spectra  $T(\lambda, \theta)$  of the BBO crystal for several angles of incidence  $\theta$ . Figure 3.3 shows a typical optical transmission spectrum  $T(\lambda)$ , measured at normal incidence ( $\theta = 0$ ). The modulation depth of the experimentally observed fringes is limited to only  $\approx 80\%$  for  $\lambda > 800$  nm and smoothly decreases to  $\approx 30\%$  at  $\lambda = 500$  nm. We attribute this limitation to the finite opening angle of the light beam, which is approximately  $0.7^\circ$  and mainly determined by the second aperture (5-mm diameter) positioned at 40 cm from the ( $200 \mu\text{m}$  diameter) detecting fiber. Multi-beam interference [50] does not play a major role in our experiment since it requires plane-wave illumination, whereas our light source has a finite opening angle and is spatially incoherent.

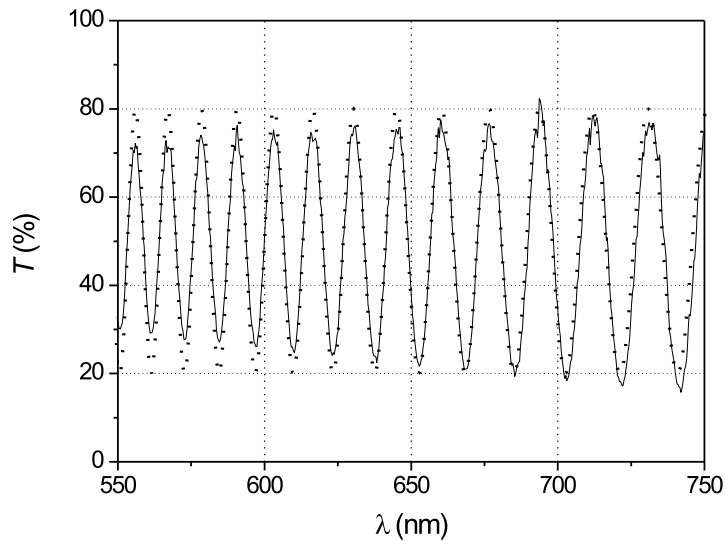


**Figure 3.3:** Optical transmission spectrum  $T(\lambda)$  of our BBO crystal, which is sandwiched between two parallel polarizers. The measured curve (solid) was taken at normal incidence ( $\theta = 0$ ); its best fit (dotted) was found for  $d_{\text{eff}} = 1124 \mu\text{m}$  and  $\theta_c = 24.7^\circ$  via the expression  $T = a \cos^2[\Delta\phi(\lambda, \Theta = \theta_c)/2] + b$ . Note that we present only a part of the full pattern to limit the number of displayed fringes.

Next, each transmission spectrum is fitted by using the  $\theta=0$  expression for the phase

difference, i.e.,  $\Delta\phi(\lambda, \theta) \approx 2\pi d_{\text{eff}}(\theta)\Delta n(\lambda, \Theta = \theta_c)/\lambda$ , with the thickness  $d_{\text{eff}}(\theta)$  acting as fitting parameter and  $\theta_c$  fixed at the *specified* value of  $24.9^\circ$ , which could differ from the real cutting angle. For the spectrum measured at normal incidence,  $d_{\text{eff}} = 1124 \mu\text{m}$  gives a perfect fit of the fringe period and phase (dotted curve in Fig. 3.3); a precise fit of the fringe amplitudes is not relevant in our analysis. For spectra taken at non-normal incidence (not shown) the fit is not always perfect, simply because the  $\theta = 0$  expression is just an approximation, though a good one, for the cases  $\theta \neq 0$ . To still obtain the correct order  $\Delta\phi(\lambda_0, \theta)/2\pi$  at a specific wavelength  $\lambda_0$ , we have to fit with an effective thickness  $d_{\text{eff}}$  such that experimental curve and fit are exactly in phase at this wavelength (fractional order), while both curves contain an equal number of fringes (= integer order) in the wavelength domain  $[\lambda_0, \infty]$ . For  $\lambda_0$  we choose a fixed value of 644 nm, because it is located in the center of our spectral range and accurate refractive index data at this wavelength is available [48]:  $n_o = 1.66736$  and  $n_e = 1.55012$ .

The described fitting procedure works well because we use accurate (at least four decimals) values for the refractive indices  $n_o$  and  $n_e$ , as tabulated for some wavelengths at  $T = 293 \text{ K}$  in [48] (originally from [51]). Due to the small temperature sensitivity ( $\approx 10^{-5} \text{ K}^{-1}$ ) of the refractive indices, temperature fluctuations within 5 K have negligible effect on the refractive index difference, which is of the order of 0.05. The mentioned tabulated values for  $n_o$  and  $n_e$  served as input to calculate data points for  $\Delta n(\lambda, \Theta = \theta_c)$ , which are then fitted with the standard dispersion relation (normally used for  $n$ ) to obtain the full wavelength dependence of  $\Delta n(\lambda, \Theta = \theta_c)$  necessary for fitting the observed spectral fringe pattern.

Figure 3.4(a) shows the measured order of waveplate  $\Delta\phi(\lambda_0, \theta)/2\pi$  as a function of the incidence angle  $\theta$ , where each point results from a single spectral measurement. These points are fitted by using the full ( $\theta \neq 0$ ) Eqs. (3.1-3.4) with cutting angle  $\theta_c$  and thickness  $d$  as fitting parameters and  $\lambda$  fixed at  $\lambda_0 = 644 \text{ nm}$ , thereby getting the proper internal angle  $\Theta$  for each  $\theta$  via iterations. The set of fitting parameters which produces the best fit (solid curve) now gives us the real cutting angle and thickness of our BBO crystal, being  $\theta_c = 24.95^\circ \pm 0.1^\circ$  and  $d = 1105 \pm 5 \mu\text{m}$ . To demonstrate the influence of the fit parameters, we have also plotted two other fits. The dashed curve shows how a change in  $\theta_c$  (to  $\theta_c = 19.95^\circ$ , keeping  $d = 1105 \mu\text{m}$ ) leads to something like a horizontal shift of the best fit. The dotted curve shows how an additional change in  $d$  leads to a simple and exact scaling in the vertical direction. The new (and incorrect) fit parameters ( $\theta_c = 19.95^\circ$ , and  $d = 1680 \mu\text{m}$ ) are chosen such that they give the same order of waveplate  $\Delta\phi(\lambda_0)/2\pi$  at normal incidence.

To determine the best fit of the data points shown in Fig. 3.4(a), we have calculated the normalized  $\chi^2 = \sum_{i=1}^N \delta_i^2 / (N - 2)$  for various sets of fitting parameters  $\theta_c$  and  $d$  (see Table 3.1). Here,  $N$  is the number of data points and  $\delta_i$  are the residuals between data points and fit which, for the best fit, are randomly spread around zero with a standard deviation of 0.10 [see Fig. 3.4(b)]. Besides the real cutting angle  $\theta_c$  and thickness  $d$  of the crystal (minimal  $\chi^2$ ), Table 3.1 also indicates that our method allows for determination accuracies of  $0.1^\circ$  for  $\theta_c$  and  $0.5\%$  for  $d$ .

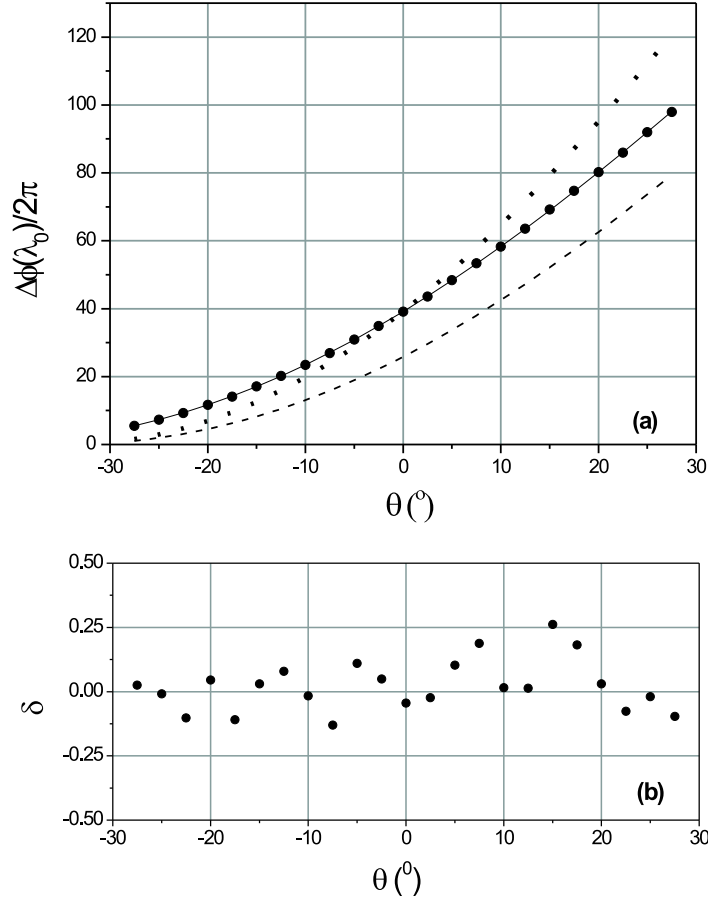


**Figure 3.4:** (a) Order of the waveplate  $\Delta\phi(\lambda_0, \Theta)/2\pi$  at  $\lambda_0 = 644$  nm as a function of the angle of incidence  $\theta$ . The dots are experimental values obtained from fits like the one shown in Fig. 3.3. The solid, dashed and dotted curves are parametric fits (see text for details). (b) Residuals  $\delta$  between experimental points and best fit shown in (a). The residuals are randomly spread around zero with standard deviation of 0.10.

### 3.5 Discussion

As this chapter stresses the high accuracy of our method, we will separately discuss the possible errors in the horizontal and vertical scale of Fig. 3.4(a). The error in the determined angle of incidence  $\theta$  comes, in the first place, from the scale accuracy of the rotation stage, being  $0.1^\circ$ . In addition,  $\theta$  can exhibit a systematic error of  $0.1^\circ$  due to the limited accuracy in the calibration of the zero setting of this scale, resulting in a total error in  $\theta$  of  $0.2^\circ$ . As a consequence of Snell's law, the error in the internal refraction angle is a factor  $n$  smaller.

**Table 3.1:** Normalized  $\chi^2$  as calculated for various cutting angles  $\theta_c$  and thicknesses  $d$ .

$d(\mu\text{m}), \theta_c$	24.85°	24.90°	24.95°	25.00°
1100	0.301	0.170	0.079	0.145
1105	0.106	0.038	0.010	0.022
1110	0.023	0.018	0.054	0.130
1115	0.050	0.109	0.209	0.351

Inaccuracy in the measured order of the waveplate  $\Delta\phi(\lambda_0)/2\pi$  comes from improper matching of the experimental curve and fit at  $\lambda_0$  in the fitting procedure shown in Fig. 3.3. The potential mismatch is, however, not more than a few times  $10^{-2}$  of a fringe, which implies that  $\Delta\phi(\lambda_0)/2\pi$  has its error only in the second decimal and can thus be determined more accurately than  $\theta$ . As we use a simplified fitting procedure (based on  $d_{\text{eff}}$ ), there is a small risk, particularly for large  $\theta$ , that we miscount  $\Delta\phi(\lambda_0)/2\pi$  by a full integer unit due to a miscalculation of the number of fringes in the range  $[\lambda_0, \infty]$ . Fortunately, such gross errors show up immediately in Fig. 3.4(b) and can thus be easily corrected for.

As an alternative check for the cutting angle, but not for the crystal thickness, we have also used our BBO crystal for type-I second harmonic generation. Starting from a weakly focused laser beam at a wavelength of  $\lambda_L = 980$  nm, we found optimum conversion to 490 nm at a measured angle of incidence of  $1.2^\circ \pm 0.1^\circ$ , corresponding to an internal angle of  $\theta' = 0.7^\circ$ . With a free software package [52], we determined the angle  $\Theta$  for optimum conversion [phase-matched by  $n_o(\lambda_L) = n_e(\lambda_L/2, \Theta)$ ] to be  $\Theta = 24.3^\circ$ . Adding the two values mentioned above leads to a cutting angle  $\theta_c = 25.0^\circ$ , which agrees well with the value found with our method.

As a test of our method, we have also determined the precise cutting angle and thickness of a second crystal (with specified values  $\theta_c = 41.8^\circ \pm 0.5^\circ$  and  $d = 200 \pm 20 \mu\text{m}$ ). Table 3.2 summarizes the results of a series of spectral measurements by giving  $\chi^2$  for various  $\theta_c$  and  $d$ . This leads to an actual cutting angle  $\theta_c = 41.0 \pm 0.1^\circ$  and thickness  $d = 238.5 \pm 0.5 \mu\text{m}$ . These small error tolerances are in good agreement with those found with our first crystal, and once more confirm the high accuracy of our method.

We stress that the simplicity of our method is due to the use of well-known refractive indices as input. In solid state optics, characterization of newly developed crystals cannot benefit from this method, as their refractive indices are still unknown, and a much more extensive method is needed. Such a method has been developed by Hecht *et al.* [47], where ellipsometric and polarization transmission intensity measurements are simultaneously analyzed to determine the optical properties of a specific crystal. In addition to its simplicity, our method also allows for easy measurement of any practical crystal thickness, contrary to what is reported in Ref. [47].

**Table 3.2:** Normalized  $\chi^2$  for a second crystal as calculated for various cutting angles  $\theta_c$  and thicknesses  $d$ .

$d(\mu\text{m}), \theta_c$	40.85°	40.90°	40.95°	41.00°	41.05°	41.10°
237.5	0.0322	0.0210	0.0124	0.0063	0.0028	0.0019
238.0	0.0183	0.0102	0.0046	0.0016	0.0012	0.0034
238.5	0.0086	0.0036	0.0011	0.0012	0.0039	0.0091
239.0	0.0032	0.0012	0.0018	0.0050	0.0108	0.0192
239.5	0.0019	0.0030	0.0068	0.0131	0.0220	0.0335

### 3.6 Conclusions

In this chapter, we have presented a simple method, based upon chromatic polarization interferometry, to determine the cutting angle and thickness of birefringent crystals. In spite of its simplicity, the method allows for accuracies of  $0.1^\circ$  in the cutting angle and 0.5% in the thickness, which are generally much smaller values than specified by the manufacturer.

In the present experiment, these accuracies are limited by the quality of the rotation mount. This is, however, not a fundamental limitation. With a more accurate mount, in combination with a better alignment scheme and a less divergent optical beam, even higher accuracies are expected.

3. Simple method for accurate characterization of birefringent crystals

## CHAPTER 4

---

### Increased polarization-entangled photon flux via thinner crystals

---

*We analyze the scaling laws that govern the production of polarization-entangled photons via type-II spontaneous parametric down-conversion (SPDC). We demonstrate experimentally that thin nonlinear crystals can generate a higher number of entangled photons than thicker crystals, basically because they generate a broader spectrum.*

*P.S.K. Lee, M.P. van Exter, and J.P. Woerdman, Phys. Rev. A **70**, 043818 (2004).*

## 4.1 Introduction

Spontaneous parametric down-conversion (SPDC) has become the standard tool to generate entangled photon pairs for experimental studies on the foundations of quantum mechanics [6–8]. These photon pairs can be simultaneously entangled in energy, momentum, and polarization (for type-II SPDC), but the use of polarization entanglement is most popular due to its simplicity. Although the mathematical description of the generating process is well known [20, 35], we think that its physical implications are not yet fully exploited. We hereby refer specifically to the thickness of the nonlinear crystal, which for BBO is generally chosen between 0.5-3 mm without any further justification [8, 23]. In this paper, we will discuss the role of the crystal thickness in terms of simple scaling laws and show that the production rate of entangled pairs can actually be increased considerably by *reducing* the crystal thickness (to 0.25 mm in our case). Our treatment is restricted to the case of a cw pump, but can be extended to pulsed pumping.

The theoretical description of type-II SPDC is centered around the two-photon wave function  $\Phi(\mathbf{q}_o, \mathbf{q}_e; \omega_o, \omega_e)$ , which quantifies the probability amplitude to generate a photon pair with transverse momentum  $\mathbf{q}_i$  and frequency  $\omega_i$ , for the ordinary ( $i = o$ ) and extra-ordinary ( $i = e$ ) polarization, respectively. Stripped down to its bare essentials this two-photon wave function is

$$|\Phi(\mathbf{q}_o, \omega_o; \mathbf{q}_e, \omega_e)| \propto L \text{sinc}(\Delta\phi), \quad (4.1)$$

where  $L$  is the crystal thickness,  $\text{sinc}(x) = \sin(x)/x$ , and  $\Delta\phi = L\Delta k$  is the phase mismatch. If the pump laser is an almost plane-wave beam at normal incidence, conservation of energy and transverse momentum requires that  $\omega_o + \omega_e = \omega_p$  and  $\mathbf{q}_o + \mathbf{q}_e = \mathbf{0}$ , and  $\Delta\phi$  becomes a function of one frequency and transverse momentum only. This functional dependence is such that the two polarized components are emitted in angular cones that are displaced with respect to the pump over an angle  $\pm\theta_{\text{off}}$  and that are approximate mirror images of each other (at  $\omega_o \approx \omega_e$ ). We consider SPDC emission close to frequency degeneracy, where  $\omega_e \equiv \omega_p/2 + \delta\omega_e$  with  $\delta\omega_e \ll \omega_p/2$  and  $\omega_p$  as pump frequency, and linearize the phase mismatch around an orthogonal crossing of the two SPDC cones (set by the crystal angle) to [35, 48]

$$\Delta\phi = L\Delta k \approx \left( \frac{\partial\Delta k}{\partial\omega_e} \delta\omega_e + \frac{\partial\Delta k}{\partial\theta_x} \delta\theta_x + \frac{\partial\Delta k}{\partial\theta_y} \delta\theta_y \right) L \approx 2\pi \left( -\frac{\delta\lambda_e}{\Delta\lambda_{\text{SPDC}}} + \frac{\delta\theta_r}{\Delta\theta_{\text{SPDC}}} \right), \quad (4.2)$$

where  $\delta\theta_r$  measures the angle change in the radial direction. As the partial derivatives of  $\Delta k$  are determined by material constants, both the spectral width  $\Delta\lambda_{\text{SPDC}}$  (at fixed angle) and the angular width  $\Delta\theta_{\text{SPDC}}$  (at fixed frequency) are inversely proportional to the crystal thickness  $L$ . More specifically, the product  $\Delta\lambda_{\text{SPDC}} \times L \approx \lambda^2/[n_{gr,o} - n_{gr,e}(\theta)]$  (with  $\lambda = 2\lambda_p$ ) depends on the difference between two group refractive indices [53], whereas the product  $\Delta\theta_{\text{SPDC}} \times L = \lambda/\sqrt{2}\rho$  depends on the internal walk-off angle  $\rho$ .

Typical numbers for type-II SPDC in BBO, where down-conversion from 407 to 814 nm requires a cut-angle of about  $41.2^\circ$ , are as follows. Conversion of the literature values for the refractive indices to group indices gives  $\Delta\lambda_{\text{SPDC}} \times L \approx 11.5 \text{ nm.mm}$ . With an internal

walk-off angle  $\rho = 72$  mrad (corresponding to an offset angle  $\theta_{\text{off}} = 57$  mrad), the product  $\Delta\theta_{\text{SPDC}} \times L \approx 8.0$  mrad.mm. Note that  $\Delta\lambda_{\text{SPDC}}$  and  $\Delta\theta_{\text{SPDC}}$  are specified in terms of the width of the SPDC signal from its peak value to the first minimum of its sinc<sup>2</sup>-shaped intensity profile, making the full widths at half maximum (FWHMs) 0.89 times as large.

The simple equations (4.1) and (4.2) already present the essential scaling behavior of SPDC. For a fixed and sufficiently small detection bandwidth and opening angle, Eq. (4.1) shows that the number of detected photon pairs ( $\propto |\Phi|^2$ ) scales as  $L^2$  and thereby increases rapidly with crystal thickness. However, as the angular width of the SPDC rings is proportional to  $1/L$ , the useful crossing areas scale as  $1/L^2$  and the number of photon pairs within these areas (and within a fixed spectral bandwidth) is independent of the crystal thickness. Furthermore, as the SPDC bandwidth is also proportional to  $1/L$  the spectrally-integrated power is expected to scale as  $1/L$ , being considerably larger for a thin crystal than for a thicker one.

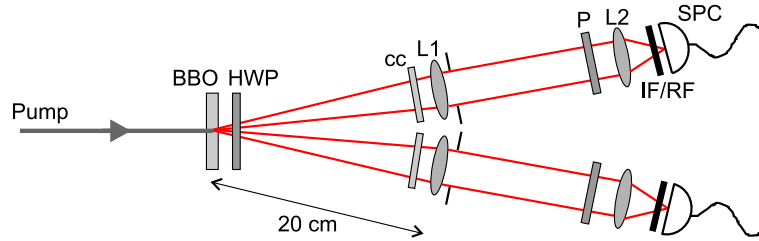
The scaling behavior described above should work not only for free-space detection behind apertures but also for fiber-coupled detectors, under the condition that three relevant transverse sizes are matched [23]. Specifically, optimum collection efficiency is obtained when the size of the backward propagated fiber mode is matched to the size of the pump spot. Both these sizes should be roughly equal to the transverse beam walk-off  $L\rho$  to create the best overlap between the SPDC emission and the fiber mode. Under these matching conditions the spectrally-integrated photon yield for a fiber-coupled system should also scale as  $1/L$  [54]. In this chapter, we will present experimental data for free-space detection only.

For pulsed instead of cw pumping the described scaling behavior remains basically the same. Although the phase mismatch in Eq. (4.2) will acquire an extra term of the form  $L(\partial\Delta k/\partial\omega_p)\delta\omega_p$ , the scaling of the SPDC angular and spectral width remains unchanged, making the number of useful entangled pairs again proportional to  $1/L$ . For more sophisticated experiments that require two simultaneously entangled photon pairs there is a catch: as the two pairs should be temporally coherent the increased spectral bandwidth  $\Delta\omega_{\text{SPDC}}$  can only be capitalized on if it remains below than the inverse pulse duration. At fixed detection bandwidth and with the proper angular scaling the SPDC yield and the production rate of double pairs will in fact be independent of the crystal thickness.

## 4.2 Measurements and results

The experimental setup is shown in Figure 4.1. Light from a cw krypton ion laser operating at 407 nm is mildly focused (spot size  $\approx 0.3$  mm) onto a 0.25-mm-thick type-II BBO crystal (cutting angle  $40.9^\circ$ ) which is slightly tilted to generate ‘‘orthogonal crossings’’ (separated by  $2\theta_{\text{off}}$ ). A half-wave plate and two compensating crystals (of 0.13-0.14 mm thickness) compensate for the longitudinal and transverse walk-off of the SPDC light. In the two intersection lines of the emission cones, collimating lenses of  $f = 20$  cm are placed at 20 cm from the generating crystal, directly followed by apertures (diameter up to 5 mm) acting as spatial selectors. This compact setup facilitates the collection of photons in a large space angle. The light emerging from the apertures is focused by  $f = 2.5$  cm lenses onto free-space single photon counters (Perkin Elmer SPCM-AQR-14). Polarizers and interference and/or red filters are used for polarization and spectral bandwidth selection, respectively. Finally, an electronic

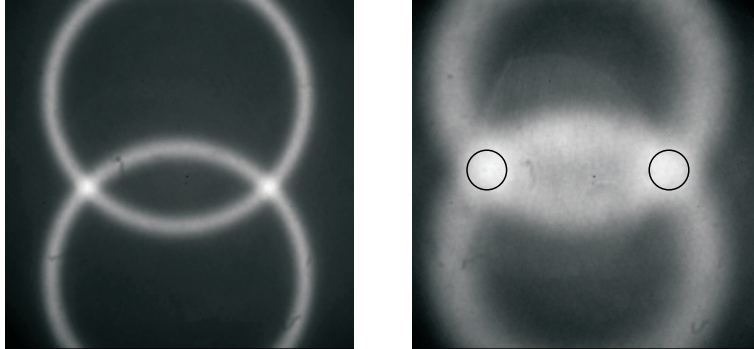
circuit receives the output signals of the photon counters and records the coincidence counts within a time window of 1.76 ns.



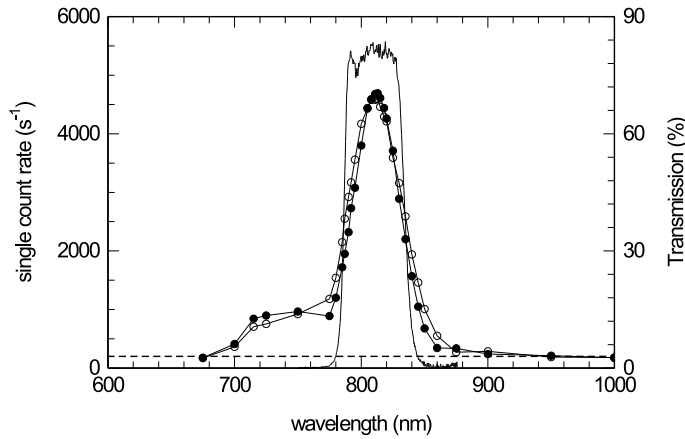
**Figure 4.1:** Schematic view of the experimental setup. A cw krypton ion laser operating at 407 nm pumps a 0.25-mm-thick BBO crystal. The generated photon pairs are collected with  $f = 20$  cm collimating lenses (L1), spatially selected by apertures and focused with  $f = 2.5$  cm lenses (L2) onto single photon counters (SPC). Walk-off effects are compensated for by a half-wave plate (HWP) and two compensating crystals (cc) of 0.13-0.14 mm thickness. Polarizers (P) and interference/red filters (IF/RF) are used for polarization and bandwidth selection, respectively.

Figure 4.2 depicts our key message in the form of two SPDC emission patterns for BBO crystals with thicknesses of  $\approx 1$  mm (measured 0.94 mm) and 0.25 mm. These pictures were measured with an intensified CCD (Princeton Instruments PI-MAX 512HQ) positioned at 6 cm from the BBO crystal behind an interference filter (5 nm spectral width) and two blue-coated mirrors that block the pump beam; no imaging lens was used. The left picture shows that the SPDC rings emitted by the 1-mm-thick BBO are relatively narrow, having a radial width of  $\Delta\theta_{\text{SPDC}} = 10.5 \pm 1.3$  mrad (FWHM). However, this value is somewhat larger than the true width of the rings since broadening by the  $\approx 0.3$ -mm-wide pump spot is still considerable at 6 cm from the BBO. We measured the true radial width of  $\Delta\theta_{\text{SPDC}} = 8.7 \pm 0.7$  mrad for an increased BBO-CCD distance of both 12 and 24 cm. The right picture shows that the 0.25-mm-thick BBO emits much wider rings, with a measured radial width of  $\Delta\theta_{\text{SPDC}} = 30 \pm 2$  mrad (FWHM) (also for 12 cm BBO-CCD distance). Note that the area within the small black circles drawn in this picture is the part of the crossings selected by 5 mm diameter apertures (25 mrad), being about  $(25/30)^2 \approx 70\%$  of the total crossing area. The measured radial widths for both crystals are in good agreement with the expected values and scale well with the crystal thickness. For comparison, we note that the angular distance between the pump and the center of the orthogonal ring crossings is measured to be  $57 \pm 1$  mrad for both crystals, which indeed agrees very well with the theoretical value of  $\theta_{\text{off}}$  (i.e., 57 mrad).

Figure 4.3 shows the spectral distribution of the SPDC light, measured for  $H$ - and  $V$ -polarization in one of the beams (5 mm apertures). After subtraction of the dark counts ( $180 \text{ s}^{-1}$ ) and correction for the spectral efficiency of both grating spectrometer and photon counter [55], we obtained full widths at half maxima of 51 and 44 nm for the  $H$ - and  $V$ -polarized spectrum, respectively. These numbers are in agreement with the expected value of 46 nm, and also the observation that the  $H$ -polarized ( $o$ ) spectrum is somewhat wider than the  $V$ -polarized ( $e$ ) spectrum is as expected [53]. These observed spectral widths scale roughly with those reported in [23], as they are indeed about a factor of 8 larger than the numbers of 4.60 nm and 4.06 nm, which are measured for the two unpolarized SPDC beams emitted by



**Figure 4.2:** SPDC emission patterns observed with an intensified CCD at 6 cm from (left) a 1-mm-thick BBO crystal and (right) a 0.25-mm-thick one (no imaging lens is used). The black circles on the right picture surround the SPDC crossing area selected by 5 mm diameter apertures. Both pictures cover a space angle of  $220 \times 220$  mrad.



**Figure 4.3:** Measured spectral distribution of the down-conversion light for H-(circles) and V-polarization (dots). The dark count level of  $180 \text{ s}^{-1}$  is indicated by the dashed line. After correction for the efficiency of both spectrometer and photon counter, we determined the central peak wavelength to be 815 nm and the peak widths (FWHM) of the H- and V-polarized light to be 51 and 44 nm, respectively. The resolution of the spectrometer is 2 nm. The solid curve (righthand scale) depicts the spectral transmission of a 50 nm broad interference filter that we used.

a 2-mm-thick crystal in [23]. The rather prominent bump between 700 and 780 nm, which is cut off on the low-wavelength side by a red filter (Schott Glass RG715), is probably the first side maximum of the  $\text{sinc}^2$ -function, which is enhanced by the increased spectrometer throughput and detector sensitivity at lower wavelengths [55].

When using detection with free-space (bucket) detectors, there is always a trade-off between photon yield and entanglement quality. The finite size of the detection apertures as

4. Increased polarization-entangled photon flux via thinner crystals

**Table 4.1:** Measured single count rates ( $sc$ ), coincidence count rates ( $cc$ ) and biphoton fringe visibilities  $V_{45^\circ}$  for two aperture diameters and three spectral filters: red filter RF, 50 nm and 10 nm interference filters.

1.4 mm aperture diameter			
filter	sc ( $10^3 \text{ s}^{-1}$ )	cc ( $10^3 \text{ s}^{-1}$ )	$V_{45^\circ}$ (%)
RF	67.0	9.7	98.4
50 nm	44.9	7.8	99.0
10 nm	13.5	2.0	99.5

5 mm aperture diameter			
filter	sc ( $10^3 \text{ s}^{-1}$ )	cc ( $10^3 \text{ s}^{-1}$ )	$V_{45^\circ}$ (%)
RF	847	198	91.1
50 nm	560	145	96.0
10 nm	145	29.6	98.0

compared to the size of the crossing regions can lead to entanglement degradation by spatial labeling, whereas the finite detection bandwidth in relation to the emission bandwidth can lead to degradation by spectral labeling. The choice of our apertures (maximal diameter 5 mm) is motivated by this trade-off. In the absence of compensating crystals the combination of small apertures (diameter 1.4 mm) and narrow filters (spectral width 5 nm) still produced high-quality polarization entanglement: the biphoton fringe visibility [8] observed with the fixed polarizer oriented at  $45^\circ$  was  $V_{45^\circ} = 96\%$ . However, a change to either a larger aperture (5 mm) or a wider filter (50 nm) seriously reduced the entanglement quality, yielding  $V_{45^\circ} = 75\%$  and  $V_{45^\circ} = 41\%$ , respectively, while the combination (5 mm & 50 nm) gave  $V_{45^\circ} = 32\%$ . These numbers clearly show that compensating crystals are also needed if one combines a thin generating crystal with wide apertures or a large detection bandwidth. The so-called “thin-crystal limit” is a relative concept; it only applies when the crystal is thin enough *in relation to a given detection scheme*.

In Table 4.1 we present the count rates and biphoton fringe visibilities  $V_{45^\circ}$ , when using compensating crystals, measured for two aperture sizes and three different filter bandwidths at a pump intensity of 187 mW. The table quantifies the trade-off between photon yield and entanglement quality; higher count rates combine with lower entanglement quality. For all  $2 \times 3$  presented cases the biphoton fringe visibility was measured to be  $> 99\%$  for the  $H$  and  $V$  projection (not in Table), but is generally less for the more critical  $45^\circ$  projection. Although we observe a steady decrease with increasing angular detection width and/or spectral bandwidth,  $V_{45^\circ}$  is at least 96% except for one case. Based on these numbers, we consider the system with 5 mm apertures (25 mrad angular width) and 50 nm filters the most promising. Under these conditions we have measured single and coincidence rates of  $560 \times 10^3 \text{ s}^{-1}$  and  $145 \times 10^3 \text{ s}^{-1}$ , respectively.

To demonstrate the high brightness of our thin crystal source, we compare above rates with those obtained by us with a 1-mm-thick down-conversion crystal using 10 nm interference filters and 4 mm diameter apertures placed at 80 cm from the crystal (5 mrad space angle). For this setting, we measured singles and coincidence rates of  $125 \times 10^3 \text{ s}^{-1}$  and  $33 \times 10^3 \text{ s}^{-1}$ , respectively, at  $V_{45^\circ} = 97.7\%$ . As expected from the scaling laws, the 0.25-mm-thick crystal yields roughly about a factor 4 more photons than a 1-mm-thick one.

To put the yield of our thin SPDC source (with 5 mm apertures and 50 nm filters) in a broader perspective, we compare it with other SPDC sources reported in the literature. The first “high-intensity” source [8] used a 3-mm-thick BBO crystal and detection behind elliptical apertures ( $H \times V$  sizes of  $3 \times 10 \text{ mm}$  at 1.5 m from the crystal). This source produced a coincidence rate of  $10 \text{ s}^{-1} \text{ mW}^{-1}$  ( $1500 \text{ s}^{-1}$  at 150 mW pump power), which is almost  $80 \times$  lower than our obtained coincidence rate of  $775 \text{ s}^{-1} \text{ mW}^{-1}$ . Even an “ultrabright” source [22], based on type-I SPDC and two stacked BBO crystals of 0.59 mm thickness each, which is claimed to be  $10 \times$  brighter than the one reported in [8], is still about  $8 \times$  weaker than our source.

Instead of detecting entangled photons behind apertures, the use of *fiber-coupled* detectors has been introduced to several experimental schemes [23, 56, 57]. The first “high-efficiency” source based on collection with fiber-coupled detectors used a 2 mm BBO crystal to achieve a coincidence rate of as much as  $900 \text{ s}^{-1} \text{ mW}^{-1}$  in the low-pump-power regime and *without polarizers*. The correct comparison is, however, with the system using polarizers for which Fig. 5 in Ref. [23] gives a coincidence rate of  $225 \text{ s}^{-1} \text{ mW}^{-1}$  (obtained by division of the  $90 \times 10^3 \text{ s}^{-1}$  fringe maximum by the 400 mW pump power). Another source [56] used a relatively thin crystal (0.5 mm BBO) to produce entangled photons at  $200 \text{ s}^{-1} \text{ mW}^{-1}$ , while a compact source (2 mm BBO) [57] achieved a similar rate of  $220 \text{ s}^{-1} \text{ mW}^{-1}$ .

To make a fair comparison between our free-space source and these fiber-coupled sources, we have to take into account the fact that fiber-coupled detection enables capturing of a larger area of the ring crossings. Based on our selected space angle and the actual width of the crossings (see Fig. 4.2), we expect a potential increase of our coincidence rate by about a factor 1.5, when switching to fiber-coupled detection. In practice, however, the profit will be only marginal due to the limited in-coupling efficiency in the fibers and the integration over Gaussian mode profiles instead of the sharp-edge profiles of the apertures.

### 4.3 Concluding discussion

In conclusion, we have discussed the scaling behavior of SPDC emission as a function of the thickness  $L$  of the generating crystal. We have found that the photon yield scales as  $1/L$  if the detection angle and bandwidth are matched to the SPDC emission. A quantitative comparison of our source, with a measured coincidence rate of  $775 \text{ s}^{-1} \text{ mW}^{-1}$  at  $V_{45^\circ} = 96\%$ , with existing sources reported in the literature (aperture and fiber-coupled), demonstrates that the use of thinner down-conversion crystals indeed yields considerably higher photon rates than thicker crystals.

How far can we go with the proposed scaling? If the yield continues to scale like  $1/L$  an infinitely thin crystal would give an infinitely strong signal. The ultimate limitation is that the angular widths of the SPDC rings should be smaller than their radii to allow a discussion in

#### 4. Increased polarization-entangled photon flux via thinner crystals

terms of SPDC rings and crossings. Before this limit is reached, there is a practical point of concern: the compensating optics and collimation lenses have to cover the full angular width of the rings, and all this has to be realized within a very limited opening angle (of  $2 \times 57$  mrad). This implies an ultra-compact setup, which is even more complicated by the fact that also the beam dump for the pump laser (not shown in Fig. 4.1) has to be accommodated. In this respect, the studied BBO thickness of 0.25 mm might well be close to the optimum.

## **4.4 Acknowledgements**

We thank Rakesh Partapsing for his experimental contribution. This work has been supported by the Stichting voor Fundamenteel Onderzoek der Materie; partial support is due to the European Union under the IST-ATESIT contract.

## CHAPTER 5

---

### Time-resolved polarization decoherence in metal hole arrays with correlated photons

---

*We study the combined polarization decoherence experienced by entangled photons due to time- and space-related dephasing processes in a metal hole array. These processes are implemented by sending the entangled photons through a birefringent delay and by focusing them on the array. In particular, we demonstrate that compensating the temporal separation of the two polarizations after passage through the array can only partly recover the original coherence. This shows, surprisingly, a coupling between the temporal and spatial decoherence channels; we ascribe this coupling to transverse propagation of surface plasmons.*

*P.S.K. Lee, M.P. van Exter, and J.P. Woerdman, J. Opt. Soc. Am. B **23**, 134-138 (2006).*

## 5.1 Introduction

The use of entangled photon pairs has proved to be a powerful tool for several forms of information processing like quantum cryptography [15, 58], but also for precise optical measurements in the field of quantum metrology [59, 60]. The benefits of these techniques over their classical counterparts is based on the exploitation of the robust correlations, which are often well-known, between the photons [59]. In this chapter, we report on the use of entangled photons for measurements on surface plasmons in metal hole arrays [61].

Metal hole arrays (metal films perforated with a periodic array of subwavelength holes) can exhibit extraordinary transmission of light with a certain resonant wavelength [61]. This transmission is surface-plasmon mediated: freely propagating light incident on one side of the metal film resonantly excites surface plasmons (SP's), which subsequently couple through the hole pattern to SP's at the other side and finally reradiate into photons [62–64]. Since its original demonstration [61], this phenomenon has been studied in different contexts [65–67], including the survival of quantum entanglement in the mentioned conversion process [67].

The polarization properties of the extraordinary light transmission in metal hole arrays have been a special topic of study in several papers [68–70]. Polarization- and angle-resolved measurements in [68] have shown that propagating SP's can act as polarization selectors, i.e., only transmission of the polarization component aligned with this direction occurs. This strong relation between SP propagation and the polarization properties of the extraordinary transmission is also demonstrated in a study of the polarization decoherence as a function of the numerical aperture of the light beam that is focused on the array [69]. This polarization decoherence, which also depends on the incident state of polarization, is ascribed to the propagation of SP's in combination with the non-plane wave character of the incident beam. The study of surface plasmon propagation via polarization properties requires an analysis [71] that is most clearly described in terms of 4 Stokes parameters and a  $4 \times 4$  Mueller matrix, representing a black-box description of the complicated physical system.

In this chapter, we will go beyond the space-resolved polarization decoherence studied in [69]. More specifically, we additionally impose a time delay between the  $H$ - and  $V$ -polarization components [72] before focusing on the hole array. As we measure the polarization correlations in the  $45^\circ$ -basis, this temporal distinction leads to a lower polarization fringe visibility, and thus to an *additional* polarization decoherence channel in time (on top of the decoherence in space induced by SP propagation and focused illumination). Our key question in this respect is whether both decoherence channels are independent from each other, i.e., whether in the presence of focused illumination the decoherence due to the time delay can be fully compensated for by retiming the  $H$ - and  $V$ -component behind the hole array.

Within the context of the Mueller-matrix black-box method the answer should be positive, i.e., operations in time and space should be independent from each other and can thus be interchanged at will. However, optical decoherence is different from most other forms of decoherence in the sense that the polarization information is not lost to some abstract (infinitely large) environment, but is instead spread over the time and space coordinates within the optical beam; the unpolarized component appears only after temporal and/or spatial averaging over the full beam. As the “labeling” information remains available within the propagating beam, it can be extracted and used in a later stage. As a result, consecutive decoherence chan-

nels are *not* necessarily *independent* and the corresponding ( $4 \times 4$ ) matrices generally *can not be multiplied* in a simple way. We will show experimentally that the decoherence channels are indeed coupled in our black box as they are mixed by propagating surface plasmons.

As a final remark, our discussion of the observed decoherence in metal hole arrays is qualitative in nature. The reason for this is that a sufficiently complete and simple theory of light transmission through hole arrays does not exist yet. Several (independent) numerical models that would allow a more quantitative analysis are around [62, 64, 70], but using these would lead to model-dependent results. Instead we have chosen to focus on the generic features.

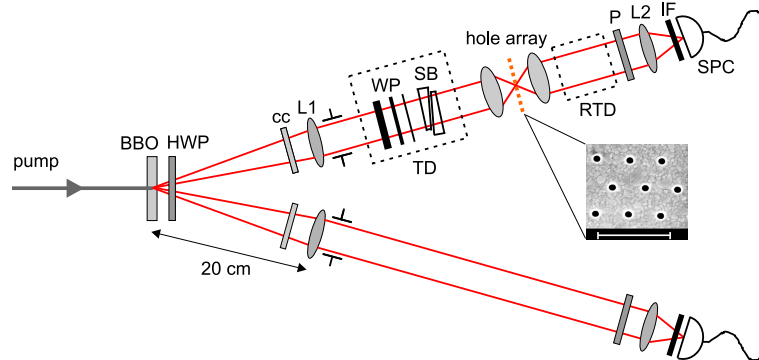
## 5.2 Experimental methods

Figure 5.1 shows the experimental setup that provides for the generation of polarization-entangled photon pairs via the process of spontaneous parametric down-conversion (SPDC) [8]. The figure caption describes in detail how our SPDC source generates a polarization-entangled signal and idler beam, and how the time and space information in one of the beams can be modified by a polarization-dependent (=birefringent) delay and focusing onto a metal hole array. In order to have sufficient time resolution in the experiment, it is essential that the spectral bandwidth of the entangled photons is larger than the spectral width of the transmission resonance of the hole array. We have chosen a relatively thin crystal (0.25 mm) in order to generate entangled photons over a large spectral bandwidth; with the properly scaled geometry such a thin crystal can generate even more entangled photons than a thicker crystal [24].

We use a metal hole array in which the holes are arranged in a hexagonal lattice. The hole diameter is 200 nm and the lattice constant is 886 nm. The holes have been etched with a focused ion beam into a 200-nm-thick film of gold, that is bonded to a glass substrate with a 2-nm-thick titanium layer. The hole array is positioned in the focus between two lenses that form a 1:1 telescope. In the experiment we only use different sets of these lenses behind the apertures to vary the numerical aperture of the light incident on the array. Thereby, the aperture diameter is fixed at 5 mm, giving a detection angle of 25 mrad which is smaller than the SPDC ring crossings (30 mrad) [24].

A typical transmission spectrum of the hole array at plane-wave illumination is shown in Fig. 5.2. Essential is the very sharp resonance peak of the hole array: its FWHM of only 18 nm is much smaller than the 50 nm spectral width of the interference filter (also shown), which in turn is somewhat smaller than the FWHM of the SPDC light [24]. Please note that in the literature FWHM values of at least 50 nm are reported for (1,1) SP resonances in square arrays [61, 67]. We think that the resonance in our sample is so sharp because we use a hexagonal instead of a square array: the reciprocal lattice of the hexagonal array is rotated with respect to its direct lattice which leads to less SP scattering at the holes. Furthermore, our sharp resonance is carried by the SP mode at the air-metal interface, which experiences less damping than that at the glass-metal interface.

To create a time delay  $\tau$  between two orthogonal polarization components of the SPDC light, a set of quartz waveplates and a Soleil-Babinet compensator are placed in the beam. The waveplates are oriented in the directions of the BBO axes and have thicknesses that differ by



**Figure 5.1:** Schematic view of the experimental setup. Light from a cw krypton ion laser operating at 407 nm is mildly focused (spot size  $\approx 0.3$  mm) on a 0.25-mm-thick BBO crystal. Walk-off effects are compensated for by a half-wave plate (HWP) and two compensating BBO crystals (cc) of 0.13-0.14 mm thickness. The entangled photons pass  $f = 20$  cm collimating lenses L1 and 5-mm-diameter apertures before quartz waveplates (WP) and a Soleil-Babinet compensator (SB) create a time delay (TD) between orthogonal polarization components in the upper beam. In this beam, the light propagates through a metal hole array positioned in the focus of the telescope. The inset shows a SEM picture of our hexagonal hole array (scale bar corresponds to 2  $\mu\text{m}$ ). A reverse time delay (RTD), similar to TD, is applied in some of the experiments. Both polarizers P are fixed at  $45^\circ$  with respect to the BBO axes, and via interference filters (50 nm FWHM) the two beams are focused onto single photon counters SPC (Perkin Elmer SPCM-AQR-14) by  $f = 2.5$  cm lenses (L2). Finally, the output signals of these counters are sent to an electronic circuit which records coincidence counts within a time window of 1.76 ns.

factors of 2 and range from 0.31 to 4.94 mm ( $\approx 2^4 \times 0.31$  mm), corresponding to a time delay  $\tau$  range from about 9 to 145 fs. Using polarization interferometry, we have measured the exact thicknesses of the waveplates; these agree very well with the specified values (error in  $\tau < 0.1$  fs).

The polarization decoherence induced by a temporal separation of the  $H$ - and  $V$ -component can be characterized by the fringe visibility of the coincidence rate scanned as a function of the time delay  $\tau$ . In a typical measurement, we determine the envelope of this fringe pattern which is defined by minimal and maximal coincidence counts. These minima and maxima are measured when we fine-tune  $\tau$  via the Soleil-Babinet compensator ( $2\lambda$  range) such that the optical path difference between the  $H$ - and  $V$ -component is precisely  $N\lambda$  and  $(N + 1/2)\lambda$ , respectively, since our compensated SPDC source is set to the singlet two-photon state  $(|HV\rangle - |VH\rangle)/\sqrt{2}$ . Here,  $\lambda$  is the degenerate wavelength of the SPDC light, being  $2 \times 407 = 814$  nm. We measure with the fast axes of the waveplates both in horizontal (negative  $\tau$ ) and vertical (positive  $\tau$ ) direction. From the measured coincidence counts  $R_m$  at path difference  $m\lambda$  we calculate the polarization fringe visibilities  $V$  via  $(R_{N+1/2} - R_N)/(R_{N+1/2} + R_N)$ . We note that *negative* time-resolved visibilities can be obtained (see Fig. 5.3), as sidelobes of a sinc-profile, due to the rectangular shape of the spectrum of the interference filter (see Fig. 5.2). Whenever possible, we scanned the Soleil-

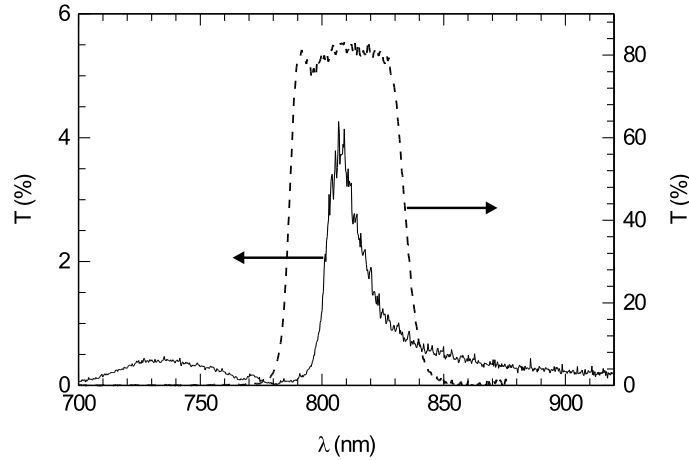


**Figure 5.2:** Transmission spectra of the hexagonal array (solid, left axis) and 50 nm FWHM interference filter (dashed, right axis).

Babinet compensator over more than  $\lambda/2$  to find the exact minima and maxima. The error in the measured visibilities  $V$  is typically 0.01 and is caused by quantum fluctuations in  $R_N$  and  $R_{N+1/2}$ .

### 5.3 Experimental results

Figure 5.3 depicts the time-resolved visibility measurements, performed with the time delay in front of the telescope (see Fig. 5.1). We first concentrate on the solid curve in Fig. 5.3 which shows the measurement *without* hole array. This curve has a peak visibility of  $V = 0.96 \pm 0.01$ , which quantifies the entanglement quality produced with our SPDC source [24]. The high visibility shows that complications due to entanglement in transverse momentum are avoided as the apertures used in the experiments are smaller than the size of the SPDC ring crossings. The visibility decays sharply with the time delay  $\tau$ ; the small width of  $65 \pm 2$  fs (peak-to-zero) is associated with the large spectral width of the SPDC light generated by our 0.25-mm-thick crystal [24]. This decay is still limited by the 50 nm FWHM interference filters since the same measurement, performed without filters, yields a more narrow curve with a somewhat lower peak visibility and no sidelobes. The width of this triangular-shaped curve is only  $50 \pm 2$  fs which agrees well with the theoretically expected dispersion of 200 fs per mm of BBO at a wavelength of 814 nm. In comparison, a (peak-to-zero) width of about 150 fs has been reported for a source using a 1-mm-thick BBO crystal [73]. The sidelobes in the measured curve result from the sharp edges in the ‘top hat’ transmission spectrum of the interference filter (see Fig. 5.2).

Next we positioned the hole array in the centre of the telescope (see Fig. 5.1). The three marked curves in Fig. 5.3 show time-resolved visibility measurements *with* hole array for three different numerical apertures (NA) of the light incident on the hole array. First, we see that the peak visibility  $V$  drops from  $V = 0.93 \pm 0.01$  (NA=0.017), via  $V = 0.83 \pm 0.01$

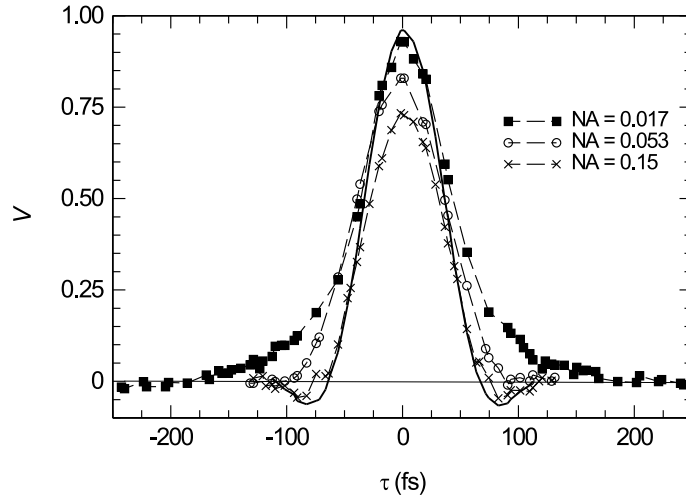


**Figure 5.3:** Time-resolved polarization decoherence, measured as the polarization fringe visibility  $V$  versus time delay  $\tau$ , for a hole array positioned in the focus of a telescope of variable numerical aperture  $NA$ . The solid curve without markers shows the measurement without hole array as a reference. The horizontal line depicts the zero level.

( $NA=0.053$ ) to  $V = 0.73 \pm 0.01$  ( $NA=0.15$ ). We ascribe this reduction to polarization decoherence in the spatial domain due to the polarization-dependent propagation of surface plasmons out of the limited region excited with a focused optical beam [69, 74]. Equivalently, this reduction can be ascribed to the combined polarization- and angle-dependence of the optical transmission [68]. The fact that we observe lower visibilities with increasing time delay  $\tau$  shows the additional polarization decoherence in the time domain. The decrease is sharpest for the case of strongest focusing ( $NA=0.15$ ), where we obtain a peak-to-zero width of  $76 \pm 2$  fs. For the cases  $NA=0.053$  and  $NA=0.017$ , the low-visibility values decay much more gradual and the approximate zeros are less accurate. Therefore, we instead determine the peak-to-2% width as  $88 \pm 2$  fs and  $160 \pm 8$  fs, respectively, for these cases.

In Fig. 5.4 the averaged absolute values of  $V(-\tau)$  and  $V(+\tau)$  in Fig. 5.3 are plotted on a logarithmic vertical scale as a function of  $|\tau|$ . The decay of the  $NA=0.017$  curve is described very well by a simple exponential  $a \exp\{-\tau/\tau_c\}$  with a decay time of  $\tau_c=38 \pm 1$  fs. For this case of weak focusing the measured decay time is just the field decay time of the surface plasmons. At a propagation speed of  $\approx 0.95c$ , the intensity decay time of 19 fs corresponds to a propagation length of about  $5.4 \mu\text{m}$ , being much smaller than the size of the spot of excitation.

Theoretically, we expect a Fourier relation between the time-resolved visibility of Fig. 5.4 and the transmission spectrum of the hole array. The described exponential decay in time corresponds to a Lorentzian-shaped transmission spectrum with a FWHM of  $1/\pi\tau_c$ . The calculated value of 18.5 nm is indeed close to the FWHM of the 18 nm obtained from the transmission spectrum in Fig. 5.2. Because of the asymmetric Fano profile of the resonance (see Fig. 5.2), a more realistic model is obtained by inclusion of a  $\delta(t)$ -response in time

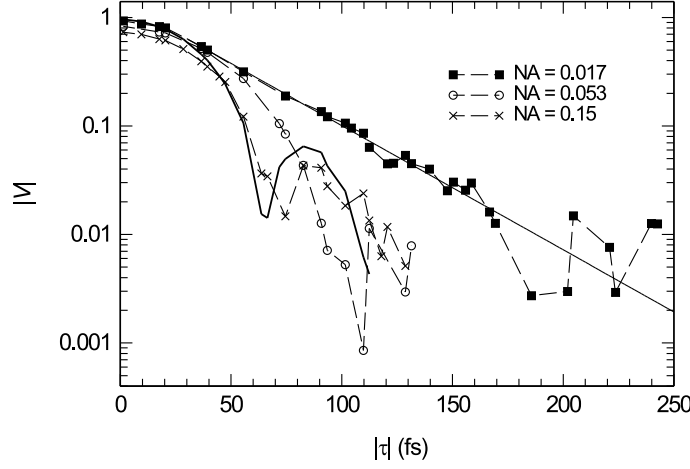


**Figure 5.4:** The averaged absolute values of  $V(-\tau)$  and  $V(+\tau)$  in Fig. 3, plotted on a vertical logarithmic scale as a function of  $|\tau|$ . The thicker curve without markers represents the measurement without hole array. The straight solid line is a fit of the exponentially decaying part of the  $NA=0.017$  curve, from which a decay time  $\tau_c=38\pm 1$  fs is obtained.

(uniform background in frequency) which results in a slightly ( $\approx 10\text{-}20\%$ ) wider spectrum for the same decay rate.

The faster decay of the time-resolved visibility at larger numerical apertures, as shown in Fig. 5.3 and 5.4, is a result of transit time effects: for large NA surface plasmons move out of the excitation area more rapidly. Alternatively, we can interpret it in terms of a Fourier relation: the transmission spectrum becomes broader under strong focusing conditions due to angle-dependent spectral shifts [68].

As our final and most crucial experiment, we studied the recovery of the polarization coherence by compensation of the imposed time delay by an additional delay behind the array. More specifically, we have measured the time-resolved visibility with a *fixed* time delay of  $\tau_{\text{fix}} = 145$  fs in front of telescope ( $NA=0.053$ ) and array (this  $\tau_{\text{fix}}$  is large enough to completely remove the polarization entanglement) and a variable “reverse” time delay  $-\tau_{\text{fix}} + \tau$  behind the hole array. Fig. 5.5 shows the measured visibility as a function of  $\tau$  (solid dots) as well as the measurement without reverse time delay (open circles for  $\tau_{\text{fix}}=0$  copied from Fig. 5.3). We note that both curves in Fig. 5.5 have practically the same functional shape, as the focusing conditions are equal. For the peak visibility, however, we obtain a value of  $V = 0.75 \pm 0.01$  for the reverse time delay measurement, whereas a value of  $V = 0.83 \pm 0.01$  was found in the original measurement. In other words, the polarization decoherence induced by  $\tau_{\text{fix}}$  (to  $V \approx 0$ ) cannot be totally compensated for by a reverse time delay  $-\tau_{\text{fix}}$ . The permanent loss of polarization coherence shows that both decoherence channels are not independent, but coupled in our black box. We note that, *in absence* of the hole array, a peak visibility of 0.96 was measured (being a measure of the entanglement quality of our SPDC source [24]), thereby excluding the combination of delay/reverse delay in itself as a potential source of

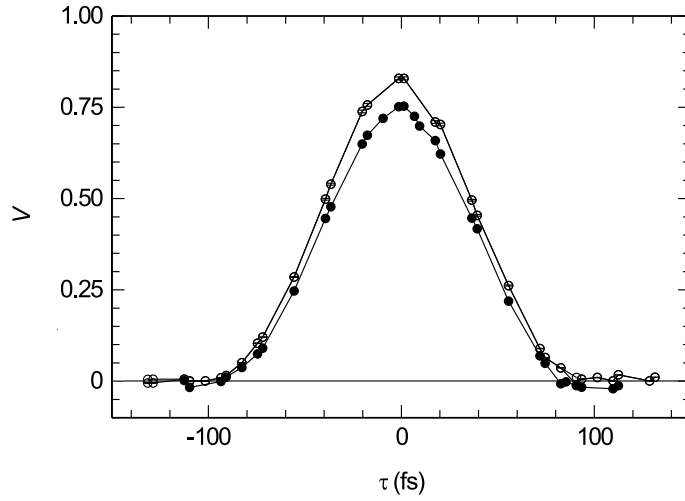


**Figure 5.5:** Time-resolved polarization decoherence at  $NA=0.053$  with variable reverse time delay  $-\tau_{\text{fix}} + \tau$  behind the telescope and fixed time delay  $\tau_{\text{fix}}=145$  fs in front of telescope (solid dots). The measured polarization fringe visibilities  $V$  are plotted as a function of  $\tau$ . The  $NA=0.053$  curve in Fig. 3 is also plotted for comparison (open circles). The horizontal line depicts the zero level. The vertical error bars are smaller than the size of the data symbols.

coherence loss.

Theoretically, the peak visibility for the reverse time delay measurement (for large  $\tau_{\text{fix}}$ ) can be interpreted as the average of the visibilities measured without any time delay in the  $45^\circ$ - and the  $\sigma^+$ -basis. This is indeed the case, as we measured  $V_{45^\circ} = 0.83 \pm 0.01$  and  $V_{\sigma^+} = 0.68 \pm 0.01$  (see also [69]) which average to  $V = 0.75 \pm 0.01$ . The reason for the mentioned averaging is most easily understood in the frequency domain: within the bandwidth of our SPDC light the polarization incident on the telescope is different for every frequency  $\omega$  (due to a varying phase delay  $\omega\tau_{\text{fix}}$ ), i.e., it changes from  $+45^\circ$ , via  $\sigma^+$ ,  $-45^\circ$  and  $\sigma^-$ , to  $+45^\circ$  again.

To confirm that the propagation of surface plasmons plays a key role in the coupling between the decoherence channels, we repeated the delay/reverse delay measurement for  $\tau=0$  at low  $NA=0.017$ . We now measured a visibility of 0.90, which is much closer to its original peak value of 0.93 (see Fig. 5.3) than for the  $NA=0.053$  data. This stronger recovery of polarization coherence is ascribed to the slower propagation of the surface plasmons out of the larger excitation spot (see Fig. 5.4).

Finally, we note that our metal hole array is not as polarization-isotropic as we would like, as production errors lead to some birefringence and dichroism of the array [69]. To study the potential effects of these anisotropies on the (recovery of) polarization coherence, we fix the input polarization of the upper beam in Fig. 5.1, by orienting the polarizer of the lower beam horizontally, and used extra polarization optics to measure the Mueller matrix of the array as in [69]. The measured Mueller matrix shows a comparable structure as in [69], i.e., dominant (at least 0.90) diagonal elements and finite but small ( $\leq 0.10$ ) off-diagonal elements, which

quantify the slight array imperfections. By choosing convenient experimental conditions in the decoherence experiments of Figs. 5.3- 5.5, we could remove most of the effects created by the off-diagonal elements. If the fringe visibilities in Figs. 5.3- 5.5 would for instance be measured by just rotating the polarizer behind the array we would face variations up to  $\approx 20\%$  in the single count rate. By keeping the polarization fixed and instead varying the birefringent delay we did not have this problem. Furthermore, as the off-diagonal elements hardly depend on the used NA [69], the drop in the measured peak visibilities  $V \approx M_{22}(1 - M_{20}) + M_{02}$  in Fig. 5.3 must indeed correspond to a decrease of the diagonal element  $M_{22}$ , and thus to polarization decoherence and not to a mere change in the state of polarization. The above arguments show that the slight polarization-anisotropic nature of our hole array hardly affects the measured visibilities and polarization decoherence.

## 5.4 Concluding discussions

In conclusion, we have performed time-resolved measurements of the polarization decoherence in a metal hole array under different focusing conditions. Apart from the decoherence induced by focused illumination of the hole array, we have shown that a temporal separation of the incident orthogonal polarization components creates an additional decoherence that cannot be totally compensated for by retiming of the polarization components after propagation through the array. This result demonstrates that the time- and space-related decoherence channels (operating on frequencies and angles, respectively) are coupled via propagating surface plasmons in a metal hole array.

An important result is that the Mueller-matrix black-box method, although convenient, should be treated with care in optical decoherence; as we have observed, it can even produce incorrect results in the analysis of a series of consecutive decoherence processes. For a complete description of the polarization evolution, beyond the simple truncated form provided by the Mueller algebra, two options are available. One option is to retain the full temporal and spatial information of the polarization. The observed coupling between the time- and space-related decoherence channels can then be mathematically explained by the non-commuting behavior of the angle-dependent transmission matrix  $\mathbf{t}(\boldsymbol{\theta}, \lambda)$  of the hole array [ $\boldsymbol{\theta}=(\theta_x, \theta_y)$ ] and the time-dependent Jones matrix  $\mathbf{t}(\tau)$ , associated with the birefringent time delay. As  $\mathbf{t}(\boldsymbol{\theta}, \lambda)$  is a non-diagonal matrix whereas  $\mathbf{t}(\tau)$  is diagonal in the  $(H, V)$ -basis (axes orientation of BBO and waveplates), it is the matrix character and not the  $\lambda$ -dependence of  $\mathbf{t}(\boldsymbol{\theta}, \lambda)$  that frustrates the commutation. Another option is to divide the spatial/angular information over  $N$  discrete transverse modes. However, in this multimode description the classical evolution of our black box already requires a  $2N \times 2N$  matrix [75] for monochromatic incident light only. If we also include the frequency, i.e., temporal information, an even larger matrix is needed which may lead to a less transparent description.

## 5.5 Acknowledgments

We thank P.G. Kwiat for his stimulating discussions and original ideas. We also thank Y.C. Oei for his experimental contribution, P.F.A. Alkemade (Delft University of Technology)

5. Time-resolved polarization decoherence in metal hole arrays with correlated photons

for production of the hole arrays and E. Altewischer for lending them to us and providing essential data. This work has been supported by the Stichting voor Fundamenteel Onderzoek der Materie; partial support is from the European Union under the IST-ATESIT contract.

## CHAPTER 6

---

### How focused pumping affects type-II spontaneous parametric down-conversion

---

*We demonstrate that the transition from plane-wave to focused pumping in type-II down-conversion is analogous to the transition from cw to pulsed pumping. We show experimentally that focused pumping leads to asymmetric broadening of both the ordinary and extraordinary light distribution. It hardly affects the entanglement quality if proper spatial filtering is applied.*

*P.S.K. Lee, M.P. van Exter, and J.P. Woerdman, Phys. Rev. A **72**, 033803 (2005).*

## 6.1 Introduction

Spontaneous parametric down-conversion (SPDC) has become the common method to generate entangled photon pairs for experimental studies on fundamental features of quantum mechanics [6–8]. Though these photon pairs can be simultaneously entangled in energy, momentum and polarization (for type-II SPDC), the use of polarization entanglement is most popular due to its simplicity. The general theoretical aspects of two-photon entanglement in type-II SPDC are well known and thoroughly studied in [20, 32]. More specifically, also the effect of the *spectral* properties of the pump on the down-converted light has been the topic of investigation in several papers, including the effect of the spectral pump width on the spatial coherence of the down-converted beams [76] and the spectral consequences of broadband pulsed [77, 78] pumping in type-II SPDC.

The role of the *spatial* properties of the pump in type-II SPDC, and particularly that of focused pumping [30, 31], is a less explored regime, though. Proper focusing of the pump laser is certainly necessary when the entangled photon pairs are detected with fiber-coupled photon counters [23, 56]. In order to optimize the collection of entangled photon pairs, both the size of the backward-propagated fiber mode and the transverse beam walk-off in the crystal have to match the size of the pump spot [23]. A potentially beneficial effect of focused pumping may also arise when using “bucket” detectors behind apertures for pair detection. A simple argument that suggests such effect is that the large wavevector spread associated with focused pumping will generally broaden the two rings that comprise the usual SPDC pattern. The increased area of the ring crossings might thus allow us to work with larger apertures and enhance the yield of polarization-entangled photon pairs. To investigate the feasibility of this scheme and check for any side effects in both the bucket and fiber-coupled detection scheme, a better understanding of the role of focused pumping in SPDC is needed.

In this chapter, we study the effect of focused pumping on the single-photon image generated via type-II SPDC, contrary to papers that specifically treat the effect on coincidence imaging [30, 31]. In particular, we theoretically and experimentally demonstrate that the transition from plane-wave to focused pumping leads to the same *asymmetric* broadening of both down-converted rings. Our theoretical description follows the approach that Grice and Walmsley [78] use to analyze the difference between the ordinary and extra-ordinary spectrum in the transition from cw pumping to broadband (pulsed) pumping, which could be loosely called “the effects of focusing in time” (instead of space). We also study the consequences of focused pumping for the measured photon yield and entanglement quality of the polarization-entangled photon pairs. We present the experimental data that support these consequences for bucket detection only and include the case of fiber-coupled detection in an outlook discussion.

## 6.2 Theory

In this section we present an analysis of the spatial properties of photons generated via type-II SPDC under focused pumping. Grice and Walmsley [78] have analyzed the spectral properties of the generated ordinary (*o*) and extra-ordinary (*e*) photons at fixed transverse momentum  $\mathbf{q}_o = \mathbf{q}_e = \mathbf{0}$  and plane-wave pumping by expressing the spectral SPDC profile as

a frequency integral of the pump envelope function and phase matching function. We perform a similar integration in space to analyze the complementary problem, i.e., calculating the SPDC emission profile for cw pumping at fixed frequency ( $\omega_o \approx \omega_e \approx \omega_p/2 \equiv \Omega$ ). The angular emission profile for this case is then represented by the differential single-photon count rate (per angular and frequency bandwidth) which, for the  $o$ -polarized emission, can be expressed as

$$\frac{dR_o}{d\theta_o d\omega_o} \propto \int d\theta_e I(\theta_p) \text{sinc}^2[\phi(\theta_e, \theta_o)], \quad (6.1)$$

where  $I(\theta_p) = \int d\omega_p |E_p(\theta_p; \omega_p)|^2$  is the pump envelope function, expressed in the pump angle  $\theta_p \approx (c/\omega_p)\mathbf{q}_p$ . Conservation of each component of the pump transverse momentum  $\mathbf{q}_p$  requires  $\mathbf{q}_p = \mathbf{q}_o + \mathbf{q}_e$  or, equivalently,  $2\theta_p = \theta_o + \theta_e$ . The phase mismatch  $\phi = \Delta k_z L/2$  built up during propagation over half the crystal length  $L$  is incorporated in the function  $\text{sinc}(x) \equiv \sin(x)/x$ . The emission profile for the  $e$ -polarized photons is obtained by swapping the  $o$ - and  $e$ -indices in Eq. (6.1).

The solution of the angular integral Eq.(6.1) is more difficult than that of the frequency integral encountered in Ref. [78]. The reason is not so much the increase from 1 to 2 dimensions, but rather the more complicated structure of the phase-mismatch function  $\phi$ , which is at least quadratic in the transverse momenta. To keep the expressions manageable we will only consider the case of mild focusing, where the angular profile of the pump is much smaller than the angular radii of the generated SPDC rings. Whenever possible we will also neglect the small differences between the various refractive indices (denoted by a single parameter  $n$ ) and take the internal walk-off angle of the  $e$ -polarized pump and SPDC light identical as  $\rho = (2/n)\theta_{\text{off}}$ . Under these conditions, the phase mismatch becomes [35, 79]

$$\phi(\theta_p, \theta_o, \theta_e) \approx \left( \frac{L\Omega}{2c} \right) \left( -C + \rho (2\theta_{p,y} - \theta_{e,y}) + \frac{1}{2n} (\theta_{o,x}^2 + \theta_{o,y}^2 + \theta_{e,x}^2 + \theta_{e,y}^2) \right), \quad (6.2)$$

where  $C$  is a constant that depends on material properties and cutting angle, where all external angles  $|\theta_i| \ll 1$  are measured with respect to the ( $z$ -directed) surface normal, and where the  $c$ -axis of the uniaxial crystal lies in the  $yz$ -plane. Eq. (6.2) highlights the phase-matching physics: the two linear terms arise from the angle dependence of the extra-ordinary refractive index (for both pump and  $e$ -ray), while the second-order terms arise from the reduction in  $k_z$  at non-normal incidence (second-order terms in  $\theta_p$  are neglected). The angular shape of the  $o$ -polarized emission is found by removing  $\theta_e \equiv (\theta_{e,x}, \theta_{e,y})$  from Eq. (6.2) which gives

$$\phi(\theta_p, \theta_o) = \left( \frac{L\Omega}{2nc} \right) \left( |\theta_o + \theta_{\text{off}}\mathbf{e}_y - \theta_p|^2 - \left( \theta_{\text{off}}\sqrt{2} - \theta_{p,y}/\sqrt{2} \right)^2 \right), \quad (6.3)$$

for  $C = \theta_{\text{off}}^2/n$  and vice versa for the  $e$ -profile.

For plane-wave pumping, the emission profiles are completely determined by the phase-matching condition  $\phi \approx 0$ . The two polarized components are emitted in angular cones (= rings in the far-field) that are approximate mirror images of each-other and are vertically displaced with respect to the pump over angles  $-\theta_{\text{off}}$  and  $\theta_{\text{off}}$ , for the  $o$ - and  $e$ - rays, respectively [32]. From Eq. (6.3) we can see that, for the chosen constant  $C$ , these rings have radii

$\theta_r = \theta_{\text{off}}\sqrt{2}$  and cross each other at  $90^\circ$  if the pump enters at normal incidence ( $\theta_p = \mathbf{0}$ ). For plane-wave pumping at non-normal incidence, angle tuning in the  $x$ -direction will produce a simple  $x$ -shift of the SPDC pattern, whereas angle tuning in the  $y$ -direction produces a  $y$ -shift as well as a change in the ring radii [see Eq. (6.3) and Fig. 6.1]. By combining these effects in the integration over the angular pump profile we can explain the asymmetric angular smearing observed under focused pumping.

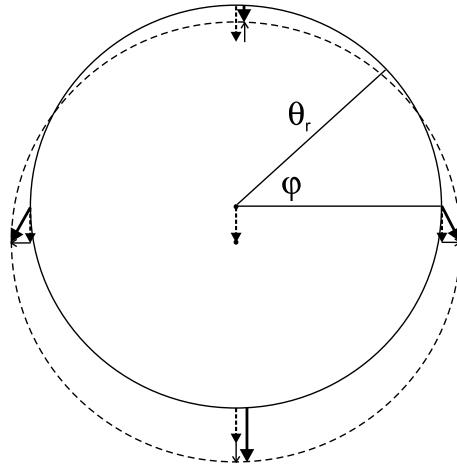


**Figure 6.1:** The two-fold effect of a change in the  $y$ -component of the pump wavevector  $\theta_p$  on the SPDC ring: the center of the ring is shifted by  $\theta_{p,y}$  (dotted arrow) while the radius of the ring increases by  $\theta_{p,y}/\sqrt{2}$  (thin arrow). As the vector addition (thick arrow) of both effects depends on the angular position  $\varphi$  within the ring, the angular broadening due to focused pumping is non-uniform over the SPDC rings.

For the visual picture of the asymmetric broadening, we introduce (shifted) radial coordinates  $\theta_r + \delta\theta_r$  and  $\varphi$  (see Fig. 6.1), which are defined by  $\theta_x = (\theta_r + \delta\theta_r)\cos\varphi$  and  $\theta_y = (\theta_r + \delta\theta_r)\sin\varphi \pm \theta_{\text{off}}$  (plus and minus sign apply to the  $e$ - and  $o$ -ring, respectively). By implementing these radial coordinates in Eq. (6.3) we can write Eq. (6.1) as

$$\frac{dR_o}{d\theta_o d\omega_o} \propto \int d\theta_p \exp(-2|\theta_p|^2/\sigma^2) \text{sinc}^2 \{ \pi[\delta\theta_r - \mathbf{a}(\varphi) \cdot \theta_p]/\bar{\theta} \}, \quad (6.4)$$

where  $\bar{\theta} = \pi nc/(L\Omega\theta_r)$  is the radial width of the SPDC ring for plane-wave pumping and  $I(\theta_p) = \exp(-2|\theta_p|^2/\sigma^2)$  is the Gaussian pump envelope function with pump divergence  $\sigma$ . This expression determines the asymmetric ring smearing under focused pumping via the vector  $\mathbf{a}(\varphi) = (\cos\varphi, 1/\sqrt{2} - \sin\varphi)$ , which quantifies the ‘‘local changes in ring radius’’ induced by the spread in  $\theta_p$ . For a more direct insight in the ring smearing, it is useful to decompose the pump angle  $\theta_p$  into components perpendicular ( $\theta_{p\perp}$ ) and parallel ( $\theta_{p\parallel}$ ) to  $\mathbf{a}(\varphi)$ . As only the component  $\theta_{p\parallel}$  contributes to the phase mismatch, we can easily remove the Gaussian integral over  $\theta_{p\perp}$  and reduce Eq. (6.4) into an one-dimensional integral. The only relevant parameter in this integral is the dimensionless ratio  $x(\varphi)$  between the projected pump divergence (FWHM  $1.18\sigma \cdot |\mathbf{a}(\varphi)|$ ) and the ring width under planar pumping (FWHM  $0.89\bar{\theta}$ ). Instead of expressing this integral in terms of error functions, we have followed a

numerical approach to solve this one-dimensional integral. As a good approximation we find that the relative increase in the (FWHM) ring width due to focused pumping depends on the angular position in the ring as

$$y(\varphi) = \sqrt{1 + x(\varphi)^2} . \quad (6.5)$$

We note that Eq. (6.5) is a very good approximation; even the largest deviations (around  $x = 1$ ) between (FWHM) widths obtained from the numerically solved integral [Eq. (6.4)] and the approximation [Eq. (6.5)] are at most 5%. The asymmetric ring smearing is now directly quantified by Eq. (6.5) via the angle-dependent value  $|\mathbf{a}|$ . The top of the  $o$ -polarized ring ( $\varphi = \pi/2$ ) remains narrow as  $|\mathbf{a}| = 1 - 1/\sqrt{2} \approx 0.29$  is small; at the bottom ( $\varphi = -\pi/2$ ) the smearing is much larger as  $|\mathbf{a}| = 1 + 1/\sqrt{2} \approx 1.71$  is large; in between at  $\varphi = 0$  the smearing is proportional to  $|\mathbf{a}| = \sqrt{1.5} \approx 1.22$ . The simple Eq. (6.5) allows us to predict the ring width at a certain part of the ring, once we know the pump divergence  $\sigma$  and the ring width at plane-wave pumping.

If we repeat the above exercise for the  $e$ -polarized ring we find that the phase mismatch obeys the same Eq. (6.4) in the shifted radial coordinates of this ring. The  $e$ -polarized SPDC ring will therefore be simply a displaced version of the  $o$ -polarized ring, with identical shape and an “asymmetric smearing” in exactly the same orientation (narrow top, wide bottom).

The effect of focused pumping on coincidence imaging [30, 31] can be calculated by performing a similar analysis as presented above. Instead of integrating over all angles  $\theta_e$  in Eq. (6.1), we can now fix  $\theta_e$  and simply calculate the integrand to obtain the coincidence image for the  $o$ -polarization, and do the opposite for the  $e$ -polarization. In the “thin-crystal limit”, which is commonly applied [30, 31], the phase mismatch is small at  $\phi \approx 0$  and the coincidence image is just (a scaled version of) the pump profile  $I(\theta_p)$ . Going beyond this limit, the phase mismatch function will then also lead to asymmetric coincidence images for both polarizations. These coincidence images are only slices of the Gaussian pump profile, with a width and orientation that depend on the polarization and the angular position in the SPDC ring.

### 6.3 Measurements and results

The experimental setup is shown in Fig. 6.2. Light from a krypton ion laser operating at 407 nm is focused onto a 1-mm-thick type-II BBO crystal (cutting angle  $41.2^\circ$ ) which was slightly tilted to generate orthogonal ring crossings (separated by  $2\theta_{\text{off}}$ ). The focusing conditions of the pump light are varied by choosing different lens configurations before the crystal. A half-wave plate (HWP) and two 0.5-mm-thick compensating BBO crystals (cc) compensate for the longitudinal and transverse walk-off of the SPDC light. Light emitted along the two orthogonal crossings of the SPDC cones passes apertures (for spatial selection) and  $f = 40$  cm lenses ( $L_1$ ) at 80 cm from the generating crystal before being focused by  $f = 2.5$  cm lenses ( $L_2$ ) onto free-space single photon counters (Perkin Elmer SPCM-AQR-14). Polarizers ( $P$ ) and interference filters (IFs, 10 nm spectral width) combined with red filters (RFs) are used for polarization and spectral bandwidth selection, respectively. Finally, the output signals of the photon counters are received by an electronic circuit which records coincidence counts within a time window of 1.76 ns.

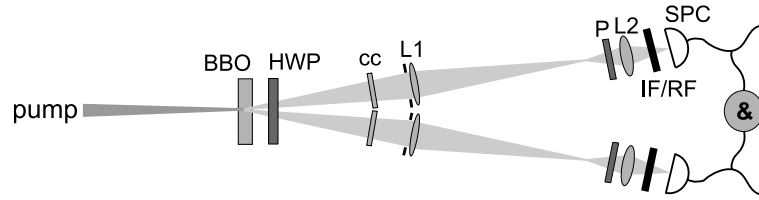


**Figure 6.2:** Schematic view of the experimental setup (see text for details).

In Fig. 6.3 we show the SPDC emission patterns for three different focusing conditions of the pump beam. These pictures were captured with an intensified CCD (Princeton Instruments PI-MAX 512HQ) at 6 cm from the generating BBO crystal behind an interference filter (5 nm spectral width), a red plate and two blue-coated mirrors that are needed to block the pump beam; no imaging lens was used. The three focusing conditions are realized by choosing different lens configurations in front of the BBO crystal. For convenience, we will label these conditions as ‘plane wave’, ‘intermediate’ and ‘extreme’, corresponding to a pump divergence  $\sigma$  of  $0.86 \pm 0.07$  mrad,  $12.0 \pm 0.5$  mrad and  $32 \pm 1$  mrad, respectively. These values were obtained by measuring the (far-field) pump size for the three focusing conditions using a CCD camera (Apogee AP1). For comparison, we note that the external offset angle  $\theta_{\text{off}} \approx 57$  mrad.

In the plane-wave case, our analysis of Fig. 6.3(a) yields a radial width of  $\Delta\theta_r = 10.9 \pm 0.5$  mrad (FWHM), being constant over the entire ring. However, this value is somewhat larger than the true width of the rings as broadening by the  $\approx 0.4$ -mm-wide pump spot is still considerable at 6 cm from the crystal. At a BBO-CCD distance of 12 cm we obtained the better estimate of  $\Delta\theta_r = 8.8 \pm 0.5$  mrad; the same value was measured at larger distances [24]. The absence of asymmetric smearing, and thus the ‘plane-wave’ condition, is not only supported by the measured constant ring width but also by the pump divergence of  $\sigma = 0.86$  mrad, for which Eq. (6.5) predicts a maximal normalized ring width (at bottom) of only  $y = 1.02$ . Furthermore, the measured angular distance between the two crossings of  $2 \times 57 \pm 1$  mrad is equal to the theoretical value of  $2\theta_{\text{off}}$  (with  $\theta_{\text{off}} = 57$  mrad) that is needed for orthogonal ring crossings. The same value is used for the next two cases of focused pumping.

For intermediate focusing [see Fig. 6.3(b) and 6.3(d)] we clearly observe the theoretically-expected asymmetric broadening of both rings: the measured radial width  $\Delta\theta_r$  (FWHM) at the top, middle and bottom of the rings was  $8.3 \pm 0.6$  mrad,  $17 \pm 1$  mrad and  $27 \pm 1$  mrad, respectively. These values are already true widths as we obtained approximately the same values at a BBO-CCD distance of 12 cm. We explain this by the less severe ring broadening by the much smaller pump spot in this case. By using the intermediate (FWHM) pump divergence of  $1.18\sigma = 14.2$  mrad and the measured (FWHM) ring width of 8.8 mrad in the plane-wave case, which combine to  $x(\varphi) = |\mathbf{a}(\varphi)| \times 14.2/8.8$ , Eq. (6.5) predicts (FWHM) ring widths of  $9.7 \pm 0.9$  mrad,  $19 \pm 2$  mrad and  $26 \pm 2$  mrad at the three positions. Within the error margins, the measured values agree well with the predicted (FWHM) values.

The observation of the SPDC emission pattern under extreme focusing [see Fig. 6.3(c)] was limited by the aperture of the collection optics (dark edges) and the presence of extra (near-infrared) fluorescence that was not visible under weaker focusing conditions. The intensity of this fluorescence, which seems to originate from the BBO crystal, was measured to

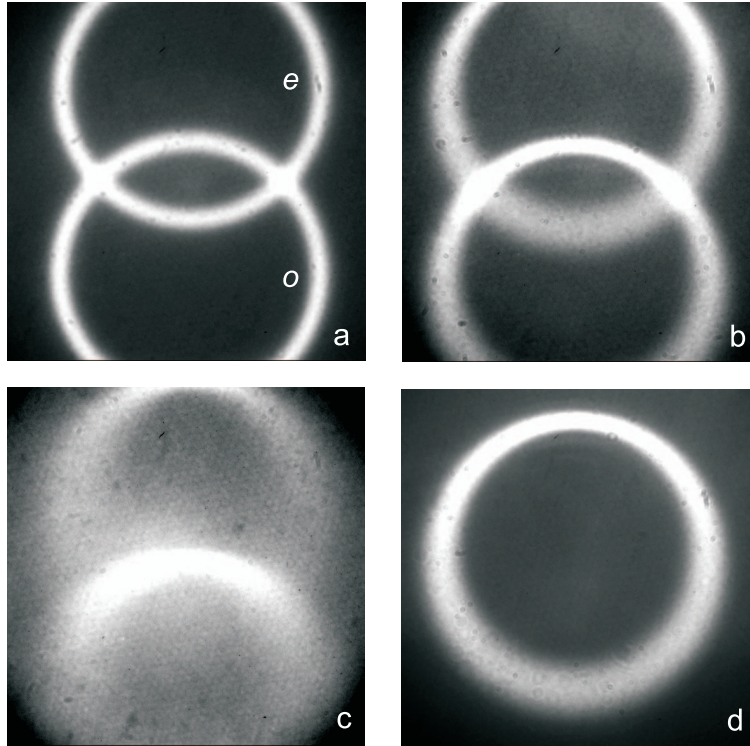


**Figure 6.3:** SPDC emission patterns observed with an intensified CCD at 6 cm from a 1-mm-thick BBO, for three focusing conditions of the pump beam: (a) plane wave ( $\sigma = 0.86 \pm 0.07$  mrad), (b) intermediate ( $\sigma = 12.0 \pm 0.5$ ) and (c) extreme ( $\sigma = 32 \pm 1$  mrad) with exposure times of 1 s, 1.3 s and 0.8 s, respectively. In each of these pictures, the upper and lower ring correspond to extraordinary (e) and ordinary (o) photons, respectively. Picture (d) was taken behind a polarizer to highlight the ordinary ring in (b). All four images cover a space angle of  $220 \times 220$  mrad and contain 100 accumulated snapshots.

be roughly  $4 \times$  higher than the background intensity in the other focusing conditions, making its averaged intensity about  $3.5 \times$  higher than the SPDC intensity in the rings. The measured (FWHM) ring widths  $\Delta\theta$ , of  $10.8 \pm 0.8$  mrad,  $48 \pm 9$  mrad, and  $80 \pm 15$  mrad at the top, middle and bottom of the ring, respectively, indeed reveal an even more severe and asymmetric broadening of the rings in comparison with the other focusing conditions. From the extreme pump divergence of  $\sigma = 32$  mrad, we have calculated (FWHM) corresponding ring widths of  $14 \pm 1$  mrad,  $47 \pm 4$  mrad,  $65 \pm 6$  mrad, which match the measured widths within the error tolerances.

Next, we will compare the photon yield and entanglement quality of the polarization-entangled photon pairs that are generated under the three different focusing conditions. In Fig. 6.4 we show the measured single count rate, quantum efficiency (= coincidence counts / single counts) and biphoton fringe visibility as a function of the aperture diameter. All mea-

6. How focused pumping affects type-II spontaneous parametric down-conversion

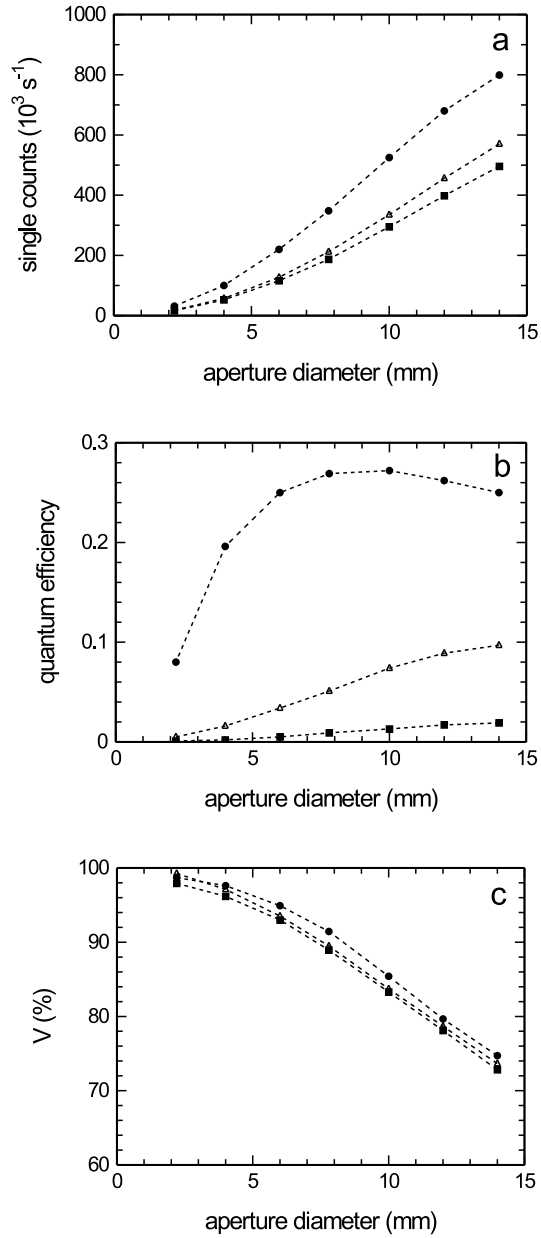


**Figure 6.4:** Single count rate (a), quantum efficiency (b) and polarization fringe visibility  $V$  (c) measured as a function of aperture diameter (at 80 cm from BBO crystal) for three focusing conditions of the pump: plane wave (dots), intermediate (triangles) and extreme (squares).

measurements were performed in the  $45^\circ$ -polarization basis. Figure 6.4(a) shows how the single count rate behind a relatively large 14-mm-diameter aperture drops from  $800 \times 10^3 \text{ s}^{-1}$  in the plane-wave case (circles), to 70% of this value for intermediate focusing (triangles) and 60% under extreme focusing (squares). At smaller apertures the drop is even somewhat more pronounced. The relatively small difference between the intermediate and extreme case is probably due to the excess fluorescence observed in the latter case. The drop in the single count rate for stronger focusing is ascribed to the angular broadening of the ring crossings. The asymmetric character of this broadening creates an imbalance between the ordinary and extra-ordinary count rate at the crossings. In consistency with the SPDC patterns shown in Fig. 6.3, we measured about 5%, 40% and 55% more ordinary than extra-ordinary photons for the plane-wave, intermediate and extreme case, respectively.

Figure 6.4(b) shows the quantum efficiency (= coincidence counts/single counts) as a function of aperture size. The maximum of 0.27 observed for plane-wave pumping is clearly much larger than the maxima observed for intermediate and extreme focusing, where we observed maxima of 0.10 and 0.02, respectively. Focused pumping thus leads to a much stronger reduction in the coincidence count rates than in the single count rates. Figure 6.4(b) also shows that the aperture diameter at which 50% of the maximum quantum efficiency is reached increases from  $\approx 3 \text{ mm}$  ( $\approx 3.8 \text{ mrad}$ ) for the plane-wave case to 7.5 mm and 8.1 mm ( $\approx 10 \text{ mrad}$ ) for the intermediate and extreme case, respectively, although the true maxima of the latter cases might not be reached yet. These numbers demonstrate the increase of the “transverse coherence area” of the down-converted beams, i.e., the angular range in one beam that corresponds to a fixed angle in the other beam, as observable in coincidence imaging [30, 31]. Focused pumping thus breaks the approximate one-to-one relation between the transverse positions of the twin photons observed under plane-wave pumping. This justifies the analogy to the transition from cw to broadband pumping where the exact anticorrelation in frequency between the two beams is destroyed [78].

Figure 6.4(c) shows the biphoton fringe visibility  $V$ , as measured by fixing one polarizer at  $45^\circ$  and rotating the other [8]. For plane-wave pumping  $V$  decreases from  $98.7 \pm 0.2\%$  at 2-mm-wide apertures to  $74.7 \pm 0.5\%$  at 14-mm-wide apertures. Virtually the same behavior is observed for both intermediate and extreme focusing, where the measured visibility is at most 2-3% lower than in the plane-wave case. The entanglement quality is thus not drastically affected by focused pumping. On the other hand, although focused pumping produces wider rings and increased crossing areas, we apparently cannot profit from these increased areas due to a combined spatial/polarization labeling of the photon pairs. By reducing the aperture size we effectively remove this labeling and increase the entanglement quality, but this reduces the photon yield, the more so the stronger the focusing. For the considered geometry of bucket detectors behind apertures, focused pumping has no clear advantages. Mild focusing is expected to lead to a slightly increased yield in coincidence imaging [30, 31].

We will end with a discussion of the effects of focused pumping on the optical spectrum, thus removing the restriction of narrow-band spectral detection. For the geometry with bucket detectors behind small apertures the width of the optical spectrum is determined by the combination of the ring size and the “angular dispersion”, i.e., the change in ring diameter with wavelength. Since the two ring sizes differ at the crossings due to asymmetric ring broadening, and since the angular dispersion is a material property [32], focused pumping should lead to a different  $o$ - and  $e$ -spectrum, and thus to spectrally labeled photons at the

crossings. The same argument applies to the single-mode geometry based on fiber-coupled detectors. The focusing used by Kurtsiefer *et al.* [23] must have been just mild enough to miss the predicted effect. We predict that stronger focusing would have led to the mentioned spectral difference, thus enforcing the use of spectral filters in order to obtain a high polarization visibility.

A quick glance at Fig. 6.3 shows that the  $e$ -ring is wider than the  $o$ -ring at the crossing, making the  $e$ -spectrum at this fixed collection angle wider than the  $o$ -spectrum. Interestingly enough, the asymmetry in this type of spectral widening is just opposite from the spectral asymmetry predicted by Grice and Walmsley for pulsed pumping [78], where the  $o$ -spectrum is wider than the  $e$ -spectrum. Proper balancing of focused pumping and pulsed excitation could thus remove the spectral asymmetry, and all spectral labeling.

## 6.4 Concluding discussion

We have investigated the effects of focused pumping on type-II SPDC. In particular, we have shown that focused pumping leads to an asymmetric broadening of both the SPDC emission cones. This is similar to asymmetric spectral broadening discussed in [78] for pulsed pumping of “focusing in time”. For pair collection with two bucket detectors behind apertures, focused pumping seems to have no clear advantages; the polarization entanglement at fixed pinhole size is virtually unaffected, but the single and especially the coincidence count rates are reduced. For detection with fiber-coupled photon counters, where focused pumping is necessary for efficient single-mode generation, severe focusing is predicted to produce polarization-unbalanced spectral broadening which leads to a reduced entanglement quality.

## 6.5 Acknowledgments

This work has been supported by the Stichting voor Fundamenteel Onderzoek der Materie; partial support is from the European Union under the IST-ATESIT contract.

## CHAPTER 7

---

### Polarization entanglement behind single-mode fibers: spatial selection and spectral labeling

---

*We study the limitations to the polarization entanglement of photon pairs that are generated via type-II spontaneous parametric down-conversion (SPDC). By employing single-mode detection behind optical fibers, we demonstrate the incompleteness of the mode-matching concept presented in Ref. [23]. Using free-space detection behind apertures as well, we demonstrate that the higher entanglement quality obtained behind single-mode fibers is due to the removal of the spatial labeling. In addition, we show that the residual spectral labeling after selection with fibers is due to imperfect phase matching.*

## 7.1 Introduction

Type-II spontaneous parametric down-conversion in a nonlinear birefringent crystal provides for a popular source of polarization-entangled twin photons in the field of experimental quantum optics and quantum information [8, 11, 15, 58]. In this generation process, one unavoidably encounters both longitudinal and transverse walk-off effects that are caused by the birefringent nature of the crystal. These make the polarizations of the twin photons distinguishable through their temporal and spatial information, respectively. This is also known as *labeling*. In order to restore the indistinguishability and thus the degree of polarization entanglement, Kwiat *et al.* [8] introduced a simple compensating device. It consists of one half-wave plate and two additional crystals, identical to the down-conversion crystal but of half the length. This device is now commonly used in several experimental schemes [23, 24, 56, 81].

The described compensating device is not perfect. With its frequency- and angle-dependent birefringence it can make the *phase* factors of the two contributing biphoton amplitude functions identical. The *amplitude* factors can however still be different, which implies that the obtained degree of polarization entanglement may still suffer from labeling, even when compensating crystals are used. In this chapter we study the limitations that spatial and spectral labeling impose on the attainable quality of the polarization entanglement.

Spatial labeling information, which is dosed by the detected angular width of the SPDC light, can be erased by transverse mode selection via single-mode fibers before photon detection. Kurtsiefer *et al.* [23] successfully pioneered this detection method to obtain both a large photon-pair collection and a high quality of polarization entanglement ( $\approx 96\%$ ). However, the geometric requirement mentioned in Ref. [23], being the matching of pump and fiber mode, is not sufficient. We will show that an optimal yield of photon pairs needs extra matching with a third spatial parameter. Moreover, the benefit of fiber detection above the more conventional detection behind apertures was not highlighted in [23]. In this chapter we explicitly demonstrate that spatial labeling plays a crucial role in the comparison between these two schemes, especially in relation to the polarization entanglement quality. Furthermore, we show how pump beam properties can affect the entanglement measured behind single-mode fibers.

## 7.2 Theory

The theoretical description of polarization entanglement created under type-II SPDC can be found in Chapter 2. As a reminder, we mention that the polarization-entangled state at the intersections 1 and 2 of the two emitted SPDC light cones is given by the complete biphoton wavefunction [see also Eq. (2.7)]

$$|\Psi\rangle = \int d\mathbf{q}_1 d\mathbf{q}_2 d\omega_1 d\omega_2 \{ \Phi_{HV}(\mathbf{q}_1, \omega_1; \mathbf{q}_2, \omega_2) |H_1, \mathbf{q}_2, \omega_1; V_2, \mathbf{q}_2, \omega_2\rangle + \Phi_{VH}(\mathbf{q}_1, \omega_1; \mathbf{q}_2, \omega_2) |V_1, \mathbf{q}_1, \omega_1; H_2, \mathbf{q}_2, \omega_2\rangle \}, \quad (7.1)$$

where integration is over the transverse wavevectors  $\mathbf{q}_1$  and  $\mathbf{q}_2$  and frequencies  $\omega_1$  and  $\omega_2$ . The state  $|H_1, \mathbf{q}_1, \omega_1; V_2, \mathbf{q}_2, \omega_2\rangle$  corresponds to the presence of one *H*-polarized photon with wavelength  $\omega_1$  and transverse wavevector  $\mathbf{q}_1$  in beam 1 and its *V*-polarized partner

photon with wavelength  $\omega_2$  and transverse wavevector  $\mathbf{q}_2$  in beam 2. A potential difference between the biphoton amplitude functions  $\Phi_{HV}$  and  $\Phi_{VH}$  is denoted as labeling and reduces the quality of the polarization entanglement. For free-space detection with bucket detectors behind apertures the degree of polarization entanglement is given by the biphoton visibility [see also Eq. (2.8)]

$$V = \frac{\langle\langle 2\text{Re}(\Phi_{HV}^* \Phi_{VH}) \rangle\rangle}{\langle\langle |\Phi_{HV}|^2 + |\Phi_{VH}|^2 \rangle\rangle}. \quad (7.2)$$

The double brackets  $\langle\langle \dots \rangle\rangle$  denote the six-fold integration over the momenta  $\mathbf{q}_1$  and  $\mathbf{q}_2$  and frequencies  $\omega_1$  and  $\omega_2$ , determined by the two spatial apertures and the transmission spectra of the two bandwidth filters, respectively.

In this chapter we also study the polarization entanglement observed behind *single-mode fibers* using fiber-coupled detectors [23, 56, 82]. In this case, the above equations remain basically the same; only the biphoton amplitude functions  $\Phi_{ij}$  will change into the projected amplitude functions

$$\alpha_{ij}(\omega_1, \omega_2) = \int \int d\mathbf{q}_1 d\mathbf{q}_2 \Phi_{ij}(\mathbf{q}_1, \omega_1; \mathbf{q}_2, \omega_2) \psi_{\text{fiber1}}^*(\mathbf{q}_1) \psi_{\text{fiber2}}^*(\mathbf{q}_2). \quad (7.3)$$

Here,  $\psi_{\text{fiber1}}(\mathbf{q}_1)$  and  $\psi_{\text{fiber2}}(\mathbf{q}_2)$  are the transverse mode profiles of the single-mode fibers in beam 1 and 2. Similar to Eq. (7.2), the degree of polarization entanglement can now be expressed as

$$V_{\text{fiber}} = \frac{\langle 2\text{Re}(\alpha_{HV}^* \alpha_{VH}) \rangle}{\langle |\alpha_{HV}|^2 + |\alpha_{VH}|^2 \rangle}, \quad (7.4)$$

where the single brackets denote a two-fold integration over the frequencies  $\omega_1$  and  $\omega_2$  only, over ranges determined by the transmission windows of the spectral filters in beam 1 and 2. It is obvious that Eq. (7.4) contains no spatial labeling information as the amplitude functions  $\alpha_{ij}(\omega_1, \omega_2)$  depend only on frequency. In comparison with detection behind apertures, detection behind single-mode fibers should thus result in a higher degree of polarization entanglement. The sole limitation that can now potentially affect the polarization entanglement is spectral labeling.

## 7.3 Experimental results

### 7.3.1 Experimental setup

The experimental setup is schematically depicted in Fig. 7.1. Light from a cw krypton-ion laser, operating at 407 nm, is focused on a 1-mm-thick birefringent  $\beta$ -barium borate (BBO) crystal. The two cones of light that are emitted at 814 nm under type-II SPDC intersect each other perpendicularly, thereby defining two slightly diverging light paths which are both spaced at an angle of about  $3^\circ$  with respect to the pump beam. One half-wave plate and two 0.5-mm-thick BBO crystals (one in each arm) compensate for walk-off effects in the down-conversion crystal. After passing through apertures the light is imaged by a  $f = 40$  cm lens, positioned at 80 cm from the down-conversion crystal, to an intermediate focus,

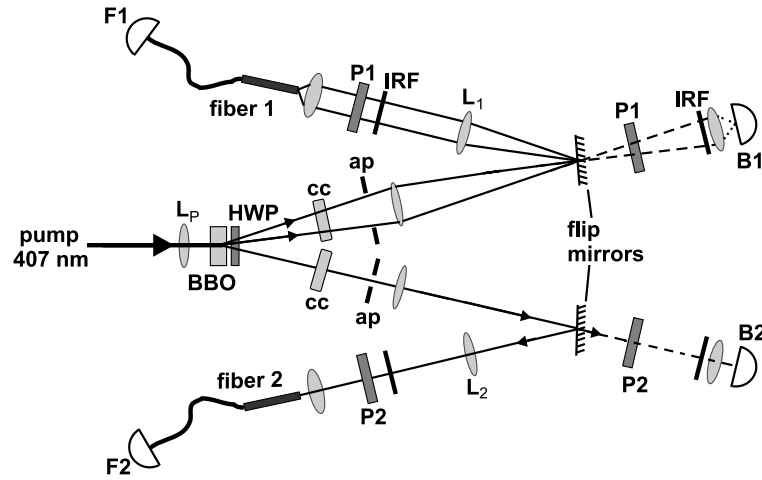


**Figure 7.1:** Experimental setup. Lens  $L_p$  focuses the pump beam on a birefringent BBO crystal. A half-wave plate HWP and two compensating crystals cc form the standard compensating device. Flip-mirrors allow for an easy switch between two detection schemes. Mirrors flipped up, solid paths: detection with fiber-coupled detectors  $F_1$  and  $F_2$ . Lenses  $L_1$  and  $L_2$  are used to direct parallel beams onto the fiber-coupling lenses. Mirrors flipped down, dashed paths: detection with bucket detectors  $B_1$  and  $B_2$ . Both schemes have apertures ap, polarizers  $P_1$  and  $P_2$ , and interference/red filters IRF.

where we have an one-to-one image of the generating area on the BBO. Flip-mirrors placed at this focus allow for easy switching between our two detection systems. When the mirrors are flipped up, light is directed into 2-m-long single-mode fibers, via imaging lenses and  $f = 11$  mm collecting lenses, before being detected by fiber-coupled counting modules (Perkin Elmer SPCM-AQR-14-FC). Spatial selection is now obtained mainly from the fibers, but also somewhat from the extra apertures that are positioned between crystal and flip-mirrors. When the mirrors are flipped down, photons propagate directly to bucket detectors (Perkin Elmer SPCM-AQR-14) and only the mentioned apertures account for spatial selection. In both systems polarizers and interference filters ( $\Delta\lambda = 10$  nm) are used for polarization and frequency selection, respectively. A very fast electronic coincidence circuit with a time window of 1.76 ns receives the detector signals and measures the rate of entangled photon pairs.

### 7.3.2 Mode matching

Detection of SPDC light behind single-mode fibers will generally result in a relatively low yield of entangled photon pairs since the detectors per definition observe only one of the many generated transverse modes. The characterization of the fiber-coupling efficiency in terms of experimental parameters has been studied in [56, 82]. The optimal collection of photon pairs behind single-mode fibers has been experimentally demonstrated by Kurtsiefer *et al.* [23], who showed that transverse matching of the pump mode and the fiber-detected mode is necessary. We will now demonstrate that his discussion of mode matching is incomplete and

**Table 7.1:** Measured count rates and visibilities for different geometries of the fiber-detection scheme.

$w_p(\mu\text{m})$	$w_f(\mu\text{m})$	$R_s(10^3\text{s}^{-1})$	$R_{\text{max}}(10^3\text{s}^{-1})$	$V_{45^\circ}(\%)$	$V_{135^\circ}(\%)$
$280 \pm 10$	$65 \pm 5$	10.5	1.53	97.5	99.2
$68 \pm 2$	$65 \pm 5$	247	58.9	98.3	98.4
	$33 \pm 1$	154	20.7	95.3	95.6
$30 \pm 1$	$65 \pm 5$	294	40.9	98.2	97.4
	$33 \pm 1$	223	23.3	95.8	96.5

support this statement with explicit measurements.

According to Kurtsiefer *et al.* [23], mode matching only refers to the matching of the pump waist  $w_p$  and the width  $w_f$  of the back-traced image of the fiber on the down-conversion crystal:  $w_p \approx w_f$ . If  $w_p > w_f$  near-field losses will occur as some of the produced photon pairs are invisible to the back-traced fiber image. The condition  $w_p < w_f$  creates comparable losses as this corresponds to a situation where the angular spread of the SPDC light is certainly larger than the far-field size of the fiber mode. The underlying reason for the joint near-field and far-field match is that the fiber selects a true single transverse mode in both  $\mathbf{r}$ - and  $\mathbf{k}$ -space, in contrast to the mode selection in  $\mathbf{r}$ -space performed by apertures.

The matching condition  $w_p \approx w_f$  is not sufficient. Full mode matching requires additional matching to a third spatial parameter, namely the (maximum) internal transverse walk-off  $w_w$  between the ordinary and extra-ordinary beam (equivalent to  $\rho L$  in Sec. 2.2.2), making the full matching condition  $w_p \approx w_f \approx w_w$ . If  $(w_p \approx w_f) < w_w$  the fiber cannot simultaneously match the different near-field profiles of the ordinary and extra-ordinary light. On the other hand, the condition  $(w_p \approx w_f) > w_w$  implies a limited observation of the SPDC pattern in the far field, as  $w_w$  is Fourier-related to the angular width of the SPDC light [see Eq. (2.6)]. We will now experimentally demonstrate the mode matching of the above three parameters to obtain an optimal yield of photon pairs behind single mode fibers.

Table 7.1 shows the typical single count rates  $R_s$ , coincidence count rates  $R_{\text{max}}$  and visibilities  $V$  that are measured for different geometries in the fiber-detection scheme (aperture fully open at  $d = 17$  mm). The pump waist  $w_p$  is realized by the choice of the proper pump focusing lens  $L_p$ . The two fiber-detected waists  $w_f = 33 \mu\text{m}$  and  $w_f = 65 \mu\text{m}$  are obtained with  $f = 10$  cm and  $f = 20$  cm imaging lenses  $L_1$ , respectively (see Fig. 7.1). The transverse walk-off in our 1-mm-thick BBO crystal is  $w_w \approx 70 \mu\text{m}$ .

In the case of  $w_p = 280 \mu\text{m}$  and  $w_f = 65 \mu\text{m}$ , where the pump waist  $w_p$  is neither matched to  $w_f$  nor to the walk-off  $w_w$ , we measure a coincidence rate of  $R_{\text{max}} = 1.53 \times 10^3 \text{ s}^{-1}$ . If we now reduce the pump waist to  $w_p = 68 \mu\text{m}$  but keep the same  $w_f$ , such that all three parameters are matched, we measure an almost 40 times higher rate of  $R_{\text{max}} = 58.9 \times 10^3 \text{ s}^{-1}$ . Table 7.1 obviously shows that a further reduction of the pump waist to  $w_p = 30 \mu\text{m}$  destroys the complete matching and therefore yields a lower rate of  $R_{\text{max}} = 40.9 \times 10^3 \text{ s}^{-1}$ . If we also

switch to a smaller fiber-detected waist of  $w_f = 33 \mu\text{m}$  in the latter case, such that again  $w_p \approx w_f$ , we obtain an even lower coincidence rate of  $R_{\text{max}} = 23.3 \times 10^3 \text{ s}^{-1}$ . This clearly shows that the matching condition  $w_p \approx w_f$  is not sufficient for an optimal collection of photon pairs. Instead, we have hereby demonstrated that a joint matching of all three parameters is needed to obtain the maximal pair rate of  $R_{\text{max}} = 58.9 \times 10^3 \text{ s}^{-1}$ . Operating at a pump power of 207 mW, this rate corresponds to a slope efficiency of  $R_{\text{max}} \times 2 \times 1.7 / 207 = 970 \text{ s}^{-1}\text{mW}^{-1}$ . The factors 2 and 1.7 correct for the use of polarizers and interference filters, respectively (see discussion around Fig. 7.4). Our measured efficiency then compares well to the value of  $900 \text{ s}^{-1}\text{mW}^{-1}$  that was obtained by Kurtsiefer *et al.* [23] in absence of both polarizers and interference filters .

### 7.3.3 Free-space detection versus fiber-coupled detection

Next we compare both the degree of polarization entanglement and the coincidence rate obtained with free-space detection behind apertures on the one hand and with fiber-coupled detectors on the other hand (see Fig. 7.1 for setup). The degree of polarization entanglement can be deduced from the maximum coincidence count rate  $R_{\text{max}}$  and the minimum coincidence count rate  $R_{\text{min}}$ , measured upon rotation of polarizer 2 at fixed orientation  $\varphi_1$  of polarizer 1. The degree of entanglement is then given by the coincidence fringe visibility

$$V_{\varphi_1} \equiv \frac{R_{\text{max}} - R_{\text{min}}}{R_{\text{max}} + R_{\text{min}}} . \quad (7.5)$$

In the natural crystal basis we measure typically  $V_{0^\circ} \approx V_{90^\circ} = 99.4 \pm 0.3\%$ . Only the visibilities  $V_{45^\circ}$  and  $V_{135^\circ}$  are closely related to the experimental implementation of Eq. (7.2) and Eq. (7.4).

Table 7.1 shows a measured visibility of  $V = 98.4\%$  for the best-matched geometry of the fiber-detection scheme. In contrast, free-space detection yields only  $V = 80.0\%$  under the same conditions ( $d = 14 \text{ mm}$  and  $w_p = 68 \mu\text{m}$ ). We can, however, improve the entanglement quality attained with free-space detection to that of the fiber-detection scheme, if we detect behind sufficiently small apertures. For instance, we already measure a visibility of  $V = 90.0\%$  behind 9 mm apertures, whereas we even obtain a value of  $V = 97.0\%$  behind 4 mm apertures. In Figure 7.2 we show the visibilities  $V_{45^\circ}$  and  $V_{135^\circ}$  measured as a function of the aperture diameter  $d$  for both detection schemes, using  $w_p = 68 \pm 1 \mu\text{m}$  and  $w_f = 65 \pm 5 \mu\text{m}$ . For free-space detection, we clearly observe the ‘‘dramatic’’ increase in visibility with decreasing aperture sizes mentioned above. For fiber-coupled detection, we measure (much) higher visibilities of at least  $V = 97.5\%$  for all considered aperture sizes. We ascribe this strong contrast in entanglement quality between the two detection schemes to the removal of spatial labeling by the mode-selective character of the fibers. In fact, the fibers select a pure fundamental transverse mode in both  $\mathbf{r}$  and  $\mathbf{k}$ -space, irrespective of the aperture size, which explains the constantly high visibilities shown in Fig. 7.2. Instead, apertures perform mode selection only in the transverse  $\mathbf{r}$ -space, which leads to enhanced polarization distinguishability and thus lower visibilities for larger apertures.

Unfortunately, the improvement of the entanglement quality for detection behind smaller apertures (see Fig. 7.2) is unavoidably accompanied by a drastic loss of signal strength. Whereas the visibility increases from  $V = 80.0\%$  at 17 mm apertures to  $V = 90.0\%$  at 9

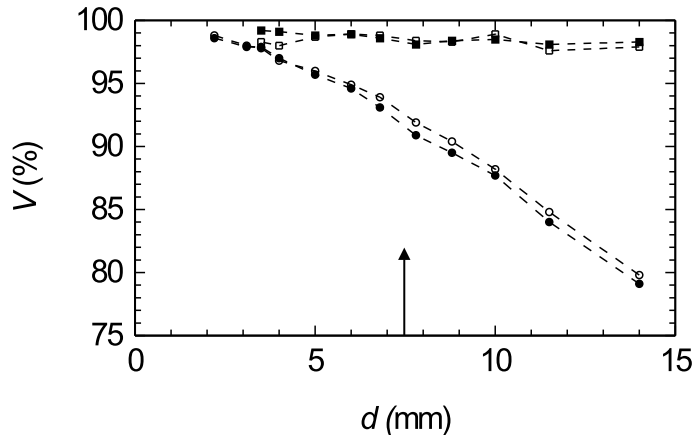


**Figure 7.2:** Visibilities  $V_{45^\circ}$  (filled marks) and  $V_{135^\circ}$  (open marks) measured as a function of aperture diameter  $d$  (at 80 cm from the crystal) for detection behind single-mode fibers (squares) and apertures (circles) at  $w_p = 68 \mu\text{m}$  and  $w_f = 65 \mu\text{m}$ . The arrow at  $d = 7.5 \text{ mm}$  marks the typical size of the fiber mode in the aperture plane, being the diameter at which the single count rate was reduced to 50% of its maximum value.

mm apertures and  $V = 97.0\%$  at 4 mm apertures, the coincidence rate drops from  $R_{\text{max}} = 156 \times 10^3 \text{ s}^{-1}$  to  $R_{\text{max}} = 90.0 \times 10^3 \text{ s}^{-1}$  and  $R_{\text{max}} = 10.6 \times 10^3 \text{ s}^{-1}$ , respectively. We can enhance the photon yield somewhat, without suffering in the entanglement, by increasing the pump size. For a pump waist of  $w_p = 280 \mu\text{m}$  instead of  $w_p = 68 \mu\text{m}$ , we measure a higher rate of  $R_{\text{max}} = 33 \times 10^3 \text{ s}^{-1}$  behind 4 mm apertures, thereby obtaining a visibility of  $V = 97.7\%$ . This improvement in coincidence counts is explained by the smaller SPDC diffraction angle, i.e., the angular spread in one of the two beams that corresponds to a fixed angle in the other beam, as also observed in coincidence imaging [30, 31]. Under this wide-beam condition, free-space detection seems to be favorable above fiber-coupled detection, where we measured only  $R_{\text{max}} = 1.53 \times 10^3 \text{ s}^{-1}$  using the same  $w_p = 280 \mu\text{m}$ . However, the best-matched geometry of the fiber-detection scheme still remains most beneficial as it combines a high visibility of  $V = 98.4\%$  with a high coincidence rate of  $R_{\text{max}} = 58.9 \times 10^3 \text{ s}^{-1}$  (see Table 7.1).

To summarize, free-space detection is most useful when a large yield of photon pairs is necessary while a high polarization entanglement quality is less crucial. If one wants to improve the degree of entanglement obtained behind apertures, one will inevitably lose some of the generated coincidence pairs. In this respect, we have demonstrated that the best-matched geometry (using  $w_p = 68 \mu\text{m}$  and  $w_f = 65 \mu\text{m}$  in our case) in the fiber-coupled detection scheme is most promising when both high entanglement quality and high count rates are accounted for.

### 7.3.4 Spectral labeling

We will now focus on the limitations to the polarization entanglement that is measured via fiber-coupled detection; these limitations must be attributed to frequency labeling only [see

Eq. (7.3)]. A detailed look at Fig. 7.2 shows that the visibility measured with this scheme is not perfectly 100% and even drops very slightly with increasing aperture sizes. Moreover, we obtain similar visibilities when using 10 m fiber instead of the usual 2 m, which confirms the complete removal of spatial labeling and the presence of spectral labeling only.

Mathematically speaking, the reduction of entanglement quality due to spectral labeling can only be explained by differences between the two projected amplitude functions, i.e.,  $\alpha_{HV}(\omega_1, \omega_2) \neq \alpha_{VH}(\omega_1, \omega_2)$ . As the projected amplitude functions can be written as  $\alpha_{ij}(\omega_1, \omega_2) = E_p(\omega_1 + \omega_2) \cdot \phi_{ij}(\omega_1, \omega_2)$ , the frequency labeling must be contained in the asymmetry of the phase-matching functions, i.e.,  $\phi_{HV}(\omega_1, \omega_2) \neq \phi_{VH}(\omega_1, \omega_2)$ ; the spectral pump profile  $E_p(\omega_1 + \omega_2)$  does not contain any polarization labels. Below we will discuss experimental results that specifically show that phase matching indeed causes the spectral labeling and thus the limited entanglement quality.

First of all, Table 7.1 shows that the visibility decreases from roughly  $V = 98\%$  to  $V = 96\%$ , for both the focusing conditions  $w_p = 30 \mu\text{m}$  and  $w_p = 68 \mu\text{m}$ , when the size of the observed pump region is reduced from  $w_f = 65 \mu\text{m}$  to  $w_f = 33 \mu\text{m}$ . The reduction in this near-field size corresponds to an increase of the fiber-detected SPDC crossing area in the far field. As a larger observation angle also implies a larger detected spectral bandwidth [23], we will operate further from the thin-crystal limit. In this respect, it is not surprising that the degree of entanglement will suffer even more from the above phase-matching asymmetry.

A second contribution to the spectral labeling could be a (slight) misalignment of the optical fibers. If the fibers are not properly centered around the degeneracy points of the crossing area, the  $H$ - and  $V$ -polarized spectra will be different because of the frequency matching ( $\omega_1 + \omega_2 = \omega_p$ ) that is associated with the energy conservation. This again leads to different phase-matching functions  $\phi_{HV}$  and  $\phi_{VH}$  which creates labeling of the two polarizations. Furthermore, even if the fiber alignment is perfect, the degree of entanglement may still suffer from the slightly different bandwidth of the  $H$ - and  $V$ -polarized light, which we have measured and discussed in Chapter 4 [53].

Intriguingly, we have also observed a limitation of the degree of entanglement due to the power of the pump laser. In Fig. 7.3 we show the visibility measured as a function of the pump power in the fiber-detection scheme, either using  $\Delta\lambda = 10 \text{ nm}$  (FWHM) interference filters (dots) or no filters (squares). Here, the apertures are fully open (at  $d = 17 \text{ mm}$ ),  $w_p = 68 \mu\text{m}$  and  $w_f = 65 \mu\text{m}$ . With interference filters we measure visibilities of  $V \approx 98\%$  at low pump powers which drop to  $V \approx 97\%$  at a power of  $\approx 300 \text{ mW}$ . When these filters are removed, the reduction from  $V \approx 96\%$  to  $V \approx 92\%$  in the same power range is more drastic. The observed visibility drop is probably related to a modified pump profile as a result of changes in the temperature and gain guiding in our  $\text{Kr}^+$  laser with increased output power. Using a shear interferometer (Melles Griot Wavealyzer) we have observed that an increase in pump power is accompanied by both a larger beam divergence and a transition from a circular to an elliptical cross-section with  $V/H$  ratio  $\approx 1.2$ . This modified pump profile changes the biphoton amplitude function  $\Phi_{ij}$  [see Eq. (7.3)] and thereby its spatially-integrated form  $\alpha_{ij}(\omega_1, \omega_2)$  and the corresponding phase-matching function  $\phi_{ij}(\omega_1, \omega_2)$ . The exact analysis of the observed behaviour in Fig. 7.3 in relation to the beam profile goes beyond the scope of this chapter.

In Fig. 7.4 we show the measured coincidence rates  $R_{\text{max}}$  as a function of the pump power, obtained with and without interference filters in the best-matched fiber-detection geometry. In

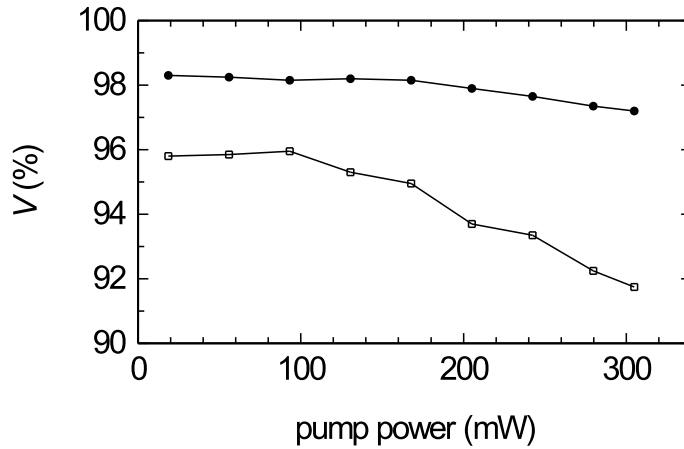


**Figure 7.3:** Averaged visibility  $(V_{45^\circ} + V_{135^\circ})/2$  measured as a function of the pump power, with  $\Delta\lambda = 10$  nm interference filters (dots) and without interference filters (squares) in the best-matched geometry of the fiber-detection scheme.

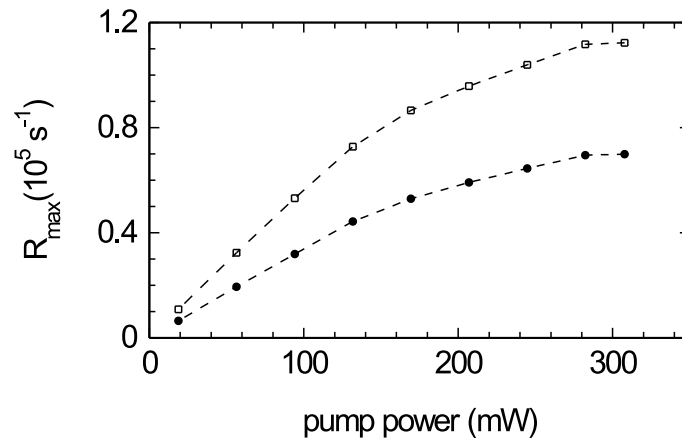


**Figure 7.4:** Coincidence rates  $R_{\max}$  measured as a function of the pump power, with  $\Delta\lambda = 10$  nm interference filters (dots) and without interference filters (squares) in the best-matched geometry of the fiber-detection scheme.

absence of the filters we measure 1.7 times higher coincidence rates, which we mainly ascribe to the signal gain of  $1/(0.8)^2 = 1.56$  that we calculate from the  $T = 80\%$  peak transmission of both filters. The residual gain of  $1.7/1.56 \approx 1.1$  agrees well with the expected bandwidth increase by a factor of 1.15 which is based on the natural SPDC bandwidth of  $\Delta\lambda_{\text{SPDC}} = 11.5$  nm (see Chapter 4) that we detect without  $\Delta\lambda = 10$  nm filters. The smaller detection bandwidth of  $\Delta\lambda = 10$  nm, which is associated with less spectral labeling, also explains the somewhat higher visibilities obtained with interference filters (see Fig. 7.3). On the other hand, the fact that  $\Delta\lambda$  is just smaller than  $\Delta\lambda_{\text{SPDC}}$  indicates that we are not yet operating sufficiently far in the thin-crystal limit and phase matching could thus still limit the attainable

entanglement quality.

Finally, Fig. 7.4 shows a clear saturation of the coincidence rate at higher pump powers, which was also observed by Kurtsiefer *et al.* [23]. This saturation is probably caused by the increased pump divergence mentioned above. As a larger pump divergence implies a larger SPDC diffraction angle, the photon-pair collection within the same aperture will be reduced and saturation will occur. We note that the presented count rates are still low enough to keep saturation effects due to detector deadtimes below the few-percent level.

## **7.4 Conclusion**

We have investigated the limitations to the polarization entanglement in a type-II SPDC setup that employs both free-space detection behind apertures and single-mode detection behind optical fibers. We have demonstrated that optimal photon-pair collection with the latter scheme requires matching to a third parameter, being the birefringent walk-off, apart from the matching of the pump waist and the fiber-detected waist [23]. We ascribe the higher entanglement quality that is measured with the fiber-detection scheme to the erasure of spatial labeling by the single-mode fibers. The remaining spectral labeling comes in essence from imperfect phase matching.

---

### Spatial labeling in a two-photon interferometer

---

*We study the spatial coherence of entangled photon pairs that are generated via type-I spontaneous parametric down-conversion (SPDC). By manipulating the spatial overlap between the two down-converted beams in a Hong-Ou-Mandel interferometer we observe the spatial interference of multiple transverse modes for an even and an odd number of mirrors in the interferometer. We demonstrate that the two-photon spatial coherence, which is quantified in terms of a transverse coherence length, differs completely for the two mirror geometries and support this result by a theoretical and experimental explanation in terms of photon labeling.*

*P.S.K. Lee and M.P. van Exter, Phys. Rev. A **73**, 063827 (2006).*

## 8.1 Introduction

In the last two decades, the use of entangled photon pairs has become a popular tool for several experimental studies on both the foundations [5, 8, 27] and applications [15, 59] of quantum mechanics. One of the most fascinating among these experiments has been introduced by Hong, Ou and Mandel in order to measure the coherence length of a two-photon wavepacket produced under spontaneous parametric down-conversion [27]. In this original two-photon interference experiment, which we will simply call the HOM experiment, two entangled photons that arrive simultaneously at the two input ports of a beamsplitter will effectively 'bunch' and together exit one of the two output ports. As a consequence, no coincidence events are measured between photon detectors placed in each output channel. As soon as the two photons become distinguishable due to a time delay between the two input beams, the coincidence rate will reappear. Therefore, the coincidence rate measured as a function of the relative time delay shows a minimum at zero delay, which is now known as the HOM dip.

Pittman *et al.* [83] showed that HOM interference is also possible if the two photons arrive at different times at the beamsplitter, provided that the detectors can not distinguish one probability path from another; the interference actually occurs between the two probability paths of the photon pair and not between the individual photons. Rarity and Tapster [84] demonstrated that two-photon (HOM) interference is even possible between two *uncorrelated* photons from independent sources. This experiment, which has been repeated by several groups [85, 87], is however only possible if the two photons are completely indistinguishable. More precisely, these photons have to arrive at the same time (within the inverse detection bandwidth) and in the same spatial mode. Experimentally, this requires pulsed pumping [84] and single-mode (fiber-coupled) detection, respectively. In case of cw pumping, the existence of two-photon interference is in fact a proof of time entanglement; while the individual arrival times of the photons in the generated pairs are undetermined, these two times are strongly quantum-correlated. If the detectors observe many transverse modes, a similar argument shows that two-photon interference is only possible if the two photons are spatially entangled; while the spatial profiles of each of the photons is undetermined, a measurement on one photon co-determines the position and momentum of the other.

Since its initial demonstration in 1987, the HOM interferometer has been employed in several experimental schemes. Like the original experiment, most of these HOM experiments focus merely on the temporal coherence of the two-photon wavepacket [86–88]. Only recently, some papers have reported on the spatial aspects of the HOM experiment [89–91]. Walborn *et al.* [89] have demonstrated how the transverse spatial symmetry of the pump beam affects the two-photon interference: for a symmetric two-photon polarization state, one can make the transition from a HOM dip to HOM peak by changing the pump profile from even to odd. Caetano *et al.* [90] and Nogueira *et al.* [91] have performed coincidence imaging experiments, measuring the coincidence rate behind two small detectors as a function of their transverse position. Using an anti-symmetric pump profile, they observed spatial anti-bunching of the two photons in the coincidence image.

So far, all reported experiments have used perfect spatial overlap between the signal and idler beams and studied the two-photon interference mostly as a function of the temporal delay in the HOM interferometer. Spatial aspects of a HOM interferometer, in a collapsed

type-II collinear geometry, have been studied via the shape, size and displacement of the detection apertures, but the generated beams remained unchanged [26]. The effect of a possible size difference between two non-overlapping beams has been studied theoretically in few-photon interference [92], but beam displacements were not considered. In this paper, we will present the first experimental results on two-photon interference under the influence of a physical separation of the signal and idler beams in the transverse plane. For this purpose, we have used a more general HOM interferometer which employs not only a longitudinal and but also a transverse displacement of one beam with respect to the other.

By measuring coincidences as a function of the beam displacement we determine the transverse coherence length of the two-photon wavepacket for different detection geometries, i.e., different numbers of interfering transverse modes. The key question is how the two-photon spatial coherence manifests in an interferometer with either an even or an odd number of mirrors in the combined signal and idler path. We find that the mirror geometry of the interferometer does indeed play a crucial role. When the total number of mirrors is even, the observed spatial interference is sensitive only to the sum of both coordinates and thereby to the profile of the pump. In case of an odd number of mirrors, one probes the two-photon coherence in the difference coordinate, and thereby basically observes the spherical wavefronts of point sources. Most of our experiments have been performed with an odd number of mirrors, a geometry that has not been studied before.

This paper is organized as follows. In Sec. 8.2 we present a theoretical description of two-photon (HOM) interference for both an even and an odd mirror geometry, including both temporal and spatial degrees of freedom. Our experimental results can be found in Sec. 8.3, which is split into the following subsections. After introducing the experimental setup in Sec. 8.3.1, we present our experimental results on temporal labeling in Sec. 8.3.2 and on spatial labeling in Sec. 8.3.3. In Sec. 8.3.4 we analyze the spatial aspects from a different perspective, using a discrete modal basis. We end with a concluding discussion in Sec. 8.4.

## 8.2 Theoretical description

### 8.2.1 The generated two-photon field

The calculation of the two-photon interference observed in a general HOM interferometer, with a combined temporal delay and transverse spatial shift in one of the arms, is mainly a matter of good bookkeeping. This bookkeeping deals to a large extent with the coordinate changes between two reference frames. The *lab frame*, having its  $z$ -axis along the pump beam and the surface normal of the crystal, is the natural choice for the generated field. The two *local beam frames* that are oriented along the two beam directions are the natural coordinate systems at the detectors. To simplify the notation we will display only one spatial direction, being the  $x$  coordinates in the plane through the signal and idler beam.

We consider two-photon emission by spontaneous parametric down-conversion (SPDC) in the so-called thin-crystal limit, where the detected space angle and spectral bandwidth have to be much smaller than the generated SPDC ring size and bandwidth, respectively. In this limit, the generated two-photon wave function is [34]

$$\psi_z(x_s, x_i; \Delta\omega) = \int E_p(x) h(x_s, x; \omega_s) h(x_i, x; \omega_i) dx \quad (8.1)$$

where  $E_p(x)$  is the field profile of the pump beam at  $z = 0$ , and  $x_s$  and  $x_i$  are transverse coordinates in the lab frame. The one-photon propagators  $h(x_s, x; \omega_s) = 1/(i\lambda L_s)^2 \exp(ik_s L_s)$  and  $h(x_i, x; \omega_i) = 1/(i\lambda L_i)^2 \exp(ik_i L_i)$  describe the propagation of the signal and idler photon from the crystal to the detection plane. They contain the wavevector amplitudes  $k_{s,i} = \omega_{s,i}/c$  and the path lengths  $L_{s,i}$ . We will consider almost frequency-degenerate SPDC, where the frequency difference  $\Delta\omega \equiv \omega_s - \omega_i$  and where the sum  $\omega_s + \omega_i = \omega_p = ck_p$  is fixed by the quasi-monochromatic pump.

Next we introduce “beam coordinates”  $\delta x_s$  and  $\delta x_i$  that are defined with respect to the two beam axes in the signal and idler direction, which themselves are oriented at angles  $-\Theta$  and  $\Theta$  with respect to the pump laser (see Fig. 8.1). Beam coordinates are more convenient to evaluate the effect of beam reflections and translations and have the extra advantage that the coordinates  $\delta x_{s,i}$  remain relatively small. Substitution of  $\delta x_{s,i}$  for  $x_{s,i}$  in Eq. (8.1) immediately yields the generated two-photon wave function in beam coordinates. Working in the paraxial limit, we expand the path lengths as  $L_{s,i} \approx L + |\delta x_{s,i} - x|^2/2L \pm x\Theta$ . The term  $\pm x\Theta$  describes how a displacement at the crystal leads to a change of the signal/idler path on account of the viewing angle.

By comparing the combined propagator of the two-photon field with the one-photon propagator of the pump field to a detection plane at a distance  $L$  behind the crystal, we can solve the integration in Eq. (8.1) to obtain the relatively complicated expression

$$\begin{aligned} \psi(\delta x_s, \delta x_i; \Delta\omega) &\approx E_{p,z} \left( \frac{1}{2}(\delta x_s + \delta x_i) - \gamma \right) \times \\ &\exp \left[ \frac{ik_p}{8L} \left( |\delta x_s - \delta x_i|^2 + 4\gamma(\delta x_s + \delta x_i) - 4\gamma^2 \right) \right], \end{aligned} \quad (8.2)$$

where  $E_{p,z}$  is the pump profile *in the detection plane* [31] and  $\gamma = L\Theta\Delta\omega/\omega_p$  is a transverse displacement that appears only for  $\Delta\omega \neq 0$ . The approximation is almost perfect and only refers to the removal of a small phase term ( $\ll 1$ ) of the order of  $(\Delta\omega/\omega_p)^2$  times the Fresnel number  $N_F$  of the detected system.

Equation (8.2) gives a full description of the spatial and temporal coherence of the generated two-photon field in the considered thin-crystal limit. It shows among others that this field has a completely different spatial coherence in the sum coordinate  $\delta x_s + \delta x_i$  than in the difference coordinate  $\delta x_s - \delta x_i$ . Whereas the former is dictated by the profile of the pump laser, the latter is characterized by the field curvature of a point source. This difference is of vital importance in the rest of our discussion and causes the very different behavior of two-photon interferometers with an even or odd number of reflecting mirrors (see Sec. 8.2.3).

If the detection bandwidth is too large to satisfy the quasi-monochromatic limit, we should include the effects of  $\gamma \neq 0$  in our discussion of Eq. (8.2). These effects are discussed in Sec. 8.2.4. For the moment we will simply explain their origin. The extra phase terms originate from the comparison of the  $[\exp(ikL)$  terms in the] propagators of signal, idler and pump beams. The argument of the pump profile  $E_{p,z}$  depends on  $\Delta\omega$ , because this argument can also be written as the weighted sum  $(k_s x_s + k_i x_i)/k_p$  of the signal and idler positions  $x_s$

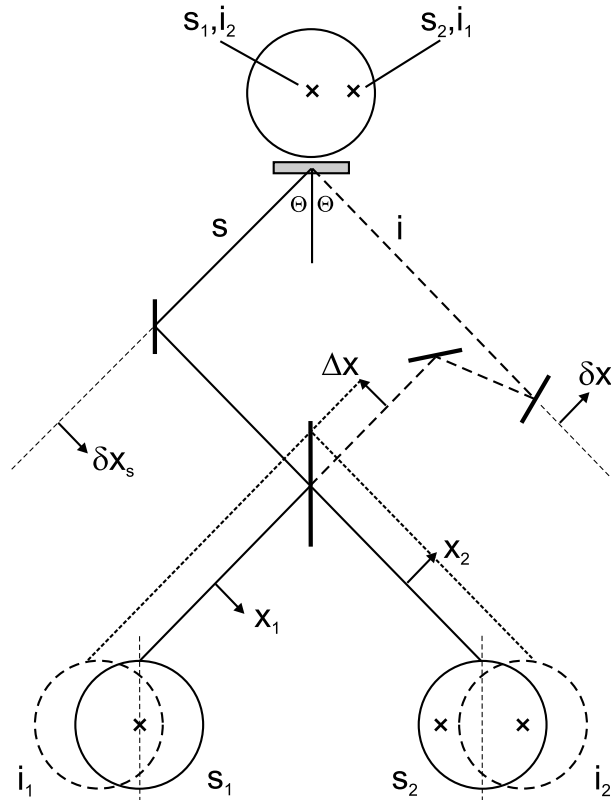


**Figure 8.1:** Optical-path geometry of a HOM interferometer with one mirror in the signal beam and two mirrors in the idler beam, which also contains a displacement  $\Delta x$ . The five circles denote the pump spot and four possible images thereof. These are used to explain the occurrence of spatial labeling (see Sec. 8.3.3 for details).

and  $x_i$  in the lab frame [31]. In the non-monochromatic limit, the spatial and spectral degrees of freedom become mixed, basically because the transverse momenta of the signal and idler photon depend both on their emission angle ( $\approx \mp\Theta$ ) and photon frequency  $\omega$ .

### 8.2.2 Two-photon interference

In a standard (HOM) two-photon interferometer the signal and idler beam are combined on a beamsplitter of which the two output beams are filtered spectrally and spatially, before being detected by two photon detectors. The observed two-photon interference is most easily described in the beam coordinates  $x_1$  and  $x_2$  of the two local coordinate systems that are centered around the two axes at detectors 1 and 2, respectively. We thus need to express the detected two-photon field  $\psi_{\text{det}}(x_1, x_2; \Delta\omega_{12})$  (with  $\Delta\omega_{12} = \omega_1 - \omega_2$ ) in terms of the generated field. As coincidence counts in a HOM interferometer can be generated by two possible routes, being either a reflection of both signal and idler photon at the beamsplitter or a double

transmission, we can symbolically express the detected two-photon field as

$$\psi_{\text{det}}(x_1, x_2; \Delta\omega_{12}) = -R\psi_{rr}(\dots) + T\psi_{tt}(\dots), \quad (8.3)$$

where the intensity reflection  $R$  and transmission  $T$  are equal to  $\frac{1}{2}$  only for the ideal beam-splitter. The coordinates in the two-photon fields  $\psi_{rr}$  and  $\psi_{tt}$  are left out on purpose. One reason for this is that the transformation from detector to crystal coordinates is different for the two possible routes. Another reason is that the actual transformation also depends on the number of mirrors and on the time delay  $\Delta t = \Delta L/c$  and transverse displacement  $\Delta x$  imposed in one of the interferometer arms.

The coincidence count rate  $R_c$  observed behind spatial apertures and spectral filters is found by integrating  $|\psi_{\text{det}}(\dots)|^2$  over the corresponding spatial and spectral coordinates, as

$$R_c = \int d\omega_1 d\omega_2 dx_1 dx_2 |\psi_{\text{det}}(x_1, x_2; \Delta\omega_{12})|^2. \quad (8.4)$$

The interference between the two-photon fields  $\psi_{rr}$  and  $\psi_{tt}$  is contained in the cross-terms of  $|\psi_{\text{det}}|^2$ . This interference is only present close to zero delay and perfect spatial overlap, but disappears when either  $\Delta t$  or  $\Delta x$  are sufficiently large. In general we can thus write the coincidence count as

$$R_c(\Delta t, \Delta x) = R_{c,\infty} \left( 1 - \frac{2RT}{R^2 + T^2} V_{\text{HOM}}(\Delta t, \Delta x) \right). \quad (8.5)$$

In the rest of the discussion we will concentrate on the temporal and spatial dependence of the visibility function  $V_{\text{HOM}}(\Delta t, \Delta x)$ , which contains the interesting physics. The factor  $V_{\text{RT}} = 2RT/(R^2 + T^2)$  just specifies the ‘‘intensity unbalance’’ between the two probability channels. The visibility function

$$V_{\text{HOM}} \approx \frac{\text{Re} [2\langle \psi_{rr} | \psi_{tt} \rangle]}{\langle \psi_{rr} | \psi_{rr} \rangle + \langle \psi_{tt} | \psi_{tt} \rangle}, \quad (8.6)$$

basically measured the spectral overlap between the two-photon fields  $\psi_{rr}$  and  $\psi_{tt}$ , where we have used the shorthand notation  $\langle \dots \rangle = \int d\omega_1 d\omega_2 dx_1 dx_2$ . Alternative, one could say that  $V_{\text{HOM}}$  measured the overlap between one two-photon field ( $\psi_{rr}$ ) and a modified version thereof ( $\psi_{tt}$ ), and can thereby provide information on the spatial and/or temporal coherence of this field. The physical interpretation of the visibility function  $V_{\text{HOM}}$  is that it quantifies the amount of temporal and/or spatial labeling of the two photons. If any properties of the detected photons 1 and 2 allow one to decide which photon took the signal path and which photon took the idler path, this so-called labeling will remove the interference between the two probability channels.

### 8.2.3 Why the number of mirrors matters

In this subsection we will highlight the difference between two-photon interferometers with an even or odd number of reflecting mirrors in the combined signal and idler path by presenting detailed expressions of  $V(\Delta t, \Delta x)$  for both cases. Based on these general expressions, Secs. 8.2.4 and 8.2.5 will separately treat the occurrence of temporal labeling ( $V_{\text{HOM}}(\Delta t)$ ) at

$\Delta x = 0$ ) and spatial labeling [ $V_{\text{HOM}}(\Delta x)$  at  $\Delta t = 0$ ], again using the distinction between an even and odd number of reflections.

Figure 8.1 depicts a possible HOM interferometer, which in this case has one mirror in the signal path and two mirrors in the idler path and thus falls in the “odd” category. It is also a sketch of the experiment, where we use 1 + 4 mirrors. The idler path contains an adjustable transverse displacement  $\Delta x$  (as shown) and an additional longitudinal displacement  $\Delta L = c\Delta t$  (shown only in the experimental setup of Fig. 8.2). The beams are labeled such that the doubly-reflected path links the coordinate indices ( $s \leftrightarrow 1$ ) and ( $i \leftrightarrow 2$ ), making  $\Delta\omega = \Delta\omega_{12}$ , whereas the doubly-transmitted path links ( $s \leftrightarrow 2$ ) and ( $i \leftrightarrow 1$ ), making  $\Delta\omega = -\Delta\omega_{12}$ . The crucial point to note, and the whole reason for the “odd/even” distinction, is that every additional reflection in either signal or idler path leads to an inversion of the corresponding beam coordinate  $\delta x \leftrightarrow -\delta x$ .

We will first consider an interferometer with one mirror in the signal and one mirror in the idler path, i.e., with an even number of mirrors. For this balanced interferometer the relation between the detected and generated two-photon field (Eq. 8.3) is

$$\begin{aligned} \psi_{\text{even}}(x_1, x_2; \Delta\omega_{12}) &= -R\psi(x_1, x_2 + \Delta x; \Delta\omega_{12})e^{i\omega_2\Delta t} \\ &\quad + T\psi(-x_2, -x_1 + \Delta x; -\Delta\omega_{12})e^{i\omega_1\Delta t}, \end{aligned} \quad (8.7)$$

where the longitudinal delay  $\Delta t$  and transverse displacement  $\Delta x$  are both imposed on the idler beam. Note that the arguments in the two contributions  $\psi_{rr}$  and  $\psi_{ii}$  are related through a swap of the labels  $1 \leftrightarrow 2$  in combination with an inversion  $x_j \leftrightarrow -x_j$  (for  $j = 1, 2$ ). Substitution into Eq. (8.2) shows that the two contributions have the dominant part of the exponential factor in common, as  $\delta x_s - \delta x_i = x_1 - x_2 - \Delta x$  for both terms, but differ in the argument in the pump field. For this “even” geometry, the visibility function  $V_{\text{HOM}}$  thus becomes

$$V_{\text{even}}(\Delta t, \Delta x) \approx \frac{\text{Re} \left[ 2 \int e^{i\Delta\omega_{12}\Delta t} e^{(ik_p/L)\gamma_{12}\Delta x} E_{p,z}^* \left( -\alpha + \frac{1}{2}\Delta x \right) E_{p,z} \left( \alpha + \frac{1}{2}\Delta x \right) \right]}{\int \left| E_{p,z} \left( -\alpha + \frac{1}{2}\Delta x \right) \right|^2 + \left| E_{p,z} \left( \alpha + \frac{1}{2}\Delta x \right) \right|^2}, \quad (8.8)$$

where the integration runs over  $x_1, x_2, \omega_1$  and  $\omega_2$  and where we have introduced  $\alpha = -\frac{1}{2}(x_1 + x_2) + \gamma_{12}$  as help variable, with  $\gamma_{12} = L\Theta\Delta\omega_{12}/\omega_p$ . The sensitivity of  $V_{\text{even}}$  to a transverse displacement  $\Delta x$  is thus found to be determined mainly by the shape of the pump beam, in combination with the limitations set by the finite integration range over the detection apertures. Especially the symmetry of the pump beam under reflection in the  $yz$  plane plays a crucial role. If this beam is symmetric under reflection, the two-photon interference will result in the familiar HOM dip ( $V_{\text{HOM}} > 0$ ), if this beam is anti-symmetric a HOM peak ( $V_{\text{HOM}} < 0$ ) will result instead [89].

The above result applies to any geometry where the total number of mirrors in the signal and idler beam is even. Officially, one should still distinguish two subclasses, but these give basically the same result. If both signal and idler beam contain an odd number of mirrors we obtain expressions identical to the ones found above for the case of “1+1 mirror”. If both

signal and idler beam contain an even number of mirrors all positions  $x_j$  should be inverted, but  $V_{\text{even}}$  is again described by Eq. 8.8 with a new  $\alpha = -\frac{1}{2}(x_1 + x_2) - \gamma_{12}$ .

Next we consider the interferometer of Fig. 8.1, which contains one mirror in the signal path and two mirrors in the idler path, and thus falls in the ‘‘odd’’ category. For this unbalanced interferometer, the relation between the detected and generated two-photon field (Eq. 8.3) is

$$\begin{aligned} \psi_{\text{odd}}(x_1, x_2; \Delta\omega_{12}) = & -R\psi(x_1, -x_2 - \Delta x; \Delta\omega_{12})e^{i\omega_2\Delta t} \\ & + T\psi(-x_2, x_1 - \Delta x; -\Delta\omega_{12})e^{i\omega_1\Delta t}, \end{aligned} \quad (8.9)$$

which differs from Eq. (8.7) only by a sign in the idler coordinate  $\delta x_i$ . Substitution into Eq. (8.2) shows that the two terms now have slightly different exponential factors, but almost identical arguments in the pump field, as the combination  $\delta x_s + \delta x_i$  is the same for both  $\psi_r$  and  $\psi_t$ . For this ‘‘odd’’ geometry, the visibility function  $V_{\text{HOM}}$  is

$$V_{\text{odd}}(\Delta t, \Delta x) \approx \frac{\text{Re} \left[ 2 \int e^{i\Delta\omega_{12}\Delta t} e^{-(i2k_p/L)\gamma_{12}\beta} e^{-(ik_p/2L)(x_1+x_2)\Delta x} E_{p,z}^*(\beta - \gamma_{12}) E_{p,z}(\beta + \gamma_{12}) \right]}{\int |E_{p,z}(\beta - \gamma_{12})|^2 + |E_{p,z}(\beta + \gamma_{12})|^2}, \quad (8.10)$$

where the integration again runs over  $x_1, x_2, \omega_1$  and  $\omega_2$  and where we have now introduced  $\beta = \frac{1}{2}(x_1 - x_2 - \Delta x)$  as help variable. The sensitivity of  $V_{\text{odd}}$  to a transverse displacement  $\Delta x$  is mainly determined by the exponential factor in Eq. (8.2), again in combination with the limitations set by the finite integration range over the detection apertures and pump profile. The ‘‘odd’’ geometry thereby probes the two-photon coherence in the difference coordinate  $\delta x_s - \delta x_i$ , whereas the ‘‘even’’ geometry probed its coherence in the sum coordinate  $\delta x_s + \delta x_i$ . The above result again applies to all geometries with an odd number of mirrors in the combined signal and idler paths; Eqs. (8.9) and (8.10) remain basically the same, apart some trivial minus signs and a possible redefinition of  $\beta$ .

## 8.2.4 Temporal labeling

In this section we will discuss the temporal labeling in a HOM interferometer with perfectly aligned beams ( $\Delta x = 0$ ), but unbalanced arm lengths ( $\Delta t \neq 0$ ). The calculated  $V_{\text{HOM}}(\Delta t)$  is different for the two generic cases, where the total number of mirrors is either even or odd. Whereas the even case exhibits only temporal labeling, the odd geometry also exhibits a combined temporal and spatial labeling, which can reduce  $V_{\text{HOM}}$  even further.

We will start by analyzing the even case for a symmetric pump ( $E_{p,z}(x) = E_{p,z}(-x)$ ). Substitution of  $\Delta x = 0$  in Eq. (8.8) and removal of the spatial integration (under the assumption that the shift  $\gamma_{12}$  doesn’t affect this integration in any serious way) yields

$$V_{\text{even}}(\Delta t) = \frac{\text{Re} \left[ \int d\omega_1 e^{i(2\omega_1 - \omega_p)\Delta t} T_1(\omega_1) T_2(\omega_p - \omega_1) \right]}{\int d\omega_1 T_1(\omega_1) T_2(\omega_p - \omega_1)}, \quad (8.11)$$

where  $T_1$  and  $T_2$  are the intensity transmission spectra of filters located in front of the detectors 1 and 2, respectively. We thus obtain the well-known result that the HOM dip has the same shape, but is twice as narrow, as the Fourier transform of the product  $T_1(\omega_1)T_2(\omega_p - \omega_1)$  [88]. For identical filters with a sharp block-shaped transmission spectrum of width  $\Delta\omega_f$  centered around  $\frac{1}{2}\omega_p$ , Eq. (8.11) yields

$$V_{\text{even}}(\Delta t) = \frac{\sin(\Delta\omega_f \Delta t)}{\Delta\omega_f \Delta t}. \quad (8.12)$$

The full width at half maximum (FWHM) of this visibility function is  $1.21 \times \pi/\Delta\omega_f = 1.21 \times \lambda^2/(2c\Delta\lambda_f)$ . If the transmission spectra of the filters are not properly centered, the product  $T_1 T_2$  will sharpen up and the temporal coherence of the detected two-photon field will increase.

If the combined number of mirrors in the signal and idler path is odd, we should substitute  $\Delta x = 0$  in Eq. (8.10) instead of Eq. (8.8). It is now in general not possible to separate the spatial and spectral integration, because the displacement  $\gamma_{12} \propto \Delta\omega_{12}$  appears both in the argument of  $E_{p,z}$  and in the exponential factor  $\exp[-(i2k_p/L)\gamma_{12}\beta]$ . Separation is only possible in two cases: if either the detection apertures are small enough to sufficiently limit the integration range over  $\beta$ , or if the displacement  $\gamma_{12}$  is sufficiently small, we retain the result we had for the even case [Eq. (8.12)].

We will first discuss the physical origin of this combined labeling, before quantifying what we mean with ‘‘sufficiently small’’. In general, the visibility  $V(\Delta t)$  decreases when the time difference between the photons arriving at detector 1 and 2 allows one (even only in principle) to distinguish which photon took the signal path and which one took the idler path. The important point to note is that this time difference is only equal to the set value  $\Delta t = \Delta L/c$  for photon pairs that originate from the center of the pumped region. Photon pairs that originate from the outer parts of the pumped region can experience an additional temporal delay of typically  $\Delta t_{\text{extra}} = \pm 2\Theta w_p/c$  between their signal and idler photon, for a Gaussian pump beam of waist  $w_p$ . This delay alone doesn’t reduce the visibility, as the contributions on either side of the pumped area can compensate each other, and actually do so for the even case. For the odd case, this extra term can lead to a degradation of the visibility, but only if the integration in Eq. (8.10) is large enough, i.e., if the apertures are opened wide enough in comparison to the pump divergence. The degradation will be small only if  $\Delta\omega_f t_{\text{extra}} \ll \pi$ . This criterium roughly translates into  $\Delta\omega_f/\omega_p \ll \theta_p/\Theta$ ,  $\theta_p$  being the far-field opening angle of the pump laser.

From an experimental perspective, the extra term in  $V_{\text{odd}}$  makes two-photon interferometers with an odd number of mirrors more difficult to operate than interferometers with an even number of mirrors. In practice, great care has to be taken to avoid the mentioned additional labeling. A two-photon interferometer with an odd number of mirrors will only provide a good visibility for apertures much larger than the pump size if three conditions are satisfied: (i) the spectral filters should be narrow enough, (ii) the opening angle  $\Theta$  should be small enough, and (iii) the pumped region should be compact enough. Together these three conditions translate into the requirement that the dimensionless ratio of the detection bandwidth over the pump frequency should be much smaller than the ratio of the pump divergence over the opening angle, i.e.,  $\Delta\omega_f/\omega_p \ll \theta_p/\Theta$ . If this is not the case, the combined spatial and spectral labeling will lead to a reduction of  $V_{\text{odd}}(\Delta t = 0)$  and a widening of the  $V_{\text{odd}}(\Delta t)$

profile as compared to Eq. (8.12). The precise amount of which depends mainly on the dimensionless product  $(\Delta\omega_f/\omega_p)(\Theta/\theta_p)$  and to a lesser extent on the position of the detectors in relation to the near/far field of the pump.

### 8.2.5 Spatial labeling

Next we will discuss spatial labeling in a HOM interferometer with balanced arms ( $\Delta t = 0$ ) and sufficiently narrow spectral filters to validate the quasi-monochromatic ( $\Delta\omega = 0$ ) limit. We again distinguish between interferometers with an even and odd number of mirrors.

For the “even” case, Eq. (8.8) can be easily solved if the integration range over  $x_1$  and  $x_2$  is large enough to change it into an effective integration of  $x_1 + x_2$  and  $x_1 - x_2$  over  $[-\infty, \infty]$ . The integration simplifies even further when one realizes that the overlap  $\langle \psi | \phi \rangle$  between two wave functions  $|\psi\rangle$  and  $|\phi\rangle$  does not change upon propagation, due to the unitary character of the propagator  $h(x, x')$ . The visibility  $V_{\text{even}}(\Delta x)$  is thereby found to be a direct measure for the overlap of the pump profile with a displaced version thereof. If this pump profile is a fundamental Gaussian function with beam waist  $w_p$ , we obtain the simple result

$$V_{\text{even}}(\Delta x) = \exp\left(-\frac{1}{2}\Delta x^2/w_p^2\right). \quad (8.13)$$

For the “odd” case, we have to substitute  $\Delta t = 0$  and  $\Delta\omega = 0$  in Eq. (8.10) instead of Eq. (8.8) to obtain

$$V_{\text{odd}}(\Delta x) \approx \frac{\text{Re} \left[ \int \int dx_1 dx_2 \left| E_{p,z} \left( \frac{1}{2}(x_1 - x_2 + \Delta x) \right) \right|^2 \exp \left( \frac{ik_p}{2L}(x_1 + x_2)\Delta x \right) \right]}{\int \int dx_1 dx_2 \left| E_{p,z} \left( \frac{1}{2}(x_1 - x_2 + \Delta x) \right) \right|^2} \quad (8.14)$$

If the aperture diameters are much larger than the size of the pump beam in the detection plane, we can again rewrite the integrations over  $x_1$  and  $x_2$  into integrations over  $x_1 + x_2$  and  $x_1 - x_2$  and use  $x_1 \approx x_2$  as the outcome of the latter integration to obtain

$$\begin{aligned} V_{\text{odd}}(\Delta x) &\approx \frac{\text{Re} \left[ \int dx_1 dy_1 \exp \left( \frac{ik_p}{L}x_1\Delta x \right) \right]}{\int dx_1 dy_1} \\ &\approx \frac{2J_1(\pi d\Delta x/(\lambda_p L))}{\pi d\Delta x/(\lambda_p L)}. \end{aligned} \quad (8.15)$$

In the final step, we have expressed the integration over a circular aperture with diameter  $d$  in terms of the first-order Bessel function  $J_1$ . We define the typical transverse coherence length  $\Delta x_{\text{coh}}$  as the full width at half maximum (FWHM) of  $V_{\text{odd}}(\Delta x)$ , which is 1.16 times the peak-to-zero width of  $\Delta x = 1.22L(\lambda_p/d)$ . The sensitivity of a two-photon interferometer with an odd number of mirrors to transverse displacement is thus found to be determined solely

by the size of the detecting apertures. More specifically,  $V_{\text{odd}}(\Delta x)$  has the same shape, but is just twice as narrow, as the diffraction limit at the crystal found for a uniform but focused illumination of one of the detecting apertures with the detected wavelength  $2\lambda_p$ .

To arrive at Eq. (8.15) we had to assume that the aperture sizes were large as compared to the size of the pump beam. If only one of the two apertures satisfies this criterium, we can still conveniently replace the integrations over  $x_1$  and  $x_2$  by integrations over  $x_1 + x_2$  and  $x_1 - x_2$  and solve the latter. For this case of asymmetric aperture sizes, the resulting Eq. (8.15) thus remains valid. If the apertures have equal sizes, but are not very large as compared to the size of the pump beam, the aperture diameter in Eq. (8.15) should roughly be reduced from its physical size  $d$  to an effective size  $d_{\text{eff}} \approx d - w$  to account for the reduced detection efficiency of photon pairs that fall close to the edge of either aperture. Here,  $w$  is the size of the pump beam in the detection plane and thereby half the positional spread in one photon for a fixed position of the other photon.

## 8.3 Experimental results

### 8.3.1 Experimental setup

Our experimental setup, representing a two-photon (Hong-Ou-Mandel type) interferometer, is shown in Figure 8.2. A cw krypton ion laser operates at a wavelength of 407 nm and emits 70 mW in a pure TEM<sub>00</sub> mode. This light is mildly focused (measured opening angle typically  $\theta_p \approx 0.50$  mrad and waist  $w_p \approx 260$   $\mu\text{m}$ ) on a 1-mm-thick type-I BBO crystal (cutting angle 29.2°). The crystal is tilted such that the emitted SPDC cone extends over a full opening angle of  $2 \times 1.6^\circ$  around the pump direction. Two entangled beams  $s$  and  $i$  (signal and idler), selected from this light cone by apertures behind a broadband beamsplitter at 1.20 m from the crystal, serve as input channels of the beamsplitter. In one of the two input beams, a reflecting open prism is placed on top of two perpendicularly mounted translation stages to enable accurate control of both the path-length difference  $\Delta L$  and the transverse beam displacement  $\Delta x$ , using motorized actuators. In most of the experiments, the output beams of the beamsplitter are focused onto free-space single photon counters (Perkin Elmer SPCM-AQR-14) by  $f = 6$  cm lenses located at 1.50 m from the crystal. We note that these counters still operate as good buckets under typical transverse beam displacements of  $\Delta x = 1$  mm in our experiments as the demagnified displacement at the detector is then still only  $6/150 \times \Delta x = 40$   $\mu\text{m}$  whereas the active area of the detector is typically 200  $\mu\text{m}$  in diameter. Though omitted in Fig. 8.2 for simplicity, our scheme allows an easy switch between free-space and fiber-coupled counters (Perkin Elmer SPCM-AQR-14-FC), connected to single-mode fibers (NA = 0.12) and 10x objectives. Bandwidth selection is done by interference filters (10 nm FWHM) in combination with red filters (Melles Griot RG715). An electronic circuit records coincidence counts within a time window of 1.76 ns.

In order to achieve the precise temporal alignment that a HOM interferometer requires, i.e., simultaneous arrival of entangled pair-photons at the beamsplitter, we use a similar trick as presented in [93]. We employ a flip-mirror to inject light from a diode laser (visible wavelength  $\approx 640$  nm) into the setup, such that its emitted light virtually covers both signal and idler paths (see Fig. 8.2). By tuning this laser below threshold, where it acts as a bright

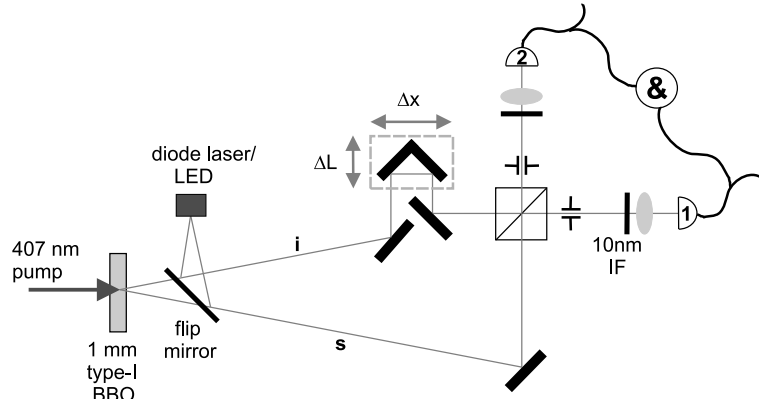


**Figure 8.2:** Schematic view of the experimental setup (see text for details).

LED with a limited coherence length, the path-length difference can be set to within a few  $\mu\text{m}$ . Final fine-tuning of the path-length difference and the angular alignment between the two beams (within a few  $\mu\text{rad}$ ) is done by motorized actuators (Newport LTA-HL; submicron stepsizes) attached to both translation stages and beamsplitter.

In our main experiments, we measure the coincidence count rate as a function of the time delay  $\Delta t = \Delta L/c$  and relative beam displacement  $\Delta x$  between the signal and idler beam, in order to quantify the two-photon temporal and spatial coherence, respectively. We have employed both an even and an odd number of mirrors to demonstrate the essential role of the mirror number in two-photon HOM interference. Most of our measurements are however done with the odd configuration (see Fig. 8.2) as this is the most unexplored case. Furthermore, we have applied free-space detection behind both 4 mm and 14 mm apertures, corresponding to detection angles of  $\theta_{\text{det}} = 1.7$  mrad and  $\theta_{\text{det}} = 5.8$  mrad, respectively. These values are well within the angular width of the SPDC ring of  $\theta_{\text{SPDC}} = 18$  mrad that we calculate and observe for our (type-I) geometry. In addition, we use spectral filters with bandwidths that are much narrower than the generated SPDC bandwidth ( $> 50$  nm). These two conditions ensure operation in the thin-crystal limit.

### 8.3.2 Temporal labeling

In Figure 8.3(a) the measured coincidence count rate behind 14 mm apertures is plotted versus time delay  $\Delta t$ . Fitting the data points with Eq. (8.12) yields a full width at half maximum (FWHM) of  $133 \pm 2$  fs. For 4 mm apertures we obtain the same value. These values agree very well with the theoretical coherence time of 133 fs, calculated for a block-shaped transmission filter with a measured spectral bandwidth of  $\Delta\lambda = 10$  nm centered around  $\lambda = 814$  nm. The observed sidelobe structure is Fourier-related to the spectral cut-off produced by the sharp-edged interference filters. Slight deviations between data points and fits are attributed to the non-perfect block-shape of the filter transmission function.

The quality of the two-photon interference can be quantified by the measured peak visibilities, being  $V = 85.0 \pm 0.5\%$  and  $V = 81.0 \pm 0.5\%$  for 4 mm and 14 mm apertures, respectively. For fiber-coupled detection, we measure a much higher visibility of  $V = 94.0 \pm 0.5\%$ .

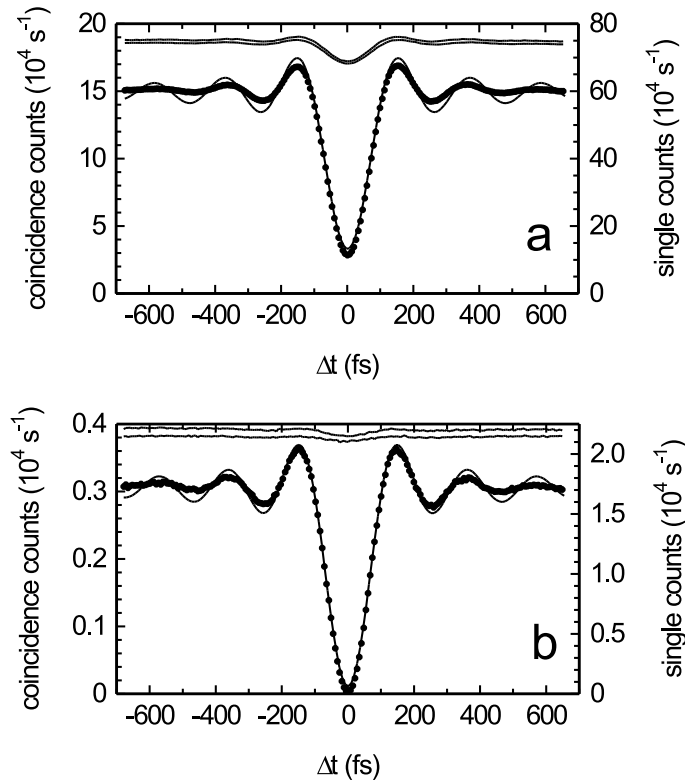


**Figure 8.3:** Two-photon temporal coherence, measured as the coincidence count rate (dots) versus time delay  $\Delta t$ , for (a) free-space detection behind 14 mm apertures and (b) fiber-coupled detection. Sinc-shaped fits and the measured single count rates (solid curves; righthand scale) are plotted as well.

This value is very close to the theoretical limit of  $V_{RT} = 95\%$  of our beamsplitter, having a measured  $T/R$ -ratio of 58/42. Fig. 8.3b shows the temporal coherence measured with fiber-coupled detectors scheme but now with a better high-quality 50/50 laserline beamsplitter. We again obtain a FWHM of  $133 \pm 2$  fs, but the peak visibility is considerably higher at  $V = 99.3 \pm 0.2\%$ . The lower peak visibilities obtained with free-space detection is attributed to the spatial labeling observed by the bucket detectors (see Figs. 8.5 and 8.6).

Apart from the coincidence dips, Fig. 8.3 also shows prominent dips in the measured *single* count rates. The occurrence of a ‘single dip’ has first been reported by Resch *et al.* [94]. This extra dip occurs as a result of the limitation of a photodetector to record two simultaneously arriving pair-photons as two single clicks. As these arrivals are more numerous for a balanced HOM interferometer than for an unbalanced one, a dip will show up in the measured single count rate as well.

In Fig. 8.4 we highlight the single dip that we measured behind 14 mm apertures [data copied from Fig. 8.3(a)]. This data is of much higher quality than the one presented in Ref. [94]; though sampling only 10 s for each data point, we obtain a statistical error of

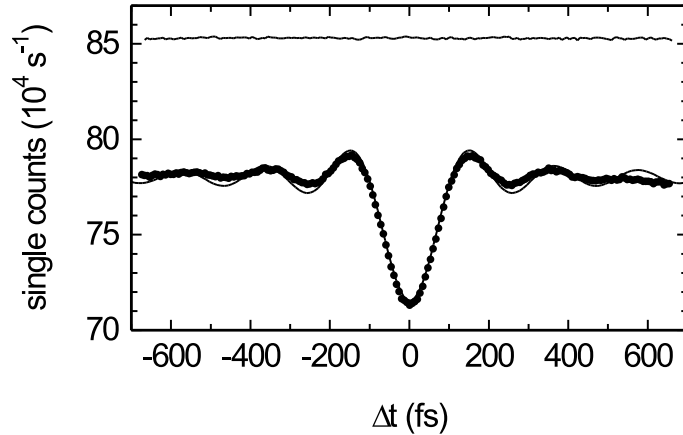


**Figure 8.4:** Single count rate measured in a HOM experiment (dots) with sinc-shaped fit [detail of Fig. 8.3(a)]. The solid curve shows the sum of the single count rates measured when either the signal or the idler path is blocked. All displayed count rates are corrected for 50 ns deadtime of the detector.

$<0.1\%$  that is even too small to display. This allows us to observe the clear sinc-shaped profile identical to the coincidence dip with a FWHM of  $133 \pm 2$  fs. Based on measured rates of  $7.13 \times 10^5 \text{ s}^{-1}$  and  $7.81 \times 10^5 \text{ s}^{-1}$  at zero and infinite delay, respectively, we determine a dip visibility of  $V_{\text{sc}} \approx 9\%$ . A calculation from  $V_{\text{sc}} = V\eta/(4 - \eta)$  [94] yields the same value, thereby using  $V = 81\%$  and an overall detection efficiency of  $\eta = 0.40$ , as deduced from the measured quantum efficiency (=coincidences/singles ratio) of  $\eta_{\text{q}} = 0.20$ . All count rates shown in Fig. 8.4 have been multiplied by a factor of  $1/(1 - \tau_{\text{d}}R_{\text{det}}) \approx 1.04$  to correct for the detector deadtime of  $\tau_{\text{d}} = 50$  ns and compare with the calculation mentioned above.

To further illustrate the origin of the single dip, we have also plotted the sum of the measured single count rates in absence of HOM interference as the solid curve in Fig. 8.4. This rate of  $8.54 \times 10^5 \text{ s}^{-1}$  shows no dip as it is obtained by adding the individual signal and idler rates of  $5.00 \times 10^5 \text{ s}^{-1}$  and  $3.54 \times 10^5 \text{ s}^{-1}$ , where the rate imbalance is due to the beamsplitter ratio  $T/R = 58/42$ . We thus measure a single count rate reduction of 16.5% for the balanced interferometer ( $\Delta t = 0$ ), but also obtain an 8.5% reduction *in absence* of HOM interference ( $\Delta t = \infty$ ). This latter reduction of course results from a random 1/4 probability that both photons arrive at the detector under study. At a finite detection efficiency  $\eta$  we expect the single count rate to be reduced by a factor  $(1 - \eta/4)$  and  $(1 - \eta/4(1+V))$  in an interferometer off and on resonance, as compared to the sum of the individual rates. For our conditions of  $V = 81\%$  and  $\eta = 0.40$ , we expect reductions of  $(1 + V)\eta/4 = 18\%$  and  $\eta/4 = 10\%$  for the balanced and unbalanced interferometer, respectively, which agree reasonably well with the measured values.

As an aside we note that our count rates are large enough to experience some visibility reduction through the influence of double photon pairs. We estimate this reduction to be  $\Delta V = 8R_{\text{c}}\tau_{\text{cc}}(1/\eta^2 - 1/2\eta)$ , based on a *generated* pair rate  $R = 2R_{\text{c}}/\eta^2$  and a coincidence time window  $\tau_{\text{cc}}$ . Our measured visibility of  $V = 78\%$  for 17 mm apertures is expected to suffer from a reduction of only  $\Delta V \approx 1\%$ , based on a measured coincidence rate of  $R_{\text{c}} =$

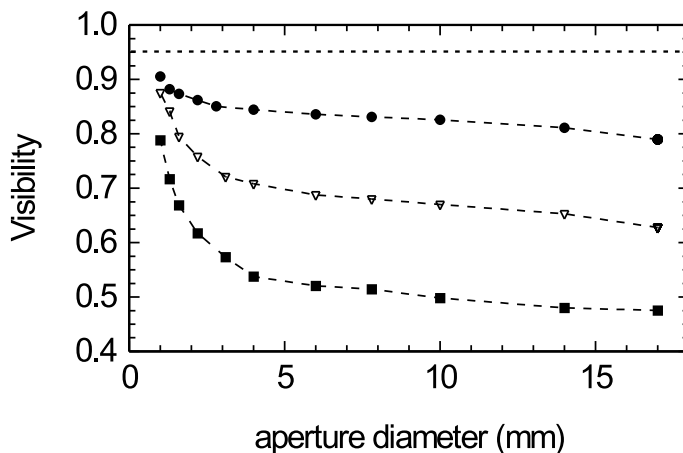


**Figure 8.5:** Measured peak visibility  $V_{\text{odd}}$  versus aperture diameter (at 1.2 m from crystal) for  $\Delta\lambda = 10$  nm interference filters and three different pump sizes:  $w_p = 260 \mu\text{m}$  (dots),  $w_p = 400 \mu\text{m}$  (triangles) and  $w_p = 700 \mu\text{m}$  (squares). The dashed horizontal line at  $V = 95\%$  indicates the visibility limit set by the beamsplitter  $T/R$  ratio of 58/42.

$2.0 \times 10^5 \text{ s}^{-1}$  and  $\eta = 0.40$ . To check that higher coincidence rates lead to larger reductions, we have also used a 4 mm crystal. At a measured rate of  $R_c = 8 \times 10^5 \text{ s}^{-1}$  we measure a lower visibility of  $V = 73\%$ , which is indeed compatible with the expected reduction of  $\Delta V \approx 5\%$ .

The theory in Sec. 8.2.4 predicts that the peak visibility in a HOM interferometer with an odd number of mirrors can be limited by a combined temporal and spatial labeling that depends on three different parameters: the aperture size, the pump size at the crystal and the detected spectral bandwidth. The first two limitations are demonstrated in Fig. 8.5, which shows the measured visibility as a function of the aperture diameter for three pump sizes  $w_p$ , using a  $\Delta\lambda = 10$  nm interference filter. The largest pump spots yield the lowest visibilities, as expected. Note how the visibilities increase steeply for the smallest apertures where diffraction removes the spatial labeling.

An increase of the pump spot not only leads to a reduction of the peak visibility but also to a widening of the  $V_{\text{HOM}}(\Delta t)$  curve. At an aperture size of 14 mm we measure (FWHM) coherence times of 133 fs for  $w_p = 260 \mu\text{m}$ , 147 fs for  $w_p = 400 \mu\text{m}$ , and 180 fs for  $w_p = 700 \mu\text{m}$ , all at  $\Delta\lambda = 10$  nm. For these three geometries the dimensionless quantity  $(\Delta\omega_f/\omega_p)(\Theta/\theta_p)$  that quantifies the extra labeling increases from 0.34 to 0.49 and 0.86.

The limitation of the visibility by the detected spectral bandwidth is shown in Fig. 8.6, where the measured visibility is plotted versus aperture size for both  $\Delta\lambda = 5$  nm and 10 nm interference filters, and a pump waist of  $w_p = 260 \mu\text{m}$ . The narrower filters yield higher visibilities. All observations made in relation to Figs. 8.5 and 8.6 are compatible with the prediction made in Sec. 8.2.4 on combined temporal and spatial labeling. For an *even* number of mirrors in our interferometer (with one extra mirror in signal path; see below) we have observed none of these combined-labeling effects, again in agreement with Sec. 8.2.4.

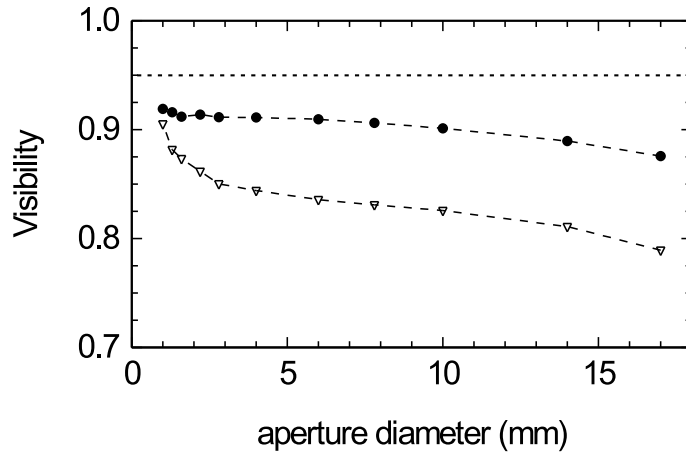


**Figure 8.6:** Measured peak visibility  $V_{\text{odd}}$  versus aperture diameter for  $\Delta\lambda = 5$  nm (solid dots) and  $\Delta\lambda = 10$  nm interference filters (triangles), and a pump size of  $w_p = 260$   $\mu\text{m}$ . The dashed horizontal line at  $V = 95\%$  indicates the visibility limit set by the beamsplitter T/R ratio of 58/42. The error margins of 0.005 in the vertical scale are too small to display.

### 8.3.3 Spatial labeling

As our key experiment we have measured the spatial coherence of the generated two-photon wavepacket. Figures 8.7(a) and 8.7(b) show the coincidence count rate measured as a function of the relative transverse beam displacement  $\Delta x$  for 4 mm and 14 mm apertures, and perfect temporal coherence ( $\Delta t = 0$ ). Fitting the data points with Eq. (8.4) yields (FWHM) transverse coherence lengths of  $\Delta x_{\text{coh}} = 184 \pm 10$   $\mu\text{m}$  and  $\Delta x_{\text{coh}} = 54 \pm 4$   $\mu\text{m}$ , respectively. These values are only slightly larger than the values of  $\Delta x_{\text{coh}} = 175$   $\mu\text{m}$  and  $50$   $\mu\text{m}$ , expected from Eq. (8.15). We ascribe these minor deviations to a reduced detection efficiency of photon pairs close to the aperture edges, which leads to effectively smaller aperture sizes and thus increased coherence lengths. This correction disappears if we employ the asymmetric geometry of a 4 mm aperture in one arm and a 14 mm one in the other, and perform the same measurement [see Fig. 8.7(c)]. We then indeed obtain a somewhat smaller transverse coherence length of  $166 \pm 10$   $\mu\text{m}$  that is solely determined by the smallest aperture. Our measurements clearly demonstrate that two-photon interference measured behind smaller apertures results in a larger spatial coherence length, and vice versa.

The observations that a transverse displacement in one of the beams leads to a reduction of the two-photon interference can be easily understood in terms of spatial labeling. This is schematically shown in Fig. 8.1, where the upper circle depicts the pumped area at the crystal. The four lower circles depict images of this pumped area that can potentially be made at both detectors if the appropriate lenses are used (for simplicity we assume perfect imaging without inversion). These images are represented by solid and dashed circles corresponding to whether the photons have travelled the signal (solid) or idler (dashed) path, respectively. Consequently, a solid circle at detector 1 matches a dashed circle in detector 2, and vice versa. The transverse displacement  $\Delta x$  of the idler beam is shown as light-dashed lines.

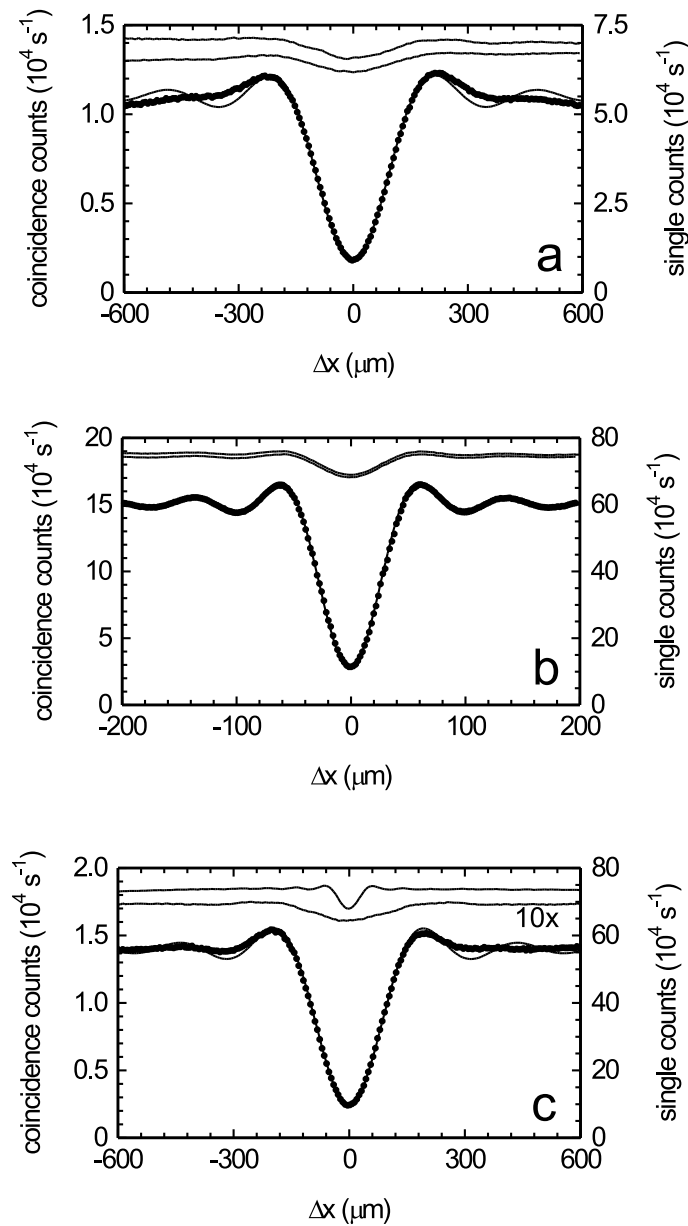


**Figure 8.7:** Two-photon spatial coherence, measured as the coincidence count rate (dots) versus relative transverse displacement behind (a)  $2 \times 4$  mm, (b)  $2 \times 14$  mm and (c)  $4 \times 14$  mm apertures. The solid curves represent the measured single count rates and fits of the coincidence count rates. Especially, the fit in (b) is of excellent quality. The lower single count rate in (c), which was measured behind the 4 mm aperture, has been multiplied by a factor of 10 in order to visualize the dip-structure. Note the differences in the horizontal scales.

Now suppose we detect a photon at detector 1 at the lower-left cross-mark. Tracing this photon back results in two different birth positions (cross-marks in upper circle) separated by  $\Delta x$  at the crystal plane. Tracing its partner photon back to detector 2 then yields two possible imaging positions (lower-right cross-marks) in circle  $s_2$  and  $i_2$ , separated by  $2\Delta x$ . If the resolution of our imaging system is good enough to distinguish between these two possibilities, the “which-path” information provided by this spatial labeling will destroy the two-photon interference. As diffraction by the apertures limits the distinguishability, larger transverse coherence lengths will be attained with smaller apertures, and vice versa. As we need the combined positional information of both photons to decide upon their paths, the diffraction limit of the smallest of the two apertures will largely determine the observed coherence length. As an aside, we note that a similar reasoning can be applied to the results in Ref. [26], where large apertures correspond to a small diffraction limit, good distinguishability between the two probability paths, and a low HOM visibility.

We will next focus our attention on Fig. 8.7(c), which refers to an asymmetric interferometer with apertures of 4 mm and 14 mm in front of the two detectors. At first thought, one might expect the single dip to follow the coincidence dip, irrespective of the aperture geometry. This is however not the case: we measure different widths (FWHM) of  $190 \pm 10 \mu\text{m}$  and  $54 \pm 4 \mu\text{m}$  for the ‘single dips’ behind the 4 mm and 14 mm aperture, respectively, whereas the coincidence width is  $166 \pm 10 \mu\text{m}$ . These values are practically the same as the widths of the single and coincidence dips observed for a symmetric setup with  $2 \times 4$  mm and  $2 \times 14$  mm apertures, respectively [see Figs. 8.7(a) and 8.7(b)].

The intriguing asymmetry in the single dips can be understood as follows. Pair-photons originating from those parts of the signal and idler beam that are captured by the 14 mm aperture but not by the 4 mm one, will be registered only by the detector behind the larger aperture. Simultaneous arrivals of these photons due to bunching will therefore affect only the single dip measured with this detector, but will not contribute to the coincidence dip. As photon bunching occurs within a smaller range of transverse displacements for larger apertures, the measured single dip for the 14 mm aperture in Fig. 8.7(c) is as narrow as the coincidence dip that would be measured with 14 mm apertures in both output channels. Consequently, the 4-mm-aperture single dip in the same figure is almost as broad as the measured coincidence dip.

To demonstrate that the two-photon spatial coherence is very different for interferometers with an even or odd number of mirrors, we have added a second mirror in the signal path, using now six (2+4) mirrors in total. In Figs. 8.8(a) and 8.8(b) we have plotted the coincidence rate versus the transverse displacement  $\Delta x$ , measured in this even geometry for  $2 \times 4$  mm and  $2 \times 14$  mm apertures, respectively. The coincidence dips are fit with the profile  $a \exp[-(\Delta x)^2/b^2] [1 - c \exp(\Delta x)^2/2v^2]$ , where the fit parameter  $v$  is expected to yield the same near-field waist  $w_p$  of the Gaussian pump profile for both aperture sizes. We indeed obtain similar widths of  $v = 253 \mu\text{m}$  and  $v = 237 \mu\text{m}$  for 4 mm and 14 mm apertures, respectively. These values agree well with the measured pump waist of  $w_p \approx 260 \mu\text{m}$ . The exponential prefactor roughly quantifies how the observed coincidence rates decreases when very large beam displacements shift the light outside the active area of the detectors. For this even geometry, we have measured 20% lower single count rates as compared to the odd geometry (see Figs. 8.7(a) and 8.7(b)) because of the increased crystal-aperture distance from 1.20 m to 1.37 m.

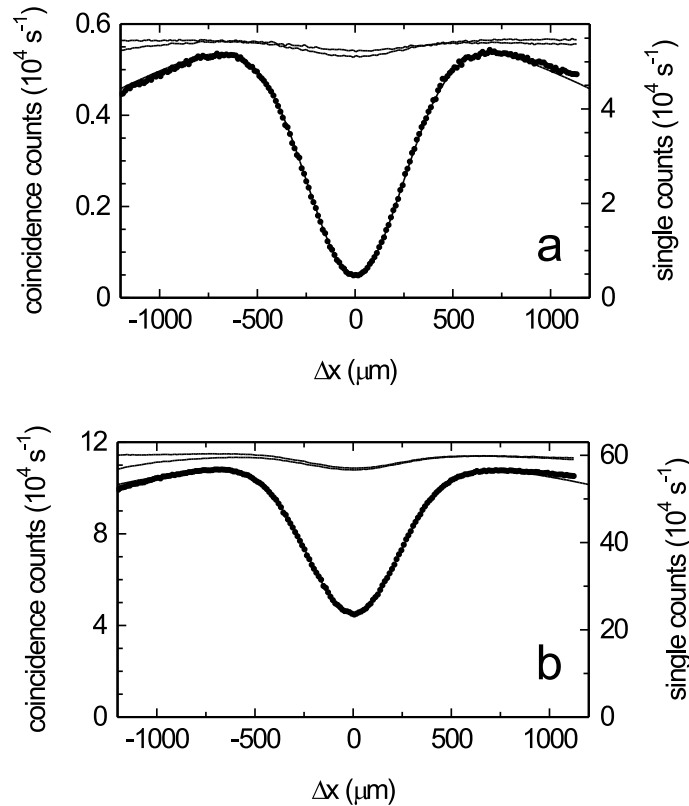


**Figure 8.8:** Two-photon spatial coherence for an even number of mirrors. The coincidence count rate (dots) is plotted versus relative transverse displacement behind (a) 4 mm and (b) 14 mm apertures. Coincidence counts fits and single count rates (solid curves) are plotted as well.

In contrast to the odd geometry, the above result clearly shows that the two-photon spatial coherence for an even number of mirrors is only determined by the pump beam profile and is insensitive to the aperture size. The picture of spatial labeling, shown in Fig. 8.1 for the odd geometry, can also be applied to the even geometry. If we observe a certain photon position at detector 1 (lower-left cross-mark), we can again reconstruct two similar birth positions of this photon at the crystal (upper cross-marks). However, we now find only one position for the corresponding photon at detector 2, as the  $s_2$  and  $i_2$  positions lie precisely on top of each other. This means that, irrespective of the aperture size, one cannot distinguish which probability channel (double reflection or double transmission) the pair-photons has travelled by judging from the detected positions of the partner photon. As the spatial labeling is only contained in the different birth positions for this even geometry, the ‘which-path’ information comes now from the pump beam profile and is no longer determined by the aperture size if the latter is much larger than  $w$ . Only the spatial symmetry of the pump beam and a possible transverse displacement  $\Delta x$  matter.

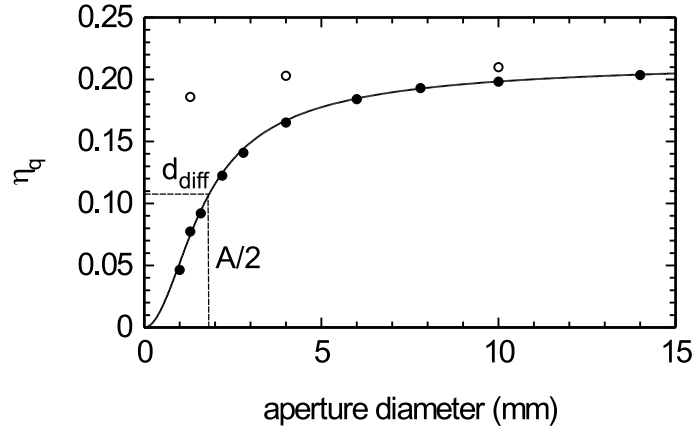


**Figure 8.9:** Measured quantum efficiency  $\eta_q$  versus aperture diameter for equal apertures (solid dots), and for a geometry with one aperture fully open (open circles). The fit (solid curve) yields an asymptotic value of  $A = 0.217$  and a pump beam waist at the aperture plane of  $w = 0.63$  mm.

### 8.3.4 Modal analysis of spatial entanglement

Next we will analyze the two-photon field in terms of a finite number of discrete modes. The shape of the pump laser defines a natural basis for this discrete modal analysis. This natural size will show up in an experiment where one fixes the position of one photon and measures the positional spread  $\theta_{\text{diff}} = 2\theta_p$  of its partner photon in coincidence imaging [30, 31].

To determine this natural size, we have performed a different experiment instead, where we vary the size of both apertures, working in a symmetric situation at (much) higher count rates. The solid dots in Fig. 8.9 depict the measured quantum efficiency  $\eta_q$ , being defined as the ratio of the coincidence count rate over the single rate, as a function of the aperture diameter  $d$ . The sharp decrease in  $\eta_q$  at small apertures results from the positional spread within the photon pair that was mentioned above. This spread is solely determined by the shape of the pump profile and can be fit with the expression [95]

$$\eta_q(d) = \frac{A}{1 + 2w^2/d^2} \left[ 1 - \frac{\sqrt{\pi} \operatorname{erf} \left( \sqrt{1 + d^2/(2w^2)} \right)}{2\sqrt{1 + d^2/(2w^2)}} \right], \quad (8.16)$$

where the asymptotic value  $A$  and the pump beam waist  $w$  at the aperture plane (1.2 m from crystal in our case) are fitting parameters. The diameter of  $d_{\text{diff}} = 1.8$  mm where the measured quantum efficiency is 50% of its asymptotic value (see Fig. 8.9) gives the typical size of the fundamental transverse mode. The solid curve is a fit based on  $A = 0.217$  and  $w = 0.63$  mm. The latter value agrees well with a calculated waist at the aperture plane of  $w = 0.65$  mm, that is based on a Rayleigh range of  $z_R = 0.52$  m, a near-field pump waist of  $w_p = 260 \mu\text{m}$ , and a pump opening angle of  $\theta_p = 0.50$  mrad; these numbers are obtained from a measured pump waist of  $w_z = 1.8$  mm at  $z = 3.6$  m from the crystal. The SPDC diffraction angle  $\theta_{\text{diff}} = 2\theta_p$  (SPDC wavelength  $\lambda = 2\lambda_p$ ) will be used below for the calculation of the

mode number.

The number of transverse modes detectable behind a far-field aperture of radius  $a$  and angular size  $\theta_{\text{det}} = a/L$  is  $N = N_{\text{1D}}^2$ , where the one-dimensional mode number

$$N_{\text{1D}} \approx \frac{\theta_{\text{det}}}{\theta_{\text{diff}}} = \pi \frac{a_p a}{\lambda L}, \quad (8.17)$$

$a_p$  being the radius of the pump spot at the crystal, i.e., the near-field radius of the SPDC radiation. The approximation sign is related to the precise definition of the mode size (FWHM, Gaussian or sharp-edge).

The second equality of Eq. (8.17) enables an easy link to a different measure for the number of interfering transverse modes, being the well-known Fresnel number  $N_F$  given by

$$N_F = \frac{a^2}{\lambda L} \approx \frac{a}{2.8 \Delta x_{\text{coh}}}. \quad (8.18)$$

Here  $\Delta x_{\text{coh}}$  is the (FWHM) transverse coherence length that we defined below Eq. (8.15), and the prefactor  $1/2.8 \approx 1.16 \times 1.22/4$  results from our definition of  $\Delta x_{\text{coh}}$ . For a one-photon field the Fresnel number denotes the number of Fresnel zones that contribute, with alternating signs, to the field transmitted through a rotational symmetric aperture. A comparison between the two quantities defined in Eq. (8.17) and Eq. (8.18) yields  $N_F = N(L/z_R)(2/\pi)$ , where  $z_R = \frac{1}{2}k_p w_p^2$  is the Rayleigh range of the pump. As we typically work at  $L/z_R \approx 2.3$ , the numbers  $N$  and  $N_F$  should be comparable.

From our experimental results we can estimate the mode number  $N$  and Fresnel number  $N_F$  in three different ways. First of all, we can use Eq. (8.17) and divide the detection angle  $\theta_{\text{det}}$  by the measured diffraction angle  $\theta_{\text{diff}}$  to find  $N \approx 3$  and  $N \approx 34$  for 4 mm and 14 mm apertures, respectively. Secondly, we can use Eq. 8.18 and compare the measured transverse coherence length  $\Delta x_{\text{coh}}$  to the aperture size to obtain Fresnel numbers  $N_F \approx 4$  and  $N_F \approx 46$  for 4 mm and 14 mm apertures, respectively. The third measure for the transverse mode number can be deduced by comparing the single count rates shown in Figs. 8.3(a) and 8.3(b). As fiber-coupled detection per definition addresses a single transverse mode, division of these mentioned count rates yields a mode numbers of  $N = 34$ . A similar exercise for a 4 mm aperture (not shown) yields  $N = 7 \times 10^4 / 2.1 \times 10^4 \approx 3$ . These numbers compare well with the mode numbers  $N$  from the first estimate. All estimates show that our experiment addresses typically 4 or 40 modes for the 4 or 14 mm apertures, respectively.

## 8.4 Concluding discussion

We have investigated the two-photon spatial coherence of entangled photon pairs by measuring the coincidence rate in a Hong-Ou-Mandel interferometer as a function of the relative transverse beam displacement for different aperture sizes. The calculated and observed coherence is completely different for an interferometer with an odd or even number of mirrors. For the odd case we have demonstrated that the transverse coherence length is inversely proportional to the aperture size. We also observed a well-defined dip in the single count rate and demonstrated the existence of a combined temporal and spatial labeling that can lead to a

reduction of the HOM visibility under certain conditions. For the even case, we have shown that the transverse coherence length is basically determined by the pump waist.

## **8.5 Acknowledgments**

This work has been supported by the Stichting voor Fundamenteel Onderzoek der Materie. We thank J.P. Woerdman for stimulating discussions and Y.C. Oei for his assistance in the lab.

## Appendix

### 8.A A frequency non-degenerate two-photon interferometer

In this chapter we have observed the two-photon temporal coherence by measuring the coincidence rate as a function of the relative delay  $\Delta t$  between the two interferometer paths. The obtained coincidence patterns (see Fig. 8.3) exhibit a profile that is given by the function  $\text{sinc}(x) = \sin(x)/x$  and determined by the sharp-edged transmission spectrum of the interference filters. This profile is however only sinc-shaped if the filter spectrum is block-shaped and the interference is frequency degenerate, i.e., if the transmission spectra of the filters are both centered around the degeneracy frequency  $\omega_p/2$ . Below we will show that non-degenerate spectra cause an additional modulation of the coincidence pattern. This effect has been studied before for different detection arrangements of photon pairs [96]. The spatial analogue of this modulation effect, which is caused by non-perfect angular beam overlap in the same two-photon interferometer, has been demonstrated in Ref. [97]. A slightly different two-photon interferometer for measuring a similar modulation of the spatial interference has been proposed in Ref. [98].

Consider the even mirror-geometry under perfect spatial coherence ( $\Delta x = 0$ ), where the two-photon visibility is given by Eq. (8.11). In the measurements presented below, we will again use sharp-edged filters but add a (narrower) Gaussian filter in one of the two interferometer arms to remove the frequency degeneracy. For  $T_1(\omega_1) = \exp[-(\omega_1 - \omega_{c1})^2/2\Delta\omega^2]$  and  $T_2(\omega_2) = 1$  Eq. (8.11) now translates into

$$V_{\text{even}}(\Delta t) = \frac{\text{Re} \left[ \int_{-\infty}^{+\infty} d\omega_1 e^{i(2\omega_1 - \omega_p)\Delta t} e^{-(\omega_1 - \omega_{c1})^2/2\Delta\omega^2} \right]}{\int_{-\infty}^{+\infty} d\omega_1 e^{-(\omega_1 - \omega_{c1})^2/2\Delta\omega^2}} = \cos(\tilde{\omega}\Delta t) \cdot e^{-2(\Delta\omega\Delta t)^2}. \quad (8.19)$$

Equation (8.19) shows an interference pattern which exhibits a Gaussian envelop and a cosine modulation. The modulation or beat frequency  $\tilde{\omega} = 2(\omega_{c1} - \omega_p/2)$  is exactly twice the frequency detuning of the 2 nm filter from degeneracy.

We have demonstrated this modulation effect by measuring the two-photon temporal coherence via fiber-coupled detection. In a “quick-and-dirty” way, we add a single 2-nm-wide (FWHM) Gaussian filter in front of one of the present 10-nm-wide sharp-edged filters. We rotate this 2 nm filter over an angle  $\alpha$  from the incident beam to blue-shift its spectrum by  $\Delta\lambda = \lambda_0\alpha^2/2n^2$ , where  $n$  is the refractive index of the filter. The spectrum of the frequency-entangled photons observed in the other arm is then automatically red-shifted by the same  $\Delta\lambda$ . In Fig. 8.10 we show both these non-degenerate spectra (dashed curves) and the measured transmission spectra of the 2 nm and 10 nm filters under normal beam incidence (solid curves). We note that the 2 nm filters are centered at  $\lambda_0 = 813$  nm, while the sharp-edged 10 nm filters are centered at  $\lambda_0 = 811.5$  nm.

In Fig. 8.11 we show the measured coincidence rate for  $\alpha = 5^\circ \pm 1^\circ$  and  $\alpha = 9^\circ \pm 2^\circ$ . We use Eq. (8.19) to fit these coincidence patterns and obtain modulation frequencies of

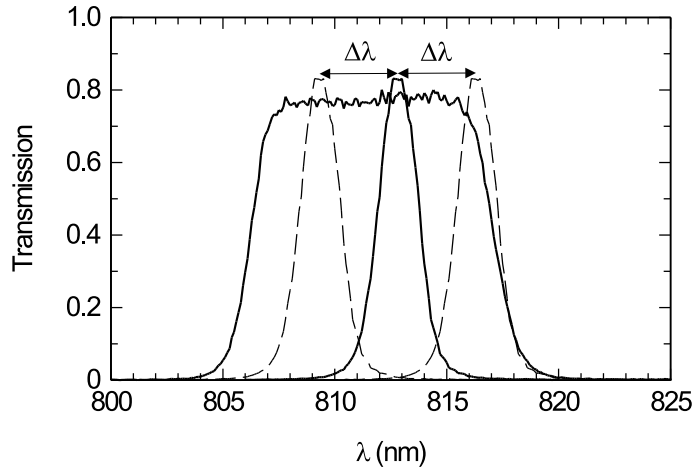


**Figure 8.10:** Measured transmission spectra of the 2 nm and 10 nm interference filters under normal beam incidence (solid curves). The left-dashed curve represents the expected spectrum of the 2 nm filter under an angle  $\alpha$  while the right-dashed curve shows the expected spectrum of the frequency-entangled photons in the other arm.

$\tilde{\omega} = 9.4 \times 10^{12}$  rad/s and  $\tilde{\omega} = 2.0 \times 10^{13}$  rad/s, which correspond to (double) wavelength detunings of  $2\Delta\lambda = \lambda_0^2 \tilde{\omega} / 2\pi c = 3.3$  nm and  $2\Delta\lambda = 7.0$  nm for  $\alpha = 5^\circ$  and  $\alpha = 9^\circ$ , respectively. These values agree reasonably well with the expected detunings of  $2\Delta\lambda = 2.8 \pm 0.6$  nm and  $2\Delta\lambda = 8.9 \pm 2.0$  nm, which we calculate from  $\alpha$  and a filter refractive index of  $n \approx 1.5$ . Despite the “quick-and-dirty” approach our results are accurate enough to demonstrate that the modulation frequency is indeed twice the frequency detuning. Furthermore, the filter bandwidths of  $\approx 1.7$  nm (FWHM), obtained from the envelope fits of the measured coincidence patterns, are close to the measured filter bandwidth of 2 nm.

Besides higher modulation frequencies we have also observed lower coincidence rates for larger angles  $\alpha$ . For normal beam incidence ( $\alpha = 0$ ) we measure a coincidence rate of  $R_c = 530$  s $^{-1}$  while we obtain only  $R_c = 330$  s $^{-1}$  and  $R_c = 260$  s $^{-1}$  for  $\alpha = 5^\circ$  and  $\alpha = 9^\circ$ , respectively. We can illustrate this drop in coincidences from Fig. 8.10. The detuning  $\Delta\lambda$  at larger angles  $\alpha$  shifts the non-degenerate spectrum of the frequency-entangled light (right-dashed curve) towards the edge of the 10 nm filter spectrum, which obviously causes a gradual loss of coincidences. For the depicted  $\Delta\lambda = 3.5$  nm, which corresponds to the measured value for  $\alpha = 9^\circ$ , the 2-nm-wide spectrum is shifted to the very edge of the 10-nm-wide spectrum. The described coincidence loss could have been avoided if the accompanying 10 nm filter would have been removed.

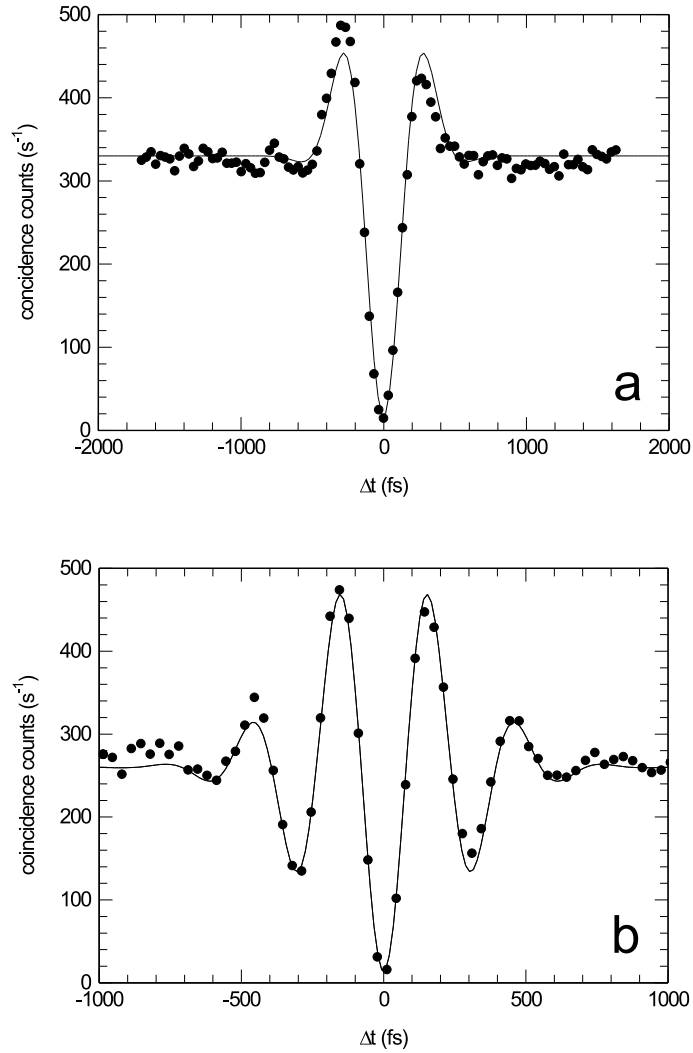


**Figure 8.11:** Coincidence count rate versus delay  $\Delta t$  measured behind single-mode fibers in a frequency non-degenerate system. The center frequency of the narrow 2 nm interference filter was blue-shifted by rotating it (a)  $\alpha = 5^\circ$  and (b)  $\alpha = 9^\circ$  away from the incident beam.

8. Spatial labeling in a two-photon interferometer

## CHAPTER 9

---

### Mode counting in high-dimensional orbital angular momentum entanglement

---

*We study the high-dimensional orbital angular momentum (OAM) entanglement contained in the spatial profiles of two quantum-correlated photons. For this purpose, we use a multi-mode two-photon interferometer with an image rotator in one of the interferometer arms. By measuring the two-photon visibility as a function of the image rotation angle we measure the azimuthal Schmidt number, i.e., we count the number of OAM modes involved in the entanglement; in our setup this number is tunable from 1 to 8.*

*M.P. van Exter, P.S.K. Lee, S. Doesburg, and J.P. Woerdman, submitted to Phys. Rev. Lett.*

The most popular variety of quantum entanglement involves the *polarization* degree of freedom of two photons; in this case we deal obviously with two (polarization) modes per photon [7, 8, 23]. Recently, there has been a lot of interest in *spatial* entanglement of two photons; in this case the number of modes per photon can be much larger than two so that entanglement is correspondingly (in fact, exponentially) richer [89–91, 99–103]. This interest is motivated, fundamentally, by the desire to understand the nature of quantum entanglement in a high-dimensional Hilbert space. From the point of view of applications the high-dimensional case is important since it holds promise for implementing high-dimensional alphabets for quantum information, e.g. for quantum key distribution [104]. A popular basis for the spatial modes is the basis in which the modes are distinguished on account of their orbital angular momentum (OAM) [100–102]. An issue of much discussion in high-dimensional entanglement, OAM or otherwise, is how many modes are involved, beyond the statement that this number is (much) larger than 2 [39, 99–102, 105]. In this chapter we demonstrate a practical method to quantify the number of OAM spatial modes involved in biphoton entanglement; in our experiment this number has been varied in a controlled way from 1 to 8. This result has been achieved by using a special two-photon interferometer.

Our two-photon interferometer contains an image rotator in one of its arms (see Fig. 9.1). Similar interferometers with built-in rotation have only been tested at the *one-photon* level, where the rotation has been linked to a topological (Berry) phase [106]. A one-photon interferometer with an image reversal has been shown to act as a sorter between even and odd spatial modes [107, 108]. We will instead consider *two-photon* interference in an interferometer with built-in rotation.

In two-photon interference experiments, two photons are combined on a beamsplitter, before being detected. These experiments, which have been pioneered by Hong, Ou and Mandel (HOM) [27], demonstrate an effective bunching between the photons in each pair, but only if the optical beams have good spatial and temporal overlap. More recent versions of these “HOM” experiments study the generation of spatial anti-bunching [90], and the effect of a modified pump profile (TEM<sub>01</sub> versus TEM<sub>00</sub>) on the interference pattern (bunching versus anti-bunching) [89, 91].

The key question that we will address is what the observed two-photon interference in our two-photon-interferometer-with-built-in-rotation tells us about the spatial entanglement between the two multi-mode beams. As our geometry leads to an effective separation of the radial and azimuthal degrees of freedom, the experiment provides information on the entanglement between the orbital angular momenta (OAM) of the two photons [100–102]. We will show that the experiment allows to measure the azimuthal Schmidt number, i.e., it allows to count the number of entangled OAM modes.

Figure 9.1 shows a schematic overview of our two-photon interferometer. We mildly focus light from a krypton ion laser ( $\lambda=407$  nm,  $\theta_p = 0.50$  mrad divergence) onto a 1-mm-thick  $\beta$ -barium borate (BBO) crystal to generate quantum-entangled photon pairs at 814 nm via (type-I) spontaneous parametric down-conversion. These twin photons travel along the individual interferometer arms, one of them through an image rotator, before they are combined at a beam-splitter. Two-photon interference is observed by recording the number of coincidences as a function of the delay  $\Delta t$  between the two arms with single-photon counters (SPC). The limited detection bandwidth (5 nm) and detection angle ( $< 7$  mrad) assure operation in the so-called thin-crystal limit [34], where phase-matching is automatically fulfilled.

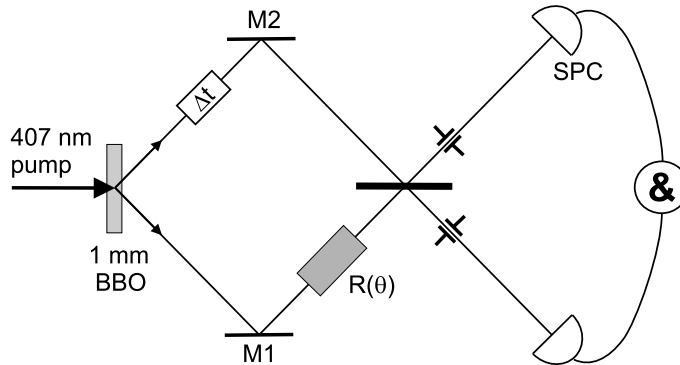


**Figure 9.1:** Schematic view of the experimental setup, representing a two-photon interferometer with an image rotator  $R(\theta)$  in one arm. The image rotator  $R(\theta)$  consists of four out-of-plane mirrors.

In this limit, the spatial properties of the detected two-photon field are solely determined by the pump profile.

We study the effect of an image rotation  $R(\theta)$  on the two-photon interference under a symmetric  $TEM_{00}$  pump profile and for different aperture sizes, positioned approximately in the far field at  $L = 1.5$  m from the crystal. The apertures allow us to control the detected number of entangled spatial modes which, together with the rotation angle  $\theta$ , are the essential parameters in our experiment. We typically use an asymmetric configuration, where one circular aperture is much larger than the other and thereby effectively “fully open”. We call the setup depicted in Fig. 9.1 “even”, as it has an even number of mirrors in the interferometer (M1 and M2). The experimental results depicted in Figs. 9.2-9.4 have, however, been obtained with an “odd” number of mirrors (see below).

Figure 9.2 shows the measured coincidence rate as a function of the time delay  $\Delta t$  at a fixed rotation angle of  $\theta = -30^\circ$ . The reduced coincidence rate around  $\Delta t = 0$  demonstrates how two-photon interference produces an effective bunching of the two incident photons in either of the two output channels [27]. The shape of the interference pattern is the same for both geometries: its width of  $\approx 260$  fs (FWHM) is Fourier-related to the transmission spectrum of our filters (not shown in Fig. 1) and agrees within a few percent with the value expected for a  $\Delta\lambda = 5$  nm bandwidth. The modulation depth or so-called HOM visibility, however, is quite different, being  $89.5 \pm 0.5$  % for the 1 mm aperture and only  $15.5 \pm 0.5$  % for the 10 mm aperture, the other aperture being “fully open” in both cases.

The reduced visibility implies a loss of entanglement and indicates the presence of spatial labeling. If the aperture size and image-rotation angle allow one to decide which of the two photons exiting the beamsplitter travelled which path in the interferometer, the two-photon interference will disappear. This discrimination can be realized by any possible imaging device (between beamsplitter and detector) and even does not need to be applied; it is sufficient if it can be done “only in principle”. Experiments with an even number of mirrors always yielded visibilities close to 100% irrespective of rotation angle; apparently labeling occurs only when the total number of mirrors in the interferometer is odd.

Coincidence measurements like those presented in Fig. 9.2 were repeated for various

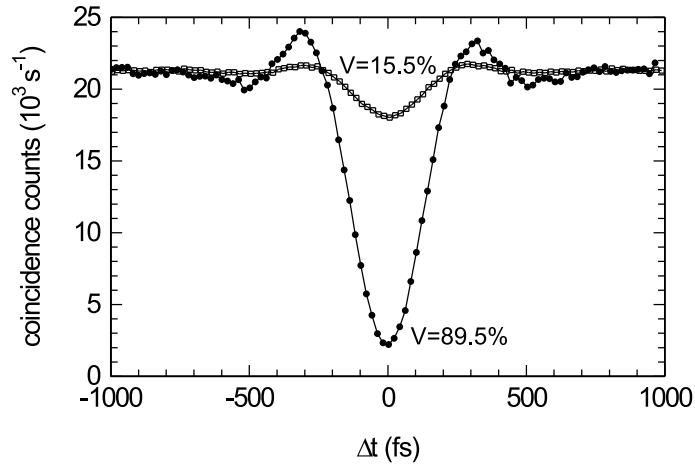


**Figure 9.2:** Two-photon coincidence rate versus the time delay  $\Delta t$  between the two interferometer arms, measured at a fixed rotation angle of  $\theta = -30^\circ$  behind a 1 mm aperture (dots) and a 10 mm aperture (squares). The coincidence rate measured for the 1 mm aperture has been multiplied by the area ratio ( $\approx 100\times$ ) for a direct comparison with the other geometry.

aperture sizes. Combining these results lead to Fig. 9.3, which shows the HOM visibility at a fixed rotation angle of  $\theta = -30^\circ$  as a function of the aperture diameter. The drop in visibility at larger apertures illustrates the above discussion on spatial labeling. The diffraction limit imposed by the smaller apertures frustrates the observation of such labeling.

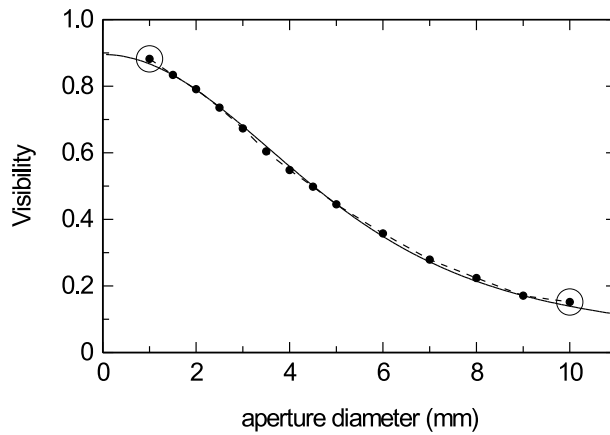


**Figure 9.3:** Two-photon visibility versus the aperture diameter  $2a$ , measured at a fixed rotation angle of  $\theta = -30^\circ$ . The solid curve represents a fit. The two encircled data points correspond to the interference patterns shown in Fig. 9.2.

By repeating the measurements shown in Fig. 9.3 for a series of fixed rotation angles we obtain a two-dimensional table of visibilities  $V(a, \theta)$ . By interchanging the rows and

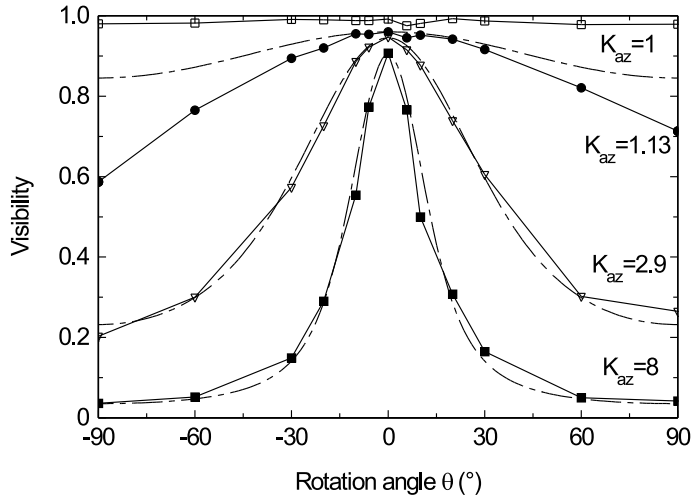


**Figure 9.4:** Two-photon visibility measured as a function of the rotation angle  $\theta$  behind different aperture geometries (specified by the azimuthal Schmidt number  $K_{az}$ ) and behind single-mode fibers ( $K_{az} = 1$ ). The three dashed lines have been calculated from Eq. (9.1).

columns in this table, we now also obtain the visibility  $V(\theta)$  as a function of rotation angle  $\theta$  for various *fixed detection geometries*. Figure 9.4 shows these results for four different geometries, which are specified by their azimuthal Schmidt number  $K_{az}$  (see below). All curves are symmetric under the operation  $\theta \leftrightarrow -\theta$  ( $\theta = 0^\circ$  corresponds to no image rotation) and periodic in  $\theta \leftrightarrow \theta + 180^\circ$ .

For detection behind single-mode fibers (labeled as  $K_{az} = 1$ ) the obtained visibilities are at least 98%, independent of  $\theta$ . As the fundamental mode detected by these fibers is rotationally symmetric, spatial labeling and thus loss of interference will not occur under any image rotation. For free-space detection behind small apertures (small  $K_{az}$ ) we observe a relatively mild effect of image rotation on the spatial entanglement. For larger apertures, this effect is much more drastic and leads to a visibility as low as 4% at  $\theta = 90^\circ$  for  $K_{az} = 8$ . The reason for this reduction is that free-space detectors also monitor the higher-order modes. As linear combinations of these higher-order modes are no longer invariant under rotation, the correlated images at the two detectors now provide labeling information that allows one to distinguish between the interference paths followed by the two photons; a lower visibility results.

The fits in Figs. 9.3 and 9.4 are based on the following analytic expression that can be derived for the “asymmetric odd” configuration with hard-edged apertures [109]

$$V(a \sin \theta) = (1 - \exp(-\xi)) / \xi, \quad (9.1)$$

where  $\xi = 2(a/w_d)^2 \sin^2 \theta$  and  $a$  is the aperture radius. The diffraction waist  $w_d = 2L\theta_p$ , or angular spread of one photon at a fixed position of the other, is twice the size of the pump in the (far-field) detection plane [31]. The solid curve in Fig. 9.3 is a fit based on  $w_d = 1.4$  mm, in agreement with the mentioned values of  $L$  and  $\theta_p$ . The three dashed curves in Fig. 9.4 are

based on the same value.

We now come to the essence of this chapter, being the question ‘‘How can we count the number of orbital angular momentum (OAM) modes involved in the high-dimensional entanglement’’. The answer follows directly from an expression of  $V(\theta)$  in terms of OAM (or  $l$ ) modes,

$$V(\theta) = \sum_l P_l \cos(2l\theta) \quad (9.2)$$

(we will derive this expression at the end of the chapter). Here  $P_l$  (with  $\sum_l P_l = 1$ ) is the probability to detect a photon pair with orbital angular momenta  $(l, -l)$  (with  $-\infty < l < \infty$ ). Equation (9.2) shows that the observed visibility  $V(\theta)$  is a weighted sum over contributions from each group of  $l$ -modes that oscillate, with their own angular dependence, between  $V_l = 1$  (HOM dip) and  $V_l = -1$  (HOM peak). A Fourier transformation of  $V(\theta)$  directly yields the modal distribution  $P_l$ .

In order to convert the modal distribution  $P_l$  into a single number that counts the effective number of entangled OAM modes, we use the azimuthal Schmidt number as  $K_{az} \equiv 1/\sum_l P_l^2$ , in analogy with the general form for modal decompositions [110, 111]. The relation between the azimuthal Schmidt number  $K_{az}$  and the full 2D Schmidt number  $K_{2D}$ , where the summation runs over both azimuthal and radial mode numbers, depends on the size of the detecting apertures. For small apertures we find  $K_{az} \approx K_{2D}$ ; for large apertures we find  $K_{az} \approx 2\sqrt{K_{2D}}$  with a shape-dependent prefactor.

Based on the above description, we count the number of entangled OAM modes in our experiment in the following way: For the three lower curves in Fig. 9.4 we first performed a Fourier analysis of the normalized  $V(\theta)/V(0)$  to obtain the probability distribution  $P_l$  for each curve. The azimuthal Schmidt numbers that we calculated from these distributions ranged from  $K_{az} = 1.13$  for the 1 mm aperture, to  $K_{az} = 2.9$  for the 4 mm aperture, and  $K_{az} = 8$  for the 10 mm aperture, with many values in between. The aperture clearly allows us to tune the effective number of entangled modes.

We have repeated our measurement series for a symmetric configuration, with equal aperture sizes in front of both detectors. The general appearance of this new set of visibilities  $V(\theta)$  (not shown) was similar to that measured with one aperture fully open. The small broadening of the new  $V(\theta)$  profile as compared to Fig. 9.4 indicates a slight reduction in the effective mode number  $K_{az}$ .

It is instructive to also consider apertures with *Gaussian* instead of hard-edged transmission profiles ( $T(r) = \exp(-2r^2/\tilde{a}^2)$ ), as this allows for a complete (radial and azimuthal) analytic Schmidt decomposition of the detected field, assuming two identical apertures [112]. This decomposition yields the simple Airy profile [109]

$$V(\theta) = \frac{1}{1 + (K_{2D} - 1) \sin^2 \theta}, \quad (9.3)$$

where  $K_{2D} = 1 + \frac{1}{2}(\tilde{a}/w_d)^2$  is the 2D Schmidt number. The Airy profile has almost the same shape as the function described by Eq. (9.1).

We conclude now with the promised derivation of Eq. (9.2). This is based on a description of the two-photon field as a sum over discrete spatial modes, instead of an integral over a plane-wave continuum. In this so-called Schmidt decomposition [14], the two-photon field is

represented by the pure state:

$$|\Psi\rangle = \sum_i \sqrt{\lambda_i} |u_i\rangle \otimes |v_i\rangle, \quad (9.4)$$

where  $|u_i\rangle$  and  $|v_i\rangle$  are two sets of orthonormal transverse modes. The Schmidt number  $K = 1/(\sum_i \lambda_i^2)$ , with  $\sum \lambda_i = 1$ , quantifies the effective number of participating modes.

Generally, the Schmidt decomposition of the generated field is very difficult to calculate, as its spatial extent depends both on the pump geometry and on phase matching [39, 105]. We instead consider only the relevant detected field, being the two-photon field behind the detection apertures. The Schmidt decomposition of this field is quite different and can often be done analytically [112] when the apertures are small enough to neglect phase-matching, as is the case in our experiment. The inclusion of the aperture transmission in the detected two-photon field is the key element in our present analysis.

For the rotationally-symmetric ( $l = 0$ ) pump that we use, the symmetry of the two-photon field is such that the Schmidt decomposition of the detected field factorizes as

$$|\Psi\rangle_{in} = \sum_l \sum_p \sqrt{\lambda_{l,p}} |l, p\rangle' \otimes |-l, p\rangle'', \quad (9.5)$$

where  $l$  and  $p$  are the azimuthal and radial quantum numbers and  $|l, p\rangle'$  and  $|-l, p\rangle''$  are the Schmidt eigenmodes of the detected field. The mentioned symmetry restricts these modes to ‘‘Laguerre-Gaussian-like’’ field profiles of which the precise radial distribution is co-determined by the detection apertures. As our amplitude coefficients  $\sqrt{\lambda_{l,p}}$  already contain the effects of aperture filtering, they will decrease rapidly both for high  $p$  and high  $l$  values (high  $l$ -states are quite extended even for  $p = 0$ ). A summation over the radial mode number  $p$  yields the OAM probability  $P_l = \sum_p \lambda_{l,p}$ .

As a last step, we propagate the two-photon field of Eq. (9.5) through our interferometer and calculate the expected two-photon visibility  $V(\theta)$ . This propagation will modify the two-photon field in the following ways: every mirror reflection changes the handedness by inverting the OAM of each  $l$ -state from  $l$  to  $-l$ . The image rotation  $R(\theta)$  adds a phase factor  $\exp(il\theta)$  to each  $l$ -state. The relevant beamsplitter operations are the double transmission, which leaves the  $l$ -states unaffected, and the double reflection, which swaps the labels and changes the handedness. None of these operations affect the radial component. As the detected  $(l, p)$  states form a complete orthogonal basis, two-photon interference is only observed between states with identical  $(l, p)$  labels in the detection channels. The final result is Eq. (9.2).

For a more general input state, the calculated visibility  $V(\theta)$  for an interferometer with an odd number of mirrors contains terms of the form  $\cos[(l_1 - l_2)\theta]$ , which translate into  $\cos(2l\theta)$  if we apply the conservation of OAM ( $l_1 = -l_2 = l$ ). For an interferometer with an even number of mirrors,  $V(\theta)$  contains terms of the form  $\cos[(l_1 + l_2)\theta]$  instead. Our observation that  $V(\theta) \approx 1$  at any angle  $\theta$  in the ‘‘even-mirror geometry’’, can thus be interpreted as a proof of the existence of OAM entanglement; any photon pair with  $l_1 \neq -l_2$  would make  $V(\theta)$  angular dependent.

In summary, we have demonstrated how the high-dimensional entanglement of orbital angular momentum (OAM) can be characterized with a two-photon interferometer that contains

9. Mode counting in high-dimensional orbital angular momentum entanglement

an odd number of mirrors and an image rotator in one of its interferometer arms. We have shown how a Fourier analysis of the observed angle-dependent visibility  $V(\theta)$  profile yields the full probability distribution over the OAM modes involved in the entanglement. Finally, we have calculated the azimuthal Schmidt number  $K_{az}$  corresponding to the effective number of entangled OAM modes.

This work has been supported by the Stichting voor Fundamenteel Onderzoek der Materie (FOM).

---

## Bibliography

---

- [1] A. Einstein, B. Podolsky, and N. Rosen,  
'Can quantum-mechanical description of physical reality be considered complete?',  
*Phys. Rev.* **47**, 777-780 (1935).
- [2] J.S. Bell,  
'On the Einstein-Podolsky-Rosen paradox',  
*Physics* **1**, 195-200 (1964).
- [3] J.F. Clauser, M.A. Horne, A. Shimony, and R.A. Holt,  
'Proposed experiment to test local hidden-variable theories',  
*Phys. Rev. Lett.* **23**, 880-884 (1969).
- [4] J.F. Clauser and A. Shimony,  
'Bell's theorem: experimental tests and implications',  
*Rep. Progr. Phys.* **41**, 1881-1927 (1978).
- [5] A. Aspect, P. Grangier, and G. Roger,  
'Experimental tests of realistic local theories via Bell's theorem',  
*Phys. Rev. Lett.* **47**, 460-463 (1981).
- [6] C. O. Alley and Y. H. Shih,  
*Proceedings of the Second International Symposium on Foundations of Quantum Me-*  
*chanics in the Light of New Technology, Tokyo, 1986* (Physical Society of Japan,  
Tokyo, 1987);  
Y.H. Shih and C.O. Alley,  
'New type of Einstein-Podolsky-Rosen-Bohm experiment using pairs of light quanta  
produced by optical parametric down conversion',  
*Phys. Rev. Lett.* **61**, 2921-2924 (1988).
- [7] Z.Y. Ou and L. Mandel,  
'Violation of Bell's inequality and classical probability in a two-photon correlation  
experiment',  
*Phys. Rev. Lett.* **61**, 50-53 (1988).

Bibliography

- [8] P.G. Kwiat, K. Mattle, H. Weinfurter, A. Zeilinger, A.V. Sergienko, and Y. Shih, 'New high-intensity source of polarization-entangled photon pairs', *Phys. Rev. Lett.* **75**, 4337-4341 (1995).
- [9] J.D. Franson, 'Bell inequality for position and time', *Phys. Rev. Lett.* **62**, 2205-2208 (1989).
- [10] M.A. Horne, A. Shimony, and A. Zeilinger, 'Two-particle interferometry', *Phys. Rev. Lett.* **62**, 2209-2212 (1989).
- [11] J.G. Rarity and P.R. Tapster, 'Experimental violation of Bell's inequality based on phase and momentum', *Phys. Rev. Lett.* **64**, 2495-2498 (1990).
- [12] W. Tittel, J. Brendel, B. Gisin, T. Herzog, H. Zbinden, and N. Gisin, 'Experimental demonstration of quantum correlations over more than 10 km', *Phys. Rev. A* **57**, 3229-3232 (1998).
- [13] G. Weihs, T. Jennewein, C. Simon, H. Weinfurter, A. Zeilinger, 'Violation of Bell's inequality under strict Einstein locality conditions', *Phys. Rev. Lett.* **81**, 5039-5043 (1998).
- [14] A. Ekert, 'Quantum cryptography based on Bells theorem', *Phys. Rev. Lett.* **67**, 661-663 (1991).
- [15] N. Gisin, G. Ribordy, W. Tittel, and H. Zbinden, 'Quantum cryptography', *Rev. Mod. Phys.* **74**, 145-190 (2002).
- [16] C. Bennett, G. Brassard, C. Crepeau, R. Jozsa, A. Peres, and W.K. Wootters, 'Teleporting an unknown quantum state via dual classical and Einstein-Podolsky-Rosen channels', *Phys. Rev. Lett.* **70**, 1895-1899 (1993).
- [17] D. Bouwmeester, J.W. Pan, K. Mattle, M. Eibl, H. Weinfurter, and A. Zeilinger, 'Experimental quantum teleportation', *Nature* **390**, 575-579 (1997).
- [18] M.A. Nielsen and I.L. Chuang, *Quantum computation and quantum information*, (Cambridge University Press, Cambridge, 2000).
- [19] A. Aspect, 'Bell's theorem: the naive view of an experimentalist', published in R.A. Bertlmann and A. Zeilinger, eds., *Quantum [un]speakables - From Bell to Quantum Information*, (Springer-Verlag, Berlin, 2002).
- [20] D.N. Klyshko, *Photons and Nonlinear Optics*, (Gordon and Breach Science, New York, 1988).
- [21] D.C. Burnham and D.L. Weinberg, 'Observation of simultaneity in parametric production of optical photon pairs', *Phys. Rev. Lett.* **25**, 84-87 (1970).

- [22] P.G. Kwiat, E. Waks, A.G. White, I. Appelbaum, and P.H. Eberhard, 'Ultrabright source of polarization-entangled photons', *Phys. Rev. A* **60**, R773-R776 (1999).
- [23] C. Kurtsiefer, M. Oberparleiter, and H. Weinfurter, 'High-efficiency entangled photon pair collection in type-II parametric fluorescence', *Phys. Rev. A* **64**, 023802 (2001).
- [24] P.S.K. Lee, M.P. van Exter, and J.P. Woerdman, 'Increased polarization-entangled photon flux via thinner crystals', *Phys. Rev. A* **70**, 043818 (2004).
- [25] P.G. Kwiat, 'Hyper-entangled states', *J. Mod. Opt.* **44**, 2173-2184 (1997).
- [26] M. Atatüre, G. Di Giuseppe, M.D. Shaw, A.V. Sergienko, B.E.A. Saleh, and M.C. Teich, 'Multiparameter entanglement in quantum interferometry', *Phys. Rev. A* **66**, 023822 (2002).
- [27] C.K. Hong, Z.Y. Ou, and L. Mandel, 'Measurement of subpicosecond time intervals between two photons by interference', *Phys. Rev. Lett.* **59**, 2044-2046 (1987).
- [28] P.G. Kwiat, A.M. Steinberg, and R.Y. Chiao, 'High-visibility interference in a Bell-inequality experiment for energy and time', *Phys. Rev. A* **47**, R2472-2475 (1993).
- [29] L. Mandel, 'Quantum effects in one-photon and two-photon interference', *Rev. Mod. Phys.* **71**, S274-S282 (1999).
- [30] T.B. Pittman, D.V. Strekalov, D.N. Klyshko, M.H. Rubin, A.V. Sergienko, and Y.H. Shih, 'Two-photon geometric optics', *Phys. Rev. A* **53**, 2804-2815 (1996).
- [31] C.H. Monken, P.H. Souto Ribeiro, and S. Padua, 'Transfer of angular spectrum and image formation in spontaneous parametric down-conversion', *Phys. Rev. A* **57**, 3123-3126 (1998).
- [32] M.H. Rubin, D.N. Klyshko, Y.H. Shih, and A.V. Sergienko, 'Theory of two-photon entanglement in type-II optical parametric down-conversion', *Phys. Rev. A* **50**, 5122-5133 (1994).
- [33] M. Atatüre, A.V. Sergienko, B.M. Jost, B.E.A. Saleh, and M.C. Teich, 'Partial distinguishability in femtosecond optical spontaneous parametric down-conversion', *Phys. Rev. Lett.* **83**, 1323-1326 (1999).
- [34] B.E.A. Saleh, A.F. Abouraddy, A.V. Sergienko, and M.C. Teich, 'Duality between partial coherence and partial entanglement', *Phys. Rev. A* **62**, 043816 (2000).

Bibliography

- [35] M.H. Rubin,  
‘Transverse correlation in optical spontaneous parametric down-conversion’,  
Phys. Rev. A **54**, 5349-5360 (1996).
- [36] B.E.A. Saleh, A. Joobeur, and M.C. Teich,  
‘Spatial effects in two-and four-beam interference of partially entangled biphotons’,  
Phys. Rev. A **57**, 3991-4003 (1998).
- [37] W.K. Wootters,  
‘Entanglement of formation of an arbitrary state of two qubits’,  
Phys. Rev. Lett. **80**, 2245-2248 (1998).
- [38] A. Peres,  
*Quantum Theory: Concepts and Methods*,  
(Kluwer Academic, Boston, 1995).
- [39] C.K. Law and J.H. Eberly,  
‘Analysis and interpretation of high transverse entanglement in optical parametric down conversion’,  
Phys. Rev. Lett. **92**, 127903 (2004).
- [40] A.E. Siegman,  
*Lasers*,  
(University Science Books, Mill Valley, California, 1986).
- [41] Der-Chin Su and Cheng-Chih Hsu,  
‘Method for determining the optical axis and ( $n_e$ ,  $n_o$ ) of a birefringent crystal’,  
Appl. Opt. **41**, 3936-3940 (2002).
- [42] Yeu-Chuen Huang, Chien Chou, and Ming Chang,  
‘Direct measurement of refractive indices ( $n_e$ ,  $n_o$ ) of a linear birefringent retardation plate’,  
Opt. Commun. **133**, 11-16 (1997).
- [43] R.P. Shukla, G. M. Perera, M.C. George, and P. Venkateswarlu,  
‘Measurement of birefringence of optical materials using a wedged plate interferometer’,  
Opt. Commun. **78**, 7-12 (1990).
- [44] Ming-Horng Chiu, Cheng-Der Chen, and Der-Chin Su,  
‘Method for determining the fast axis and phase retardation of a wave plate’,  
J. Opt. Soc. Am. A **13**, 1924-1929 (1996).
- [45] M. Schubert, B. Rheinländer, J.A. Woollam, B. Johs, and C.M. Herzinger,  
‘Extension of rotating-analyzer ellipsometry to generalized ellipsometry: determination of the dielectric function tensor from uniaxial TiO<sub>2</sub>’,  
J. Opt. Soc. Am. A **13**, 875-883 (1996).
- [46] G.E. Jellison Jr., F.A. Modine, and L.A. Boatner,  
‘Measurement of the optical functions of uniaxial materials by two-modulator generalized ellipsometry: rutile (TiO<sub>2</sub>)’,  
Opt. Lett. **22**, 1808-1810 (1997).
- [47] J.D. Hecht, A. Eifler, V. Riede, M. Schubert, G. Krauß, and V. Krämer,  
‘Birefringence and reflectivity of single-crystal CdAl<sub>2</sub>Se<sub>4</sub> by generalized ellipsometry’,  
Phys. Rev. B **57**, 7037-7042 (1998).

- [48] V.G. Dmitriev, G.G. Gurzadyan, and D.N. Nikogosyan, *Handbook of Nonlinear Optical Crystals*, (Springer-Verlag, Berlin, 1999).
- [49] A.V. Shubnikov, *Principles of optical crystallography* (translated from Russian), (Consultants Bureau, New York, 1960).
- [50] F.I. Fedorov and T.L. Kotyash, ‘Transmission of light through a transparent uniaxial crystal plate’, *Optics and Spectroscopy* **12**, 162-165 (1962) (translated from Russian: *Optika i spektroskopiya* **12**, 298-303 (1962)).
- [51] D. Eimerl, L. Davis, S. Velsko, E.K. Graham, and A. Zalkin, ‘Optical, mechanical, and thermal properties of barium borate’, *J. Appl. Phys.* **62**, 1968-1983 (1987).
- [52] Free software from Sandia National Laboratories, <http://www.sandia.gov/imrl/X1118/xxtal.htm>.
- [53] For collinear phase-matching the expected SPDC bandwidth is precisely as stated. For emission at a fixed nonzero angle the bandwidth will, however, depend on whether one detects the *e*- or *o*-polarized light; these cases are not equivalent as the two angles can differ on account of the relation  $\omega_o \theta_o = -\omega_e \theta_e$ . The extra term that appears in the expression for  $\Delta\omega_{\text{SPDC}}$  has a relative strength of  $\pm 2\theta_{\text{off}}^2 / \{\bar{n}(n_{gr,o} - n_{gr,e})\}$ , making the spectral bandwidth of the *e*-polarization somewhat (13% for our system) smaller than that of the *o*-polarization.
- [54] An extensive mathematical analysis of the fiber-coupled system is given by Bovino *et al.* [56]. If our described scaling (which in Bovino’s terminology translates in  $r_p \propto w \propto L$ ) is applied to their Eq. (5) the (one- and two-) photon yield per mW of pump power is indeed found to scale as  $1/L$ .
- [55] The spectrometer throughput was measured to be 28%, 19% and 10% for wavelengths of 720 nm, 815 nm and 900 nm, respectively, while the specified detector efficiency decreases from 73% to 60% to 38% at these wavelengths.
- [56] F.A. Bovino, P. Varisco, A.M. Colla, G. Castagnoli, G. Di Giuseppe and A.V. Sergienko, ‘Effective fiber-coupling of entangled photons for quantum communication’, *Opt. Comm.* **227**, 343-348 (2003).
- [57] P. Trojek, Ch. Schmid, M. Bourennane, H. Weinfurter, and Ch. Kurtsiefer, ‘Compact source of polarization-entangled photon pairs’, *Opt. Express* **12**, 276-281 (2004).
- [58] A.V. Sergienko, M. Atatüre, Z. Walton, G. Jaeger, B.E.A. Saleh, and M.C. Teich, ‘Quantum cryptography using femtosecond-pulsed parametric down-conversion’, *Phys. Rev. A* **60**, R2622-2625 (1999).
- [59] A.V. Sergienko and G.S. Jaeger, ‘Quantum information processing and precise optical measurement with entangled-photon pairs’, *Contemp. Phys.* **44**, 341-356 (2003).

Bibliography

- [60] A. Migdall,  
'Correlated-photon metrology without absolute standards',  
Physics Today January 1999, 41-46 (1999)
- [61] T.W. Ebbesen, H.J. Lezec, H.F. Ghaemi, T. Thio, and P.A. Wolff,  
'Extraordinary optical transmission through sub-wavelength hole arrays',  
Nature **391**, 667-669 (1998).
- [62] L. Martín-Moreno, F.J. García-Vidal, H.J. Lezec, K.M. Pellerin, T. Thio, J.B. Pendry,  
and T.W. Ebbesen,  
'Theory of extraordinary optical transmission through subwavelength hole arrays',  
Phys. Rev. Lett. **86**, 1114-1117 (2001).
- [63] H.F. Ghaemi, T. Thio, D.E. Grupp, T.W. Ebbesen, and H.J. Lezec,  
'Surface plasmons enhance optical transmission through subwavelength holes',  
Phys. Rev. B **58**, 6779-6782 (1998).
- [64] S. Enoch, E. Popov, M. Neviere, and R. Reinisch,  
'Enhanced light transmission by hole arrays',  
J. Opt. A. **4**, S83-S87 (2002).
- [65] D.E. Grupp, H.J. Lezec, T.W. Ebbesen, K.M. Pellerin, and T. Thio,  
'Crucial role of metal surface in enhanced transmission through subwavelength apertures',  
Appl. Phys. Lett. **77**, 1569-1571 (2000).
- [66] C. Sönnichsen, A.C. Duch, G. Steininger, M. Koch, G. von Plessen, and J. Feldmann,  
'Launching surface plasmons into nanoholes in metal films',  
Appl. Phys. Lett. **76**, 140-142 (2000).
- [67] E. Altewischer, M.P. van Exter, and J.P. Woerdman,  
'Plasmon-assisted transmission of entangled photons',  
Nature **418**, 304-306 (2002).
- [68] E. Altewischer, M.P. van Exter, and J.P. Woerdman,  
'Polarization analysis of propagating surface plasmons in a subwavelength hole array',  
J. Opt. Soc. Am. B **20**, 1927-1931 (2003).
- [69] E. Altewischer, C. Genet, M.P. van Exter, P.F.A. Alkemade, A. van Zuuk, and E.W.J.M.  
van der Drift,  
'Polarization tomography of metallic nanohole arrays',  
Opt. Lett. **30**, 90-92 (2005).
- [70] E. Altewischer, M.P. van Exter and J.P. Woerdman,  
'Analytic model of optical depolarization in square and hexagonal nanohole arrays',  
J. Opt. Soc. Am. B **22**, 1731-1736 (2005).
- [71] F. Le Roy-Brehonnet and B. Le Jeune,  
'Utilization of Mueller matrix formalism to obtain optical targets depolarization and  
polarization properties',  
Prog. Quant. Electr. **21**, 109-151 (1997).
- [72] P.G. Kwiat, S. Barraza-Lopez, A. Stefanov, and N. Gisin,  
'Experimental entanglement distillation and 'hidden' non-locality',  
Nature **409**, 1014-1017 (2001).

- [73] Y.H. Kim,  
‘Quantum interference with beamlike type-II spontaneous parametric down-conversion’,  
Phys. Rev. A **68**, 013804 (2003).
- [74] E. Moreno, F.J. García-Vidal, D. Erni, J.I. Cirac, and L. Martín-Moreno,  
‘Theory of plasmon-assisted transmission of entangled photons’,  
Phys. Rev. Lett. **92**, 236801 (2004).
- [75] A. Aiello and J.P. Woerdman,  
‘Intrinsic entanglement degradation by multimode detection’,  
Phys. Rev. A **70**, 023808 (2004).  
(1988)
- [76] A. Joobeur, B.E.A. Saleh, and M.C. Teich,  
‘Spatiotemporal coherence properties of entangled light beams generated by parametric down-conversion’,  
Phys. Rev. A **50**, 3349-3361 (1994).
- [77] T.E. Keller and M.H. Rubin,  
‘Theory of two-photon entanglement for spontaneous parametric down-conversion driven by a narrow pump pulse’,  
Phys. Rev. A **56**, 1534-1541 (1997).
- [78] W.P. Grice and I.A. Walmsley,  
‘Spectral information and distinguishability in type-II down-conversion with a broadband pump’,  
Phys. Rev. A **56**, 1627-1634 (1997).
- [79] The phase mismatch is expressed by  $\phi = \Delta k_z L/2$ , where  $\Delta k_z = k_{p,z} - k_{o,z} - k_{e,z}$ . Eq. (6.2), basically given in Ref. [35], is obtained by Taylor-expanding  $k_{i,z} = n_i(\omega_i, \frac{\theta_{i,y}}{n_i}) \frac{\omega_i}{c} \cos(\frac{\theta_{i,x}}{n_i}) \cos(\frac{\theta_{i,y}}{n_i})$  around the external angles  $\theta_{i,x} = \theta_{i,y} = 0$ , using  $\partial n / \partial \theta_{y,ext} = \rho$  for the extra-ordinary rays.
- [80] A. Zeilinger,  
‘Experiment and the foundations of quantum physics’,  
Rev. Mod. Phys. **71**, S288-S297 (1999).
- [81] P.S.K. Lee, M.P. van Exter, and J.P. Woerdman,  
‘How focused pumping affects type-II spontaneous parametric down-conversion’,  
Phys. Rev. A **72**, 033803 (2005).
- [82] S. Castelletto S, I.P. Degiovanni IP, and V. Schettini,  
‘Spatial and spectral mode selection of heralded single photons from pulsed parametric down-conversion’,  
Opt. Express **13**, 6709-6722 (2005).
- [83] T.B. Pittman, D.V. Strekalov, A. Migdall, M.H. Rubin, A.V. Sergienko, and Y.H. Shih,  
‘Can two-photon interference be considered the interference of two photons?’,  
Phys. Rev. Lett. **77**, 1917-1920 (1996).
- [84] J.G. Rarity and P.R. Tapster,  
‘Quantum interference: experiments and applications’,  
Phil. Trans. R. Soc. Lond. A **355**, 2267-2277 (1997).

*Bibliography*

- [85] T. Yamamoto, M. Koashi, S.K. Özdemir, and N. Imoto,  
‘Experimental extraction of an entangled photon pair from two identically decohered pairs’,  
*Nature* **421**, 343-346 (2003).
- [86] P.G. Kwiat, A.M. Steinberg, and R.Y. Chiao,  
‘Observation of a quantum eraser: A revival of coherence in a two-photon interference experiment’,  
*Phys. Rev. A* **45**, 7729-7739 (1992).
- [87] T.B. Pittman and J.D. Franson,  
‘Violation of Bell’s inequality with photons from independent sources’,  
*Phys. Rev. Lett.* **90**, 240401 (2003).
- [88] Y.-H. Kim,  
‘Measurement of one-photon and two-photon wave packets in spontaneous parametric downconversion’,  
*J. Opt. Soc. Am. B* **20**, 1959-1966 (2003).
- [89] S.P. Walborn, A.N. de Oliveira, S. Pádua, and C.H. Monken,  
‘Multimode Hong-Ou-Mandel interference’,  
*Phys. Rev. Lett.* **90**, 143601 (2003).
- [90] D.P. Caetano and P.H. Souto Ribeiro,  
‘Generation of spatial antibunching with free-propagating twin beams’,  
*Phys. Rev. A* **68**, 043806 (2003).
- [91] W.A.T. Nogueira, S.P. Walborn, S. Pádua, and C.H. Monken,  
‘Generation of a two-photon singlet beam’,  
*Phys. Rev. Lett.* **92**, 043602 (2004).
- [92] K.J. Resch,  
‘Spatiotemporal few-photon optical nonlinearities through linear optics and measurement’,  
*Phys. Rev. A* **70**, 051803(R) (2004).
- [93] S.E. Spence, D.C. Stoudt, N.L. Swanson, A.D. Parks, and F.E. Peterkin,  
‘A method for balancing the paths of a two-photon interferometer’,  
*Rev. Sci. Instrum.* **71**, 23-26 (2000).
- [94] K.J. Resch, J.S. Lundeen, and A.M. Steinberg,  
‘Experimental observation of nonclassical effects on single-photon detection rates’,  
*Phys. Rev. A* **63**, 020102(R) (2001).
- [95] C.H. Monken, P.H. Souto Ribeiro, and S. Pádua,  
‘Optimizing the photon pair collection efficiency: A step toward a loophole-free Bell’s inequalities experiment’,  
*Phys. Rev. A* **57**, R2267-R2269 (1998).
- [96] H. Kim, J. Ko, and T. Kim,  
‘Two-particle interference experiment with frequency-entangled photon pairs’,  
*J. Opt. Soc. Am. B* **20**, 760-763 (2003).
- [97] H. Kim, O. Kwon, W. Kim, and T. Kim,  
‘Spatial two-photon interference in a Hong-Ou-Mandel interferometer’,  
*Phys. Rev. A* **73**, 023820 (2006).

- [98] J. Visser and G. Nienhuis,  
'Interference between entangled photon states in space and time',  
*Eur. Phys. J. D* **29**, 301-308 (2004).
- [99] R.S. Bennink, S.J. Bentley, R.W. Boyd, and J.C. Howell,  
'Quantum and classical coincidence imaging',  
*Phys. Rev. Lett.* **92**, 033601 (2004).
- [100] A. Mair, A. Vaziri, G. Weihs, and A. Zeilinger,  
'Entanglement of the orbital angular momentum states of photons',  
*Nature* **412**, 313-316 (2001).
- [101] N.K. Langford, R.B. Dalton, M.D. Harvey, J.L. O'Brien, G.J. Pryde, A. Gilchrist, S.D. Bartlett, and A.G. White,  
'Measuring entangled qutrits and their use for quantum bit commitment',  
*Phys. Rev. Lett.* **93**, 053601 (2004).
- [102] S.S.R. Oemrawsingh, X. Ma, D. Voigt, A. Aiello, E.R. Eliel, G.W. 't Hooft, and J.P. Woerdman,  
'Experimental demonstration of fractional orbital angular momentum entanglement of two photons',  
*Phys. Rev. Lett.* **95**, 240501 (2005).
- [103] L. Neves, G. Lima, J.G. Aguirre Gomez, C.H. Monken, C. Saavedra, and S. Pádua,  
'Generation of entangled states of qudits using twin photons',  
*Phys. Rev. Lett.* **94**, 100501 (2005).
- [104] H. Bechmann-Pasquinucci and A. Peres,  
'Quantum cryptography with 3-state systems',  
*Phys. Rev. Lett.* **85**, 3313-3316 (2000).
- [105] J.P. Torres, A. Alexandrescu, and L. Torner,  
'Quantum spiral bandwidth of entangled two-photon states',  
*Phys. Rev. A* **68**, 050301(R) (2003).
- [106] M. Segev, R. Solomon, and A. Yariv,  
'Manifestation of Berry's phase in image-bearing optical beams',  
*Phys. Rev. Lett.* **69**, 590-592 (1992).
- [107] H. Wei, X. Xue, J. Leach, M.J. Padgett, S.M. Barnett, S. Franke-Arnold, E. Yao, and J. Courtial,  
'Simplified measurement of the orbital angular momentum of single photons',  
*Opt. Commun.* **223**, 117-122 (2003).
- [108] H. Sasada and M. Okamoto,  
'Transverse-mode beam splitter of a light beam and its application to quantum cryptography',  
*Phys. Rev. A* **68**, 012323 (2003).
- [109] M.P. van Exter, P.S.K. Lee, and J.P. Woerdman,  
in preparation for submission to *Phys. Rev. A*.
- [110] A. Ekert and P.L. Knight,  
'Entangled quantum systems and the Schmidt decomposition',  
*Am. J. Phys.* **63**, 415-423 (1995).

Bibliography

- [111] The azimuthal Schmidt number  $K_{az}$  that we introduce is closely related to the quantum spiral bandwidth introduced in Ref. [105]; both single out the azimuthal behavior by summing over all radial mode numbers.
- [112] M.P. van Exter, A. Aiello, S.S.R. Oemrawsingh, G. Nienhuis, and J.P. Woerdman, 'Effect of spatial filtering on the Schmidt decomposition of entangled photons', *Phys. Rev. A* **74**, 012309 (2006)

---

## Summary

---

*In this summary, we will introduce light waves and light particles, and explain the aspects of quantum mechanics that are hidden behind the entanglement of light. The specific research on polarization and spatial entanglement of light, that is presented in this thesis, will be highlighted.*

## Light: waves or particles?

In everyday life one can consider light as a wave phenomenon. A light wave is composed of an electric and a magnetic field, both exhibiting the same wave behaviour. A light wave is therefore also known as an electromagnetic wave. Some characteristics of a light wave are the direction of propagation, the wavelength and the polarization. In Figure 1 we show (the electric field of) a light wave at two different times together with the three mentioned wave characteristics. The physical description of light as a wave phenomenon is called wave optics.

The wavelength is defined as the distance between two subsequent wave peaks. In the case of ‘visible light’, or just ‘light’ for convenience, the wavelength determines the color of the light. Blue light has the smallest wavelength of about 400 nm (nm = nanometer = one billionth of a meter). Red light has the largest wavelength of about 750 nm. Light from the sun is ‘white’ since it contains all possible colors, as demonstrated by the well-known rainbow. White sunlight is captured by raindrops after which each color will exit the raindrops via a separate direction. All colors will then be resolved which results in the rainbow effect. Other electromagnetic waves (‘invisible’ light) have a much smaller or a much larger wavelength than that of light. For instance, the wavelength of x-rays is about 10.000 times smaller, whereas the wavelength of radio signals is millions times larger, varying from a few meters to several kilometers.

The polarization is the direction in which the electric field of light oscillates. Figure 1 shows a possible polarization; the polarization perpendicular to this one would be associated with an electric field that oscillates inside and outside this sheet of paper. As sunlight contains all possible polarizations, it is also called *unpolarized* light. By using polarizing materials, one can convert unpolarized light to *polarized* light which has only one single polarization. These materials are applied in polaroid sunglasses.



**Figure 1:** The electric field of a light wave at a certain time and somewhat later (dashed).

So far, we have considered light as a wave phenomenon. Under certain circumstances, light can be described as separate light particles rather than as light waves. These light particles, which are also known as *photons*, are like small packets of energy which contents is solely determined by the wavelength of the light. A smaller wavelength hereby corresponds to a higher photon energy. ‘Blue’ photons therefore contain more energy than ‘red’ photons. The theory that explains the behavior of photons is called *quantum mechanics*, which is also applied to study the behavior of physical objects like atoms and molecules. These latter quantum objects are the building blocks of all matter around us.

## Quantum mechanics

### Quantum superposition

The state of a classical object at an arbitrary moment in time can be given by the object's position and velocity at this specific moment. As an example, we consider a mass that is sliding down an incline without friction. As time goes by, the mass will be lower on the incline and will continuously have a different position. Moreover, the velocity of the mass will increase steadily due to the gravitational acceleration and will therefore have different values at different moments in time. *At an arbitrary moment in time*, however, classical mechanics imposes a *well-determined* state upon the mass, being a position and a velocity.

The above state description is not valid anymore in quantum mechanics. A quantum object can be in more than one state at an arbitrary moment in time. The object is said to be in a *superposition of states*. If our mass would be a quantum object, it could be located somewhere at the top of the incline having a low velocity and, *at the same time*, somewhere down under having a high velocity. This concept of superposition is hardly to imagine in everyday life, but is needed to understand the entanglement of photons.

In analogy to the classical state, we have supposed that the (superposition) state of a quantum object can be given by a well-determined position and velocity as well. However, quantum mechanics teaches us that one cannot *simultaneously* determine the position and the velocity of an object *with full certainty*. If one measures the position with high accuracy, the measured velocity will exhibit a large uncertainty, and vice versa. Therefore, the position and velocity that define the state of our quantum mechanical mass should be read as a position *distribution* and a velocity *distribution*.

### Observation in quantum mechanics

If we want to know the state of a classical object, we can observe the object by performing a measurement. In the case of our mass we can stick some measuring tape along the incline and attach a velocity meter on the mass. By taking a photograph of the system at a certain moment, we can distillate both the position and the velocity of the mass from the photograph, and thus the state of the mass *at this specific moment in time*. It is not surprising that the mass would again have the same position and velocity at the same moment, if we would *not* have made the photograph. In other words, an observation, being a measurement in this case, does not affect the state of an classical object at all.

How different is the quantum mechanical world, where an observation does drastically affect the state of a physical system. If we do *not* observe our quantum mechanical mass (no photoshooting), the mass could be in the mentioned superposition state: the mass has two or more positions and two or more velocities *at one single moment in time*. This state changes as soon as we perform a measurement by photoshooting. Then, our mass may be either somewhere at the bottom of the incline with a high velocity, or somewhere else with another velocity. As a result, our measurement forces the mass to choose for a certain state. In general, a measurement performed on a quantum object automatically 'projects' its superposition state onto one of the possible substates. This property of quantum mechanics is called the 'projection postulate'.

## Quantum entanglement

We now consider a system that contains *two* quantum objects. For convenience, we imagine two table tennis balls, which are classical objects in reality. Both these table tennis balls can be of low and high quality, which we label with one star and three stars, respectively. The two balls are now separated from each other by putting them each in a closed box to prevent any observation. Let us consider the following superposition state for our two-ball system [see Figure 2(a)]: with a probability of 50% ball 1 is of 1-star quality and ball 2 is of 3-star quality, but *simultaneously* and *with equal probability* the opposite holds (3-star quality for ball 1 and 1-star quality for ball 2). As long as both boxes remain closed such that the balls are not observable, the system will stay in the same superposition state and the qualities of the balls are fully undetermined. If we now, for instance, open box 1 and observe ball 1, the superposition will immediately vanish due to the projection postulate and the system will choose one of the two possible states [see Figure 2(b)]. If the 1-star quality is observed for ball 1, then we *immediately* and *with full certainty* know that ball 2 is of 3-star quality, without opening the box 2! On the contrary, observation of the 3-star quality for ball 1 will automatically force ball 2 to have the 1-star quality. The bizarre thing of this experiment is the determination of the quality of ball 2 without any manipulation of ball 2 itself. After all, both balls are strictly separated. This example shows that two quantum objects that are separated by an *arbitrary* distance can act as one single object. This connection is called the *entanglement* of quantum objects.

Of course, classical table tennis balls will not be entangled easily in reality; we have used them only to illustrate quantum entanglement. Photons are quantum objects and can therefore be in an entangled state. In the above example, two entangled photons would play the role of the two table tennis balls whereas the ball quality would correspond to a certain property of the photons. By measuring this property for one of the two photons, we immediately know the outcome for the other photon, without any manipulation of this latter photon and irrespective of the distance between the photons.

As mentioned earlier, this thesis presents the research that has been done on the entanglement of light. A better understanding of this physical phenomenon comes also from the scientific progress in several laboratories around the world. For example, entanglement of photons that are separated by tens of kilometers has already been demonstrated. The ultimate challenge of entanglement research is the development of a *quantum computer* which would outclass the performance of the current computer by several orders of magnitude. In particular, such a quantum computer would be ideal for code-breaking (cryptography).

## Making entangled photons

Entangled photons are usually generated in a particular crystal (a small glass-like plate), where a ‘mother photon’ is split into two identical ‘daughter photons’. The daughter photons are like twins: observation of one of the two photons directly determines the character of the other, though both photons are separated. Entangled photons are therefore also called *twin photons*. The mentioned generation process, named *spontaneous parametric down-conversion*, is shown in Figure 3 and described in Chapter 2. As energy is conserved in this process, the energy of each twin photon is exactly half the energy of the mother photon.

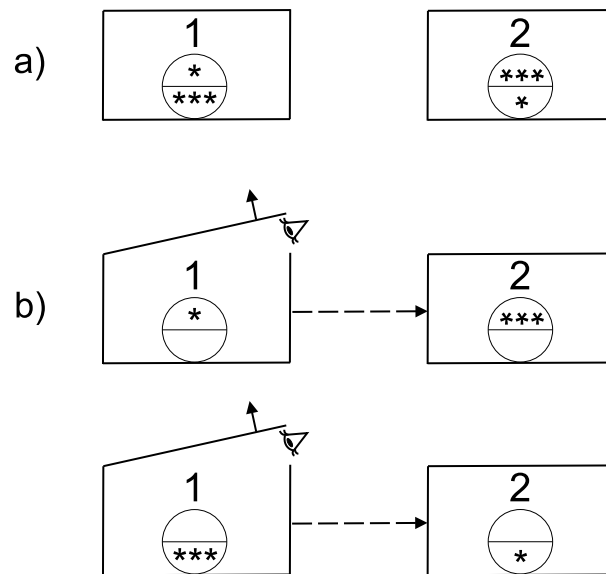


**Figure 2:** (a) Two virtually quantum mechanical table tennis balls are each in a closed box, being in the following superposition state: ball 1 has the 1-star quality and ball 2 has the 3-star quality (upper halves) but, simultaneously and with equal probability, ball 1 has the 3-star quality and ball 2 has the 1-star quality as well (lower halves). The individual ball qualities are thus fully undetermined. (b) By looking inside box 1, ball 1 will immediately have either the 1-star or the 3-star quality. Without opening box 2, ball 2 will then automatically have either the 3-star or the 1-star quality, respectively, as if it is directly connected to ball 1 (dashed arrow). This connection is called entanglement.

In practice, it is usual to split a beam of blue mother photons into two beams, each containing one of the corresponding red twin photons. We can insert a detector in both beams, which ‘clicks’ whenever a twin photon arrives. If both detectors click *simultaneously*, we know that we have observed a photon pair and that entanglement of light can be measured. The generated twin photons are simultaneously entangled with respect to three variables. Below we discuss these three types of entanglement, being entanglement in polarization, time and space.

The individual polarization of the generated twin photons can be in any direction and is therefore fully undetermined. However, measurement of an arbitrary polarization for one of the twin photons immediately forces the polarization of the other twin photon to be in the *perpendicular* direction, without any manipulation of this photon. This is called *polarization entanglement* of photons. As the polarization of light is relatively easy to handle (for instance with polarizing elements), research on this type of light entanglement is most popular.

The two entangled photons are generated in the crystal *at the same time*. At an arbitrary time after their birth, these photons will have travelled the *same* distance from the crystal (see Figure 3). By detecting a photon in only one of the two beams, at a certain distance from the crystal, we know for sure that its partner in the other beam is located at the same distance from the crystal. As this distance is related to the time passed by after the birth of the photon

## Summary

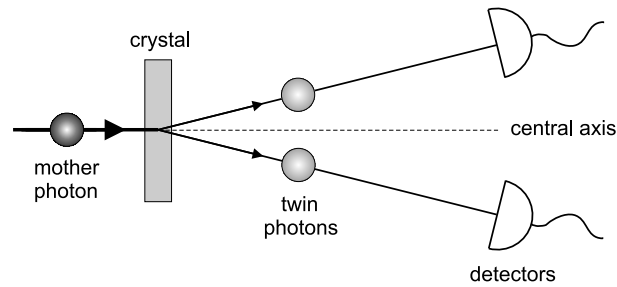


**Figure 3:** Two entangled photons are generated as twins from a mother photon. Both twin photons are located at the same distance from the crystal and their locations are each other's mirror image with respect to the central axis. Although the twin photons are separated, observation of one photon immediately determines the character of the other photon. This so-called entanglement can be measured by inserting a detector in both paths.

pair, we here speak of *time entanglement* of photons.

Twin photons are generated not only at the same time but also *at the same transverse position* in the crystal. The transverse position is the position measured in the direction perpendicular to the incoming beam of mother photons, or perpendicular to the central axis (see Figure 3). The measurement of a certain transverse position for a photon in one of the emitted beams immediately determines the transverse position of its partner in the other beam. This latter position is simply the mirror image of the measured transverse position with respect to the central axis. This type of entanglement is called entanglement of photons in their transverse position, or *spatial entanglement* of light.

## **This thesis**

The research presented in this thesis covers both polarization and spatial entanglement of light. In Chapter 3 we present a novel method for high-accuracy determination of the thickness and cutting angle of the generating crystal. The effect of the crystal thickness on the production rate of polarization-entangled photons is discussed in Chapter 4. We have demonstrated that, under certain circumstances, the production rate is inversely proportional to the crystal thickness: a 0.25 millimeter thick crystal surprisingly yields four times more photon pairs than a 1 millimeter thick one.

In Chapter 5 we compare the degree of polarization entanglement that we have measured in two different experiments. In the first experiment, a metal hole array (hole size smaller than wavelength) is positioned in one of the two beams. In the second experiment, the photons are 'torn apart' by decomposing their polarization in front of the hole array, and 'recovered' again in a reverse way behind the hole array. The latter scheme, seemingly identical to the first one, surprisingly yields a significantly weaker polarization entanglement. This result is ascribed to the propagation of specific waves along the surface of the metal hole array.

In Chapter 6 we study the effect of the spatial character of the mother beam on the spatial character of the two daughter beams. In addition, we investigate the consequences for the

degree of polarization entanglement. In Chapter 7 we show that the measured degree of polarization entanglement strongly depends on the way the twin photons are detected.

In the experiment described in Chapter 8, both twin photons have the possibility to travel along two different paths. We explore whether the measured transverse position of one photon can reveal which path the other photon has travelled. The answer to this question depends on the symmetry of the experimental setup. Chapter 9 treats a similar experiment in which one of the beams is rotated around its own axis. Again, the symmetry of the setup determines whether the degree of spatial entanglement decreases with the amount of rotation. Moreover, this experiment allows us to quantify the size of the spatial structure of the entangled light.

Summary

---

## Samenvatting

---

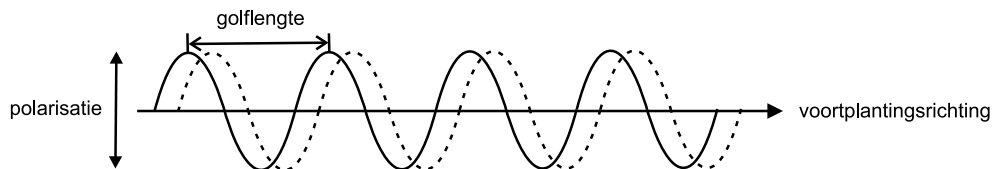
*In deze samenvatting wordt uitgelegd wat lichtgolven en lichtdeeltjes zijn, en welke aspecten van de quantummechanica onder de verstrengeling van licht schuilen. Het specifieke onderzoek naar lichtverstrengeling in polarisatie en de ruimtelijke vrijheidsgraad, dat beschreven staat in dit proefschrift, wordt nader toegelicht.*

## Lichtgolven of lichtdeeltjes?

In het dagelijkse leven kunnen we licht vaak opvatten als een golfverschijnsel. Een lichtgolf bestaat uit een elektrisch en een magnetisch veld, die elk hetzelfde golvende karakter vertonen. Een lichtgolf wordt daarom ook wel een elektromagnetische golf genoemd. Enkele kenmerken van een lichtgolf zijn de voortplantingsrichting, de golflengte en de polarisatie. In figuur 1 is (het elektrische veld van) een lichtgolf op twee tijdstippen weergegeven met de drie genoemde eigenschappen. De natuurkundige beschrijving van licht als een golfverschijnsel is de golfoptica.

De golflengte is de afstand tussen twee opeenvolgende golf toppen. In het geval van ‘zichtbaar licht’, dat hier voor het gemak ‘licht’ wordt genoemd, bepaalt de golflengte de kleur van het licht. Blauw licht heeft de kleinste golflengte van ongeveer 400 nm (nm = nanometer = een miljardste van een meter). Rood licht heeft de grootste golflengte van ongeveer 750 nm. Zonlicht is ‘wit’ omdat het alle kleuren bevat. De welbekende regenboog is hiervan het sprekende bewijs. Het witte zonlicht wordt door de regendruppels ingevangen waarbij elke kleur via een afzonderlijke richting de druppels verlaat. Hierdoor worden alle kleuren gescheiden en ontstaat het regenboog-effect. Andere elektromagnetische golven (‘onzichtbaar’ licht) hebben een veel kleinere of veel grotere golflengte dan die van licht. De golflengte van bijvoorbeeld röntgenstraling is zo’n 10.000 maal kleiner, terwijl de golflengte van radiosignalen miljoenen malen groter is, variërend van enkele meters tot vele kilometers.

De polarisatie is de richting waarin het elektrische veld van het licht op en neer golft. In figuur 1 is een mogelijke polarisatie aangegeven. Een andere polarisatie is de polarisatie loodrecht hierop, welke in dezelfde figuur correspondeert met een elektrisch veld dat als het ware in en uit het papier golft. Zonlicht bezit alle mogelijke polarisaties en wordt daarom *ongepolariseerd* licht genoemd. Door gebruik te maken van zogenaamde polariserende materialen kan ongepolariseerd licht omgezet worden in *gepolariseerd* licht, dat nog een enkele polarisatie heeft. Dit gebeurt onder andere bij polaroid zonnebrillen.



**Figuur 1:** Het elektrische veld van een lichtgolf op een zeker tijdstip en even later (gestippeld).

Hierboven hebben we licht beschouwd als een golfverschijnsel. Onder bepaalde omstandigheden laat licht zich echter beter beschrijven als afzonderlijke lichtdeeltjes die ook wel *fotonen* worden genoemd. Een foton is als het ware een energiepakketje; de hoeveelheid energie van een foton wordt alleen bepaald door de golflengte van het licht. Hierbij geldt dat hoe kleiner de golflengte van het licht, des te groter de energie van het foton. ‘Blauwe’ fotonen bezitten dus meer energie dan ‘rode’ fotonen. De natuurkundige theorie die onder andere het gedrag van fotonen verklaart, is de *quantummechanica*. Verder beschrijft de quantummechanica het gedrag van natuurkundige objecten zoals atomen en moleculen. Dergelijke quantumobjecten zijn de bouwstenen van alle materie om ons heen.

## Quantummechanica

### Quantumsuperpositie

De toestand van een klassiek object op een willekeurig tijdstip kan worden gegeven door zijn positie en snelheid op dat tijdstip. We beschouwen een blokje dat wrijvingsloos van een helling afschuift. Het blokje zal zich in de loop van de tijd steeds lager op de helling bevinden en zodoende voortdurend een andere positie innemen. Daarnaast zal de snelheid van het blokje geleidelijk toenemen als gevolg van de zwaartekrachtsversnelling en elk tijdstip een andere waarde hebben. Echter, de wetten van de klassieke mechanica leggen het blokje *op een willekeurig tijdstip een welbepaalde* toestand op, die gegeven wordt door een positie en een snelheid.

In de quantummechanica is deze toestandsbeschrijving niet meer geldig. Een quantumobject kan zich op een willekeurig tijdstip in meerdere toestanden bevinden. Het object bevindt zich dan in een zogenaamde *superpositie van toestanden*. Als het hiervoor genoemde blokje quantummechanisch zou zijn geweest, kon het zich op één tijdstip zowel bovenaan de helling bevinden met een lage snelheid als onderaan de helling met een grote snelheid. Dit idee van superpositie is in de alledaagse wereld nauwelijks voor te stellen, maar is essentieel om de verstrengeling van fotonen te verklaren.

Voor de analogie met de klassieke toestand hebben we aangenomen dat ook de toestand van een quantumobject, al dan niet in een superpositie, gegeven kan worden door een combinatie van een welbepaalde positie en snelheid van het quantumobject. Echter, volgens de quantummechanica kunnen de positie en de snelheid van een object nooit *tegelijktijd met 100% zekerheid* worden bepaald. Wanneer de positie heel precies wordt gemeten, zal de gemeten snelheid een grote onzekerheid vertonen, en andersom. Voor de toestand van ons quantummechanische blokje is het correcter om voor de combinatie van positie en snelheid een combinatie van *positiespreiding* en *snelheidspreiding* te lezen.

### Waarnemen in de quantummechanica

Wanneer we de toestand van een klassiek object willen weten, kunnen we een waarneming doen door een meting aan het object uit te voeren. In het geval van het blokje kunnen we een meetlint langs de helling plakken en een snelheidsmeter op het blokje plaatsen. Door op een bepaald tijdstip met een camera een foto van het systeem te maken, kunnen we uit de gemaakte foto zowel de positie als de snelheid van het blokje, en daarmee de toestand van het blokje *op dat ene tijdstip* bepalen. Het zal ons niet verbazen dat het blokje op dat ene tijdstip wederom dezelfde positie en snelheid zou hebben gehad als we de foto *niet* hadden gemaakt. Met andere woorden, de waarneming in de vorm van een meting heeft geen enkele invloed op de toestand van een klassiek object.

In de quantummechanica heeft een waarneming juist wel drastische gevolgen voor de toestand van een natuurkundig systeem. Wanneer ons blokje een quantumobject zou zijn geweest en *niet* wordt geobserveerd, door bijvoorbeeld geen fotometing te doen, zou het blokje zich in de eerder genoemde superpositie-toestand kunnen verkeren: het blokje neemt *op één tijdstip* twee of meerdere posities in en heeft twee of meerdere snelheden. Deze toestand verandert echter als we *wel* een fotometing zouden uitvoeren. Het blokje blijkt zich

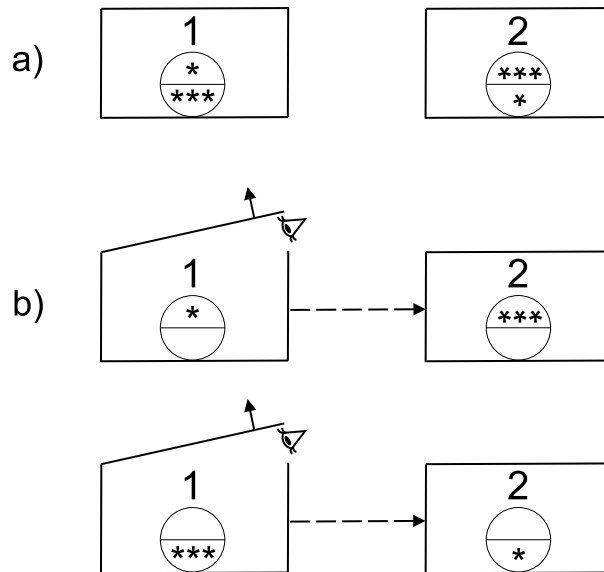
dan bijvoorbeeld ergens onderaan de helling te bevinden en een grote snelheid te bezitten. De fotometing dwingt het blokje dus een bepaalde toestand te kiezen. In het algemeen geldt dat een meting aan een quantummechanisch systeem de superpositie-toestand in een van de mogelijke deeltoestanden wordt 'geprojecteerd'. Dit wordt het *projectiepostulaat* van de quantummechanica genoemd.

## Quantumverstremgeling

We beschouwen nu een systeem bestaande uit *twee* quantumobjecten. Voor het gemak nemen we twee tafeltennisballen die in werkelijkheid klassieke objecten zijn. De tafeltennisballen kunnen elk van lage en hoge kwaliteit zijn die we respectievelijk aanduiden met één ster en drie sterren. We doen de ballen ieder afzonderlijk in een afgedekte doos zodat ze gescheiden en niet waarneembaar zijn. Laten we zeggen dat dit quantummechanische tweeballensysteem zich nu in de volgende superpositie-toestand bevindt [zie figuur 2(a)]: met een kans van 50% heeft bal 1 de 1-sterkwaliteit en bal 2 de 3-sterrenkwaliteit, maar *tegelijkertijd* en *met dezelfde kans* geldt ook het omgekeerde (bal 1 van 3-sterrenkwaliteit en bal 2 van 1-sterkwaliteit). Zolang we beide dozen dichthouden en de ballen niet kunnen zien, blijft het systeem in deze superpositie-toestand verkeren en is de individuele kwaliteit van beide ballen volledig onbepaald. Door nu bijvoorbeeld doos 1 te openen en bal 1 waar te nemen, zal het systeem vanwege het projectiepostulaat onmiddellijk zijn superpositie verliezen en in een van de twee mogelijke toestanden vervallen [zie figuur 2(b)]. Zien we de 1-sterkwaliteit voor bal 1, dan weten we *onmiddellijk* en *met 100% zekerheid* dat bal 2 van 3-sterrenkwaliteit is zonder doos 2 te openen! Zien we daarentegen de 3-sterrenkwaliteit voor bal 1, dan was bal 2 automatisch van 1-sterkwaliteit geweest. Het bizarre van dit experiment is dat de kwaliteit van bal 2 bepaald kan worden zonder ook maar enige invloed op deze bal uit te oefenen. Immers, beide ballen zijn strict gescheiden. Dit voorbeeld laat zien dat twee *willekeurig ver van elkaar verwijderde* quantumobjecten de mogelijkheid hebben om zich als één object voor te doen. Deze relatie noemen we de *verstremgeling* van quantumobjecten.

Uiteraard hebben we klassieke tafeltennisballen alleen maar gebruikt om quantumverstremgeling te illustreren, en zullen ze in werkelijkheid niet snel verstremgeld zijn. Fotonen zijn quantumobjecten en kunnen daardoor wel in een verstremgelde toestand verkeren. In het bovenstaande voorbeeld zouden twee verstremgelde fotonen de rol van de twee tafeltennisballen innemen en correspondeert de balkkwaliteit met een bepaalde eigenschap van de fotonen. Door deze eigenschap aan een van de twee fotonen te meten, weten we onmiddellijk wat de uitkomst voor het andere foton is, *zónder* iets te doen met dit laatste foton en ongeacht de afstand tussen beide fotonen.

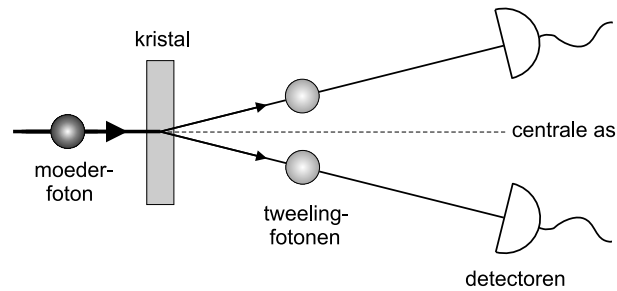
Het onderzoek dat gepresenteerd wordt in dit proefschrift gaat zoals eerder gezegd over lichtverstremgeling. Ook elders op de wereld wordt wetenschappelijk onderzoek verricht om dit natuurkundig verschijnsel beter te begrijpen. Zo is onder andere verstremgeling van fotonen aangetoond die tientallen kilometers van elkaar verwijderd zijn. Het ultieme doel van het onderzoek naar verstremgeling is het ontwikkelen van een *quantumcomputer* die vele malen sneller zou kunnen rekenen dan de huidige computers, en onder andere uitermate geschikt is voor het kraken van codes (cryptografie).



**Figuur 2:** (a) Twee zogenaamd quantummechanische tafeltennisballen bevinden zich ieder in een afgedekte doos en in de volgende superpositie-toestand: bal 1 is van 1-sterkwaliteit en bal 2 van 3-sterrenkwaliteit (bovenste balhelften), maar tegelijkertijd en even waarschijnlijk is bal 1 van 3-sterrenkwaliteit en bal 2 van 1-sterkwaliteit (onderste balhelften). De individuele kwaliteit van beide ballen is dus volledig onbepaald. (b) Door nu in doos 1 te kijken verdwijnt de superpositie en is bal 1 onmiddellijk van 1-ster- of van 3-sterrenkwaliteit. Zónder doos 2 te openen zal bal 2 dan respectievelijk van 3-sterren- of van 1-sterkwaliteit zijn, alsof het in directe verbinding (gestippelde pijl) staat met bal 1. Deze relatie wordt verstrengeling genoemd.

## Het maken van verstrengelde fotonen

Verstrengelde fotonen worden doorgaans in een speciaal kristal (een glazig plaatje) gemaakt, waar een ‘moederfoton’ wordt gesplitst in twee identieke ‘dochterfotonen’. De dochterfotonen vormen als het ware een tweelingpaar: het waarnemen van een van de twee fotonen geeft direct uitsluitsel over het karakter van het andere foton, ook al zijn beide fotonen gescheiden. Verstrengelde fotonen worden daarom ook wel *tweelingfotonen* genoemd. Het genoemde splitsingsproces, dat *spontaneous parametric down-conversion* wordt genoemd, is in figuur 3 weergegeven en wordt in hoofdstuk 2 beschreven. Aangezien er geen energie verloren mag gaan in dit proces is de energie van elk tweelingfoton precies de helft van die van het moederfoton. In de praktijk wordt vaak een blauwe bundel van moederfotonen gesplitst in twee rode bundels die elk een van de bijbehorende tweelingfotonen bevat. We kunnen in beide bundels een fotodetector plaatsen die ‘klikt’ zodra er een tweelingfoton op valt. Wanneer beide detectoren *tegelijk* klikken, weten we dat we een fotonpaar ‘gezien’ hebben en lichtverstrengeling kunnen meten. De geproduceerde tweelingfotonen zijn tegelijkertijd in drie opzichten met elkaar verstrengeld. We bespreken hieronder deze drie mogelijke vormen van lichtverstrengeling in polarisatie, tijd en ruimte.



**Figuur 3:** Twee verstrengelde fotonen worden als een tweelingpaar uit een moederfoton gemaakt. Beide fotonen bevinden zich even ver van het kristal en hun locaties zijn elkaars spiegelbeeld ten opzichte van de centrale as. Hoewel de tweelingfotonen gescheiden zijn, legt een waarneming van één foton onmiddellijk het karakter van het andere foton vast. Deze verstrengeling kan worden gemeten door in beide paden een detector te plaatsen.

De individuele polarisatie van de geproduceerde tweelingfotonen neemt alle mogelijke richtingen aan en is zodoende volledig onbepaald. Echter, meten we een willekeurige polarisatie voor een van de tweelingfotonen, dan staat onmiddellijk vast dat het andere tweelingfoton de polarisatie *loodrecht* op deze gemeten polarisatie bezit, zonder ook maar iets te doen met dit laatste foton. We spreken dan over *polarisatieverstrengeling* van fotonen. Aangezien de polarisatie van licht eenvoudig te manipuleren is (met onder andere polariserende elementen) geniet deze vorm van lichtverstrengeling de meeste populariteit in het wetenschappelijk onderzoek.

De twee verstrengelde fotonen worden *op hetzelfde moment* in het kristal aangemaakt en zullen op een willekeurig tijdstip na hun geboorte *dezelfde* afstand vanaf het kristal hebben afgelegd (zie figuur 3). Door in een van de twee bundels een foton te detecteren op een zekere afstand van het kristal, weten we zeker dat zijn partner in de andere bundel zich op dezelfde afstand van het kristal bevindt. Aangezien deze afstand gekoppeld is aan de verstreken tijd na de geboorte van het fotonpaar, noemen we deze vorm van verstrengeling ook wel *tijdsverstrengeling* van fotonen.

Tweelingfotonen worden niet alleen op hetzelfde moment maar ook *op dezelfde dwarspositie* in het kristal aangemaakt. Hiermee bedoelen we de positie in de richting loodrecht op de invallende bundel van moederfotonen, ofwel loodrecht op de centrale as (zie figuur 3). Het meten van een zekere dwarspositie van een foton in één van de uittredende bundels legt onmiddellijk de dwarspositie van zijn partner in de andere bundel vast. Deze laatste positie is namelijk het spiegelbeeld van de gemeten positie ten opzichte van de centrale as. We spreken hier over de verstrengeling van fotonen in hun dwarspositie, ofwel *ruimtelijke verstrengeling* van licht.

## Dit proefschrift

Het onderzoek in dit proefschrift omvat zowel de polarisatie- als de ruimtelijke verstrengeling van licht. In hoofdstuk 3 wordt een nieuwe methode gepresenteerd om de dikte en de snijhoek

van het genererende kristal heel nauwkeurig te bepalen. De invloed van de kristaldikte op het aantal geproduceerde polarisatieverstrengelde fotonen wordt in hoofdstuk 4 behandeld. We hebben aangetoond dat onder bepaalde omstandigheden deze productie omgekeerd evenredig is met de kristaldikte: een 0.25 millimeter dik kristal levert gek genoeg vier keer zoveel fotonparen op als een 1 millimeter dik kristal.

In hoofdstuk 5 worden twee experimenten beschreven waarin de gemeten sterktes van polarisatieverstrengeling met elkaar worden vergeleken. In het eerste experiment wordt in een van de bundels een metalen gatenrooster (met gaten kleiner dan de golflengte) geplaatst. In het tweede experiment worden de fotonen vóór het gatenrooster afzonderlijk 'uit elkaar getrokken' door hun polarisatie te ontbinden, en worden ze ná het gatenrooster op omgekeerde wijze weer 'hersteld'. Hoewel deze laatste situatie identiek lijkt aan die van het eerste experiment, meten we verrassend genoeg een aantoonbaar zwakkere polarisatieverstrengeling. Dit kan worden verklaard door de voortplanting van bepaalde golven over het oppervlak van het metalen gatenrooster.

In hoofdstuk 6 wordt het effect van het ruimtelijke karakter van de moederbundel op de ruimtelijke karakter van de twee dochterbundels bestudeerd. Verder wordt onderzocht welke gevolgen dit heeft voor de sterkte van de polarisatieverstrengeling. In hoofdstuk 7 wordt aangetoond dat de gemeten sterkte van de polarisatieverstrengeling sterk afhangt van de wijze waarop de tweelingfotonen gedetecteerd worden.

In het experiment dat in hoofdstuk 8 beschreven is, hebben beide tweelingfotonen de mogelijkheid om twee verschillende paden te volgen. We onderzoeken of we op grond van de gemeten dwarspositie van één foton kunnen beslissen welk pad het andere foton heeft gevolgd. Het antwoord op deze vraag blijkt af te hangen van de symmetrie van de meetopstelling. Hoofdstuk 9 behandelt een soortgelijk experiment waarin één van de bundels om zijn eigen as wordt gedraaid. Ook hier bepaalt de symmetrie van de meetopstelling of de sterkte van de ruimtelijke verstrengeling afneemt met de hoeveelheid verdraaiing. Tevens hebben we met dit experiment de grootte van de ruimtelijke structuur van het verstrengelde licht kunnen vaststellen.

Samenvatting

---

## List of publications

---

- *Erosion patterns in a sediment layer*,  
Adrian Daerr, Peter Lee, José Lanuza, and E. Clément,  
Phys. Rev. E. **67**, 065201(R) (2003).
- *Increased polarization-entangled photon flux via thinner crystals*,  
P.S.K. Lee, M.P. van Exter, and J.P. Woerdman,  
Phys. Rev. A **70**, 043818 (2004).
- *Simple method for accurate characterization of birefringent crystals*,  
P.S.K. Lee, J.B. Pors, M.P. van Exter, and J.P. Woerdman,  
Appl. Opt. **44**, 866-870 (2005).
- *How focused pumping affects type-II spontaneous parametric down-conversion*,  
P.S.K. Lee, M.P. van Exter, and J.P. Woerdman,  
Phys. Rev. A **72**, 033803 (2005).
- *Time-resolved polarization decoherence in metal hole arrays with correlated photons*,  
Peter S.K. Lee, Martin P. van Exter, and J.P. Woerdman,  
J. Opt. Soc. Am. B **23**, 134-138 (2006)
- *Spatial labeling in a two-photon interferometer*,  
P.S.K. Lee and M.P. van Exter,  
Phys. Rev. A **73**, 063827 (2006).
- *Mode counting in high-dimensional orbital angular momentum entanglement*,  
M.P. van Exter, P.S.K. Lee, S. Doesburg, and J.P. Woerdman,  
submitted to Phys. Rev. Lett.

List of publications

---

## Curriculum vitæ

---

Peter Sing Kin Lee werd op 12 december 1978 geboren in Wageningen. In 1997 behaalde hij zijn atheneumdiploma aan het Ichthus College te Veenendaal. In datzelfde jaar begon hij aan de studie sterrenkunde aan de Universiteit Leiden, waarvoor hij de propedeuse behaalde. In 1999 besloot hij de overstap te maken naar de studie natuurkunde, eveneens aan de Universiteit Leiden. Zijn afstudeerstage, onder begeleiding van dr. M. L. van Hecke, betrof het experimentele onderzoek naar vertragingseffecten in een tweedimensionaal granulaair systeem. Daarnaast heeft hij onder begeleiding van prof. E. Clément en dr. A. Daerr een onderzoeksstage gelopen aan de Université Pierre et Marie Curie te Parijs, Frankrijk. Het onderwerp was ditmaal erosievorming in een sedimentlaag. In 2002 slaagde hij voor zijn doctoraal examen natuurkunde.

In september 2002 trad hij in dienst van de Stichting voor Fundamenteel Onderzoek der Materie (FOM) om een promotieonderzoek te verrichten in de vakgroep 'Quantum Optics and Quantum Information', onder leiding van dr. M. P. van Exter en prof. dr. J. P. Woerdman. Het onderwerp betrof de quantumverstremeling van polarisatie- en ruimtelijke vrijheidsgraden van fotonen. In dit proefschrift zijn de behaalde onderzoeksresultaten opgenomen.

Naast het onderzoekswerk heeft hij deelgenomen aan de conferenties *Quantum Optics: EuroConference on Cavity QED and Quantum Fluctuations* in Granada, Spanje (2003) en *CLEO / QELS* in Baltimore, Verenigde Staten (2005). Op deze laatste conferentie en op de najaarsvergadering van de Nederlandse Natuurkundige Vereniging (sectie Atoom-, Molecuul- en Optische Fysica) in Lunteren (2005) heeft hij een wetenschappelijke voordracht gegeven. Als onderwijstaak verzorgde hij het werkcollege van het derdejaarsvak 'Signaalverwerking en Ruis'. Verder heeft hij met plezier het jaarlijkse kerstontbijt van zijn vakgroep tezamen met de vakgroep 'MoNOS' georganiseerd.

Curriculum vitæ

---

## Nawoord

---

Gedurende mijn promotieonderzoek, dat geresulteerd heeft in dit proefschrift, heb ik op de steun van meerdere mensen mogen rekenen. Ik wil hen bij dezen graag bedanken.

Een goed lopend experimenteel onderzoek is onlosmakelijk verbonden met de ondersteuning van een fijnmechanische afdeling. In dit opzicht wil ik met name Koos Benning en Ewie de Kuiper bedanken voor hun waardevolle kennis en kunde, die ze hebben weten te vertalen naar allerlei op maat vervaardigde onderdelen van mijn meetopstelling. Modern onderzoek kan ook niet bestaan zonder elektronische apparatuur en snelle computers. De expertise op dit gebied werd gegarandeerd door Arno van Amersfoort, René Overgaww en Leendert Prevo, die de, soms onvermijdelijke, ‘probleempjes’ met hardware en software telkens voor mij hebben kunnen oplossen. De secretariële ondersteuning was in de behulpzame handen van Anneke Aschoff, Henriette van Leeuwen en Daniëlle van Raaij. De warme aanwezigheid van Anneke hebben we, tot onze droefenis, al in het derde jaar van mijn promotie moeten missen.

De afgelopen jaren heb ik prettig mogen samenwerken met de studenten Bart-Jan Pors, Rakesh Partapsing, Yung-Chin Oei en Sander Doesburg. Tijdens hun stages in de vakgroep hebben zij niet alleen een concrete bijgedrage geleverd aan de voortgang van mijn onderzoek, maar heeft hun, soms kritische, nieuwsgierigheid mij zeker ook scherp gehouden.

Ik ben dankbaar voor de aangename sfeer waarin ik mijn promotieonderzoek heb mogen verrichten. De ontspanning binnen en buiten het lab, weerspiegeld in onder andere de koffiepauzes, filmavonden en groepsetentjes, was uiteraard niet mogelijk geweest zonder de aanwezigheid van mijn collega’s, te weten de stafleden, de promovendi Yngve Lien, Jos Dingjan, Sumant Oemrawsingh, Hayk Haroutyunyan, Javier Loaiza, Jorrit Visser, Erwin Altewischer, Thijs Klaassen, Nikolay Kuzmin, Graciana Puentes, Eduard Driessen, Steven Habraken, Bart-Jan Pors en Wouter Peeters, de postdocs Andrea Aiello, Cyriaque Genet en Dirk Voigt, en alle studenten.

Tot slot wil ik mijn broer, mijn zus en mijn ouders bedanken, die mij te allen tijde hebben gestimuleerd en onvoorwaardelijk hebben gesteund.

